

MoS₂-based anode for sodium ion batteries

Xiyan Yue

Graduate School of Science and Technology

Hirosaki University

2021

ABSTRACT

Sodium ion batteries (SIBs), as a promising candidate for lithium ion batteries (LIBs), have attracted researchers' great attention because of the abundant resources and low cost. Looking for suitable anode materials is very essential for developing SIBs. Layered metal sulfides (MS_2) are considered as one of potential anode materials for SIBs due to their structural stability and high theoretical capacity. However, low conductivity, large volume expansion, and slow electrochemical kinetics cause in poor cycling stability and bad rate performance, which severely limit its application as an anode material for SIBs. Recently, numerous efficient strategies such as nanostructure designing, electrolyte selecting, voltage range cutting off and combination of MS_2 with carbon materials have been applied to enhance the electrochemical performance of such anode materials for SIBs. The purposes are to effectively provide more active sites for Na^+ storage, shorten Na^+ diffusion path, enhance the conductivity, and buffer the volume expansion. Unfortunately, most of strategies are too complex to limit their applications in the preparation of anode materials. Therefore, it is still full of challenges to find a facile method to prepare anode materials with excellent electrochemical performance for SIBs. In this dissertation, simpler strategies for enhancing the electrochemical performances of MoS_2 -based anode have been developed.

Firstly, to improve the conductivity and cycling stability, coral reef-like MoS_2 microspheres (MoS_2 -MS) with 1T/2H phase are synthesized by a simple one-step hydrothermal method. It is found that this material has a disordered structure, rich defects

and large interlayer spacing. As it is used as the anode material for sodium ion batteries (SIBs), a stable specific capacity of 467 mAh g⁻¹ at a current density of 100 mA g⁻¹ after 100 cycles is delivered. Moreover, after 500-cycle test at 1 A g⁻¹, a highly stable specific capacity is still maintained at 412 mAh g⁻¹. In addition, even at a high current density of 20 A g⁻¹, the MoS₂-MS electrode delivers a specific capacity of 100 mAh g⁻¹. It is considered that the 1T/2H phase MoS₂-MS with the disordered structure can effectively enhance the electrical conductivity for the rate performance improvement, and furthermore, the rich defects provide more active sites for Na⁺ storage and the large interlayer spacing allows the rapid diffusion of the Na⁺ ions.

Secondly, in order to further improve the electronic conductivity and sluggish electrochemical kinetics and specific capacity of MoS₂-based anode, vanadium is combined into the framework of MoS₂ to form VMoS₂ (VMS₂) through a facile one-step hydrothermal method. Combined the experiment results with the density functional theory calculations, it is found that V mediating not only significantly increases the electronic conductivity due to metallic property but also decreases the energy barrier (0.069 eV) of sodium ion transportation when compared with that of the pure MoS₂ (0.12 eV), resulting in excellent electrochemical performance with rapid electrochemical kinetics. Furthermore, the disordered structure with rich defects in the VMS₂ could provide more active sites for Na⁺ storage. As a result, when it is used as the anode material of SIBs, a high specific capacity (548.1 mAh g⁻¹ at a current density

of 100 mA g⁻¹) with excellent cycling stability (451.6 mAh g⁻¹ retaining after 800 cycles at 2 A g⁻¹) and superb rate performance (207.4 mAh g⁻¹ retained at 20 A g⁻¹) is achieved.

Finally, even though vanadium mediating can effectively promote the sluggish electrochemical kinetics and electronic conductivity, the specific capacity is still low, which cannot meet the demand of society. In order to achieve higher specific capacity, a novel orderly layered VMoS₂ (OL-VMS) anode material is synthesized through a facile hydrothermal self-assembly method followed by a heating treatment process. As it is used as the anode material for the SIBs, the unique structure of OL-VMS not only facilitates the rapid migration of sodium ions between the stacked layers but also provides stable framework for the volume expansion during charging/discharging process. In addition, vanadium mediating in the framework causes more defects to produce more active sites for the sodium ion storage. As such, the OL-VMS based anode exhibits high reversible capacities of 602.9 mAh g⁻¹ at 0.2 mA g⁻¹ and 534 mAh g⁻¹ even after 190 cycles at 2 A g⁻¹. Furthermore, the OL-VMS based anode delivers a high reversible capacity of 626.4 mAh g⁻¹ after 100 cycles at 2 A g⁻¹ in a voltage range of 0.01-3 V. Particularly, even in the absence of conductive carbon, it still showed an excellent specific capacity of 260 mAh g⁻¹@1 A g⁻¹ after 130-cycle in a 0.3-3 V voltage range, which should be benefit for the cost reduction and energy density increase.

ACKNOWLEDGMENTS

I would like to express my sincere gratitude to all people who has supported and encouraged me both in scientific research and life during the period of my Ph.D course in Japan.

My deepest gratitude goes first and foremost to my supervisor Professor Dr. Abuliti Abudula and Professor Guoqing Guan, who have offered me an opportunity and place to continue learning. Furthermore, when I met problems, they always gave me valuable comments and suggestions in time to conquer the issues.

In addition, I would like to thank Associate Professor Dr. Akihiro Yoshida in our group for his useful comments during the period of my Ph.D course in Japan.

I would like to express my heartfelt thanks to Profs. Xiaogang Hao and Zhongde Wang, Department of Chemical Engineering, Taiyuan University of Technology, China, for their helps regarding to sample characterizations.

I also would like to thank Prof. Zhongqing Jiang, Department of Physics, Key Laboratory of ATMMT Ministry of Education, Zhejiang Sci-Tech University, China, for his thoughtful comments.

I am also greatly indebted to all co-authors for their cooperation, all members in our group, and all staff in Institute of Regional Innovation (IRI) and Graduate School of Science and Technology, Hirosaki University, for their supports.

I would like to thank my wife for her accompanying and collaborative effort, my mother for her encouragements, and my brother for his supports.

Finally, last my thanks would go to China Scholarship Council and ZiQoo Chemical Co. Ltd. for their supports during the period of my Ph.D course in Japan.

Thank you all very much.

Xiyan Yue

TABLE OF CONTENTS

ABSTRACT.....	i
ACKNOWLEDGMENTS	iv
LIST OF TABLES	ix
LIST OF FIGURES	x
CHAPTER 1 Introduction.....	1
1.1 General Introduction	1
1.2 Strategies.....	4
1.2.1 Morphology design	4
1.2.2 Structural engineering.....	8
1.2.3 Doping or combination with non-carbon materials	12
1.2.4 Combination with carbon materials	15
1.3 Objectives of this study.....	22
1.4 Scope of this dissertation	22
References.....	24
CHAPTER 2 Experimental.....	34
2.1 Reagent information.....	34
2.2 Characterization	35
2.2.1 Scanning electron microscope (SEM)	35
2.2.2 Energy dispersive spectrometer (EDS).....	35
2.2.3 Transmission electron microscope (TEM).....	35
2.2.4 X-ray diffractometer (XRD)	35
2.2.5 X-ray photoelectron spectrometer (XPS).....	35
2.2.6 Raman	36
2.3 Electrochemical measurement	36
CHAPTER 3 Coral reef-like microspheres with 1T/2T phase as high performance anode material for sodium ion batteries.....	37
3.1 Introduction.....	37

3.2 Experimental	39
3.2.1 Synthesis of MoS ₂ -MS and MoS ₂ -MS-800.....	39
3.3 Results and discussion	41
3.3.1 Characterization of MoS ₂ -MS and MoS ₂ -MS-800	41
3.3.2 Electrochemical performance	47
3.3.3 Electrochemical kinetics	53
3.3.4 EIS analysis.....	56
3.4 Conclusions.....	57
References.....	58
CHAPTER 4 A novel vanadium-mediated MoS ₂ with metallic behavior for sodium ion batteries: achieving fast Na ⁺ diffusion to enhance electrochemical kinetics	65
4.1 Introduction.....	65
4.2 Experimental	67
4.2.1 Synthesis of VM-23, VM-33, VM-43, VM-53, MoS ₂ , A-MoS ₂ , and VS ₂	67
4.2.2 Characterizations.....	67
4.2.3 Electrochemical measurements.....	68
4.2.4 Density functional theory (DFT) calculations	69
4.3 Results and discussion	70
4.3.1 Characterizations.....	70
4.3.2 Na ⁺ storage mechanism.....	82
4.3.3 Electrochemical performance	85
4.3.4 Electrochemical kinetics and EIS analysis	90
4.3.5 DFT calculations	96
4.4 Conclusions.....	99
References.....	100
CHAPTER 5 Controllable synthesis of novel orderly layered VMoS ₂ anode materials with super electrochemical performance for sodium ion batteries	111

5.1 Introduction.....	111
5.2 Experimental.....	113
5.2.1 Synthesis of OL-VMS	113
5.2.2 Characterizations.....	113
5.2.3 Electrochemical measurements.....	114
5.3 Results and discussion	115
5.3.1 Characterizations.....	115
5.3.2 Electrochemical performance	124
5.3.3 Electrochemical kinetics	131
5.3.4 EIS analysis.....	133
5.4 Conclusions.....	137
References.....	138
CHAPTER 6 Conclusions and Prospects	148
6.1 Conclusions.....	148
6.2 Prospects	151
List of publications and presentations.....	153

LIST OF TABLES

Table 1.1 Comparison of the physicochemical properties of lithium and sodium	2
Table 2.1 Reagent information for experiment	34
Table 4.1 Atomic contents in the VM-33, VM-43, and VM-53 based on elemental analysis.....	74
Table 4.2 Fitting results of Nyquist plots based on the equivalent circuit in Fig. S8 after the 20 th cycle.	95
Table 5.1 Comparison of electrochemical performance of the present OL-VMS based anode with the reported MoS ₂ and VS ₂ based ones.	130
Table 5.2 Fitting results of Nyquist plots based on the equivalent circuits after 1 st , 5 th , 10 th , and 20 th cycles.....	134

LIST OF FIGURES

Figure 1.1 Energy density comparison of SIBs with different commercial LIBs	2
Figure 3.1 (a), (b) and (c) SEM morphologies of the MoS ₂ -MS. (d) elemental mapping images of MoS ₂ -MS. (g) TEM image of MoS ₂ -MS; (e), (f), (h) and (i) HRTEM images of the MoS ₂ -MS.	42
Figure 3.2 (a), (b) and (c) SEM morphologies of the MoS ₂ -MS-800. (d) TEM image of MoS ₂ -MS-800; (e), (f), and (g) HRTEM images of the MoS ₂ -MS-800.	43
Figure 3.3 (a) XRD patterns of MoS ₂ -MS and MoS ₂ -MS-800. (b) Raman spectra of MoS ₂ -MS and MoS ₂ -MS-800. High-resolution XPS spectra of the (c) Mo 3d peak and (d) S 2p peak in MoS ₂ -MS.	45
Figure 3.4 (a) XPS survey spectra of MoS ₂ -MS and MoS ₂ -MS-800. Comparison of high-resolution XPS spectra of Mo 3d (b) and S 2p (c).	46
Figure 3.5 (a) Typical galvanostatic charging/discharging profiles for the the 1 st , 2 nd , 5 th and 10 th cycles at a current density of 100 mA g ⁻¹ for MoS ₂ -MS and MoS ₂ -MS-800 based anodes; (b) Typical CV curves of MoS ₂ -MS based anode for the first 3 cycles at a scanning rate of 0.1 mV s ⁻¹ in the voltage range of 0.3–3 V; and cycling performances of MoS ₂ -MS and MoS ₂ -MS-800-based anodes at current rates of (c) 100 mA g ⁻¹ and (d) 1 A g ⁻¹	47

Figure 3.6 Typical CV curves of MoS ₂ -MS-800-based anode for the first three cycles at a scanning rate of 0.1 mV s ⁻¹ in the voltage range of 0.3–3 V.	48
Figure 3.7 TEM images of (a) MoS ₂ -MS and (d) MoS ₂ -MS-800 before cycling; TEM and HRTEM images of (b, c) MoS ₂ -MS and (e, f) MoS ₂ -MS-800 after 500 cycles at the current density of 1 A g ⁻¹	50
Figure 3.8 (a) Cycling performances of the MoS ₂ -MS and MoS ₂ -MS-800-based anodes at a current rate of 2 A g ⁻¹ ; (b) Rate performances of MoS ₂ -MS and MoS ₂ -MS-800-based anodes. HRTEM images of (c) MoS ₂ -MS after 500 cycles at the current density of 1 A g ⁻¹	51
Figure 3.9 (a) CV curves of MoS ₂ -MS at different scan rates from 0.7 to 1.5 mV s ⁻¹ , (b) corresponding log <i>i</i> vs. log <i>v</i> plots of peaks 1, 2 and 3; (c) capacitive contribution of MoS ₂ -MS in comparison to the total current at 1.5 mV s ⁻¹ ; (d) capacitive contribution of MoS ₂ -MS at different scan rate from 0.7 to 1.5 mV s ⁻¹	53
Figure 3.10 (a) CV curves of MoS ₂ -MS-800 at different scan rates from 0.7 to 1.5 mV s ⁻¹ , (b) capacitive contribution of MoS ₂ -MS-800 in comparison to the total current at 1.5 mV s ⁻¹ ; (C) capacitive contribution of MoS ₂ -MS-800 at different scan rate from 0.7 to 1.5 mV s ⁻¹	54
Figure 3.11 Nyquist plots of the (a) MoS ₂ -MS-based and (b) MoS ₂ -MS-800-based anodes.	56

Figure 4.1 (a) Schematic illustration of the VMS ₂ synthesis; FESEM images of the (b, e) VM-33, (c, f) VM-43, and (d, g) VM-53.....	70
Figure 4.2 SEM morphologies of (a), (b) pure MoS ₂ ; (c), (d) A-MoS ₂ ; (e), (f) VS ₂ ; and (g) VM-23.	71
Figure 4.3 Elemental analysis of (a) VM-33, (b) VM-43, and (c) VM-53.	73
Figure 4.4 (a and b) TEM and (c-f) HRTEM images of VM-43 sample. (g) STEM elemental mappings of (h) S, (i) Mo and (j) V.....	75
Figure 4.5 TEM images of (a) VM-33 and (d) VM-53; HRTEM images of (b), (c) VM-33 and (e), (f) VM-53.....	76
Figure 4.6 (a) XRD patterns of VM-33, VM-43 and VM-53. High-resolution XPS spectra of (b) Mo 3d, (c) V 2p and (d) S 2p.....	78
Figure 4.7 XRD patterns of (a) MoS ₂ , A-MoS ₂ , (b) VS ₂ ., and (c) VM-43 after calcination at 800 °C for 2h in Argon gas.	79
Figure 4.8 XPS survey spectra of VM-33, VM-43 and VM-53.....	80
Figure 4.9 Raman spectra of VM-33, VM-43 and VM-53.	81
Figure 4.10 (a) Typical CV curves of VM-43 based anode in the first three cycles at a scanning rate of 0.1 mV s ⁻¹ in a voltage range of 0.3-3 V; (b) <i>Ex-situ</i> XRD patterns of VM-43 at different voltages during the discharging/charging process.	82
Figure 4.11 XRD pattern of glass fiber separator after the 200 th cycle.	82

Figure 4.12 Typical CV curves of (a) VM-33 and (b) VM-53 for the first three cycles at a scanning rate of 0.1 mV s^{-1} in the voltage range of 0.3-3 V.....84

Figure 4.13 (a) Typical galvanostatic charging/discharging profiles in the 1st, 2nd, 10th, 20th, and 50th cycles for the VM-43 based anode at a current density of 100 mA g^{-1} ; Cycling performance of the VM-43 based anode at current densities of (b) 100 mA g^{-1} and (d) 2 A g^{-1} ; (c) Cycling performances of the VM-33, VM-43, and VM-53 based anodes at a current density of 1 A g^{-1} ; (e) Rate performances of A-MoS₂, VM-33, VM-43 and VM-53 based anodes; (f) Comparison of rate performance of the VM-43 based anode with other MoS₂-based anodes.....85

Figure 4.14 Typical galvanostatic charging/discharging profiles at the 1st, 2nd, 10th, 20th and 50th cycles of (a) A-MoS₂, (b) VM-33 and (c) VM-53 at a current density of 100 mA g^{-1} ; Cycling performance of (d) A-MoS₂, (e) VM-43 and (f) VM-53 at a current density of 100 mA g^{-1} 86

Figure 4.15 (a) Typical galvanostatic charging/discharging profiles at the 1st, 2nd, 5th, and 10th cycles of VS₂; (b) Cycling performance of VS₂ at a current density of 1 A g^{-1}87

Figure 4.16 (a) TEM and (b) HRTEM images of VM-43 after the 800th cycle at the current density of 2 A g^{-1}89

Figure 4.17 (a) CV curves of VM-43 based anode at different scan rates from 0.1 to 0.7 mV s^{-1} , (b) corresponding $\log i$ vs. $\log v$ plots of peaks 1, 2, 3 and 4; (c) capacitive contribution of the VM-43 material in comparison to the total current

at 0.7 mV s^{-1} ; (d) capacitive contribution of $\text{MoS}_2\text{-MS}$ at different scan rates from 0.1 to 0.7 mV s^{-1} , (e) Nyquist plots of the A- MoS_2 , VM-33, VM-43, and VM-53 based anodes.90

Figure 4.18 (a) CV curves of A- MoS_2 at different scan rates from 0.1 to 0.7 mV s^{-1} , (b) capacitive contribution of A- MoS_2 related to the total current at 0.7 mV s^{-1} ; (c) capacitive contribution of A- MoS_2 at different scan rates from 0.1 to 0.7 mV s^{-1}92

Figure 4.19 (a) CV curves of VM-33 based anode at different scan rates from 0.1 to 0.7 mV s^{-1} , (b) corresponding $\log i$ vs. $\log v$ plots of the peaks 1, 2, 3, and 4; (c) capacitive contribution of VM-43 related to the total current at 0.7 mV s^{-1} ; (d) capacitive contribution of $\text{MoS}_2\text{-MS}$ at different scan rates from 0.1 to 0.7 mV s^{-1}93

Figure 4.20 (a) CV curves of VM-53 based anode at different scan rates from 0.1 to 0.7 mV s^{-1} , (b) corresponding $\log i$ vs. $\log v$ plots of peak 1, 2, 3, and 4; (c) capacitive contribution of VM-43 related to the total current at 0.7 mV s^{-1} ; (d) capacitive contribution of $\text{MoS}_2\text{-MS}$ at different scan rates from 0.1 to 0.7 mV s^{-1}94

Figure 4.21 The equivalent circuit used for the analysis of the impedance plots.94

Figure 4.22 Optimized structures of the (a) pure MoS ₂ and (b) VMS ₂ ; (c) density of states of the pure MoS ₂ and VMS ₂ ; Na ⁺ migration path in the interlayer of the (d) pure MoS ₂ and (e) VMS ₂ ; (f) energy profiles along the diffusion path.	97
Figure 4.23 (a) Na ⁺ migration path in the interlayer of VMS ₂ from Mo to V; (b) energy profiles along the diffusion path.	97
Figure 4.24 Illustration of Na ⁺ diffusion and electronic transmission during the charging/discharging processes in the VMS ₂ based anode.	98
Figure 5.1 SEM images of OL-VMS synthesized with different amount of ammonia solution: (a and b) 0 ml, (c and d) 0.5 ml, (e and f) 0.1 ml, and (g and h) 2 ml.	116
Figure 5.2 (a and b) SEM images of OL-VMS, (c) EDS elemental mappings of S, Mo, and V, (d) TEM and (e and f) HRTEM images of OL-VMS.	117
Figure 5.3 SEM images of OL-VMS samples prepared with different hydrothermal synthesis time: (a and b) 3 h, (c and d) 6 h, (e and f) 12 h, and (g and h) 18 h.	119
Figure 5.4 Schematic illustration of the OL-VMS fabrication procedure.	120
Figure 5.5 (a) XRD pattern and (b) Raman spectrum of OL-VMS sample.	121
Figure 5.6 XRD patterns of OL-VMS samples prepared at different conditions.	122
Figure 5.7 (a) XPS survey spectrum of OL-VMS; High-resolution (b) Mo 3d, (c) V 2p and (d) S 2p spectra of OL-VMS.	124

Figure 5.8 (a) Typical CV curves of the OL-VMS based anode in the first three cycles under condition of 0.1 mV s^{-1} within a voltage range from 0.1 to 3 V; (b) Typical galvanostatic charging/discharging curves in the 1st, 2nd, and 5th cycles for the OL-VMS based anode at 0.2 A g^{-1} ; (c) Stability measurement of the OL-VMS based anode at 2 A g^{-1} ; (d) Rate capability of the OL-VMS based anode; (e) Long cyclability of the OL-VMS based electrode at 5 A g^{-1} 126

Figure 5.9 (a) Cycling performances of the OL-VMS based anode at a current density of 2 A g^{-1} in different voltage ranges of 0.3-3, 0.2-3, and 0.01-3V; (b) Cycling performance of the anode with the flower-like sample (prepared without ammonia solution) at a current density of 2 A g^{-1} in the voltage range of 0.01-3V; 127

Figure 5.10 Cycling performance of the OL-VMS based anode with (a) in the case without conductive carbon addition and (b) high loading amount at a current density of 1 A g^{-1} in the voltage range of 0.3-3 V. 128

Figure 5.11 (a) CV curves of the OL-VMS based anode at different scan rates from 0.1 to 1.5 mV s^{-1} ; (b) Fitting line of $\log i$ vs. $\log v$ plots for peaks 1, 2, 3 and 4; (c) The calculated contribution of capacitive at 1.5 mV s^{-1} ; (d) The content of capacitive contribution for OL-VMS at various scan rates from 0.1 to 1.5 mV s^{-1} 132

Figure 5.12 (a) EIS Nyquist plots of the OL-VMS-based electrode after 1st, 5th, 10th, and 20th cycles (inset: equivalent circuit); (b) the linear fitting between Z' and $\omega^{-1/2}$ 134

Figure 5.13 SEM images of (a, b) OL-VMS and (c, d) VMS with flower-like structure after 1 and 10 cycles. 136

Figure 5.14 Illustration of pulverization of different structure during intercalation/deintercalation of Na^+ 136

CHAPTER 1 Introduction

1.1 General Introduction

With the continuous improvement of human awareness of environmental protection and energy crisis, green energy with environmentally friendly, sustainable and renewable has gradually entered people's vision [1-4]. Lithium ion batteries (LIBs), as a commercialized green energy storage devices, have been widely used in various fields, such as portable electronic devices, electronic vehicles and energy storage filed due to advantages of good cycling stability, high specific capacity and renewability [5, 6]. However, the limited lithium resource and high price of lithium cannot meet the increasing demand of society for batteries as shown in Table 1.1 [7]. In this case, the most urgent thing is to find an alternative to LIBs to meet demand of market. Recently, sodium ion batteries (SIBs) are considered as a promising candidate of LIBs owing to the similar electrochemical performance, abundant sodium resource, and low price (Table 1.1) [7-10]. Furthermore, as shown in Figure 1.1, the energy density of sodium ion batteries is higher than that of commercial LiFePO_4 based LIBs, which can be a potential candidate of LIBs in large-scale energy storage field [11-12]. Unfortunately, the anodes for LIBs are not suitable for SIBs due to larger ionic radius of Na^+ compared with that of Li^+ (1.02 Å vs 0.76 Å, Table 1.1), which result in sluggish kinetics and large volume expansion. Thus, it is significant and meritorious to develop anode with high electrochemical performance for SIBs [13-15].

Table 1.1 Comparison of the physicochemical properties of lithium and sodium [7].

Property ^{a)}	Lithium	Sodium
Abundance (ppm)	20	23 600
Atomic mass (g mol ⁻¹)	6.94	22.99
Ionic radius (nm)	0.076	0.102
Distribution	70% in South America	Universally
Price, carbonate (\$ per ton)	≈5800	≈250–300

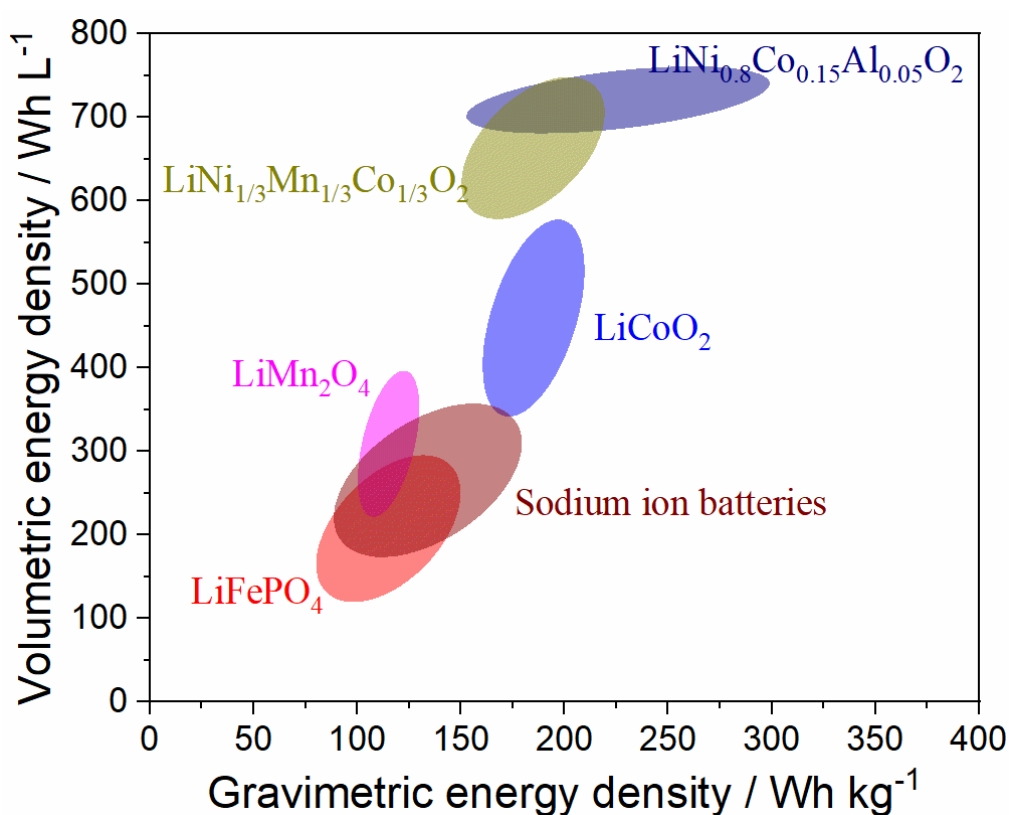


Figure 1.1 Energy density comparison of SIBs with different commercial LIBs [11-12].

Recently, numerous researchers focus on carbon material, metal oxide, metal sulfide, and alloy based anodes, which are considered as promising ones for SIBs [16-23]. Among these anode materials, metal sulfide has attracted widespread attention due to higher specific capacity and initial coulombic efficiency compared with carbon based one, higher conductivity and faster conversion reaction compared with metal oxide

based one, and smaller volume expansion and longer cycling stability compared with alloy based one [24-26]. Especially, layered metal sulfide (MS_2 , $M=Mo, V, W, Sn$), as a special kind of metal sulfide, has been widely studied as anode materials for SIBs owing to large interlayer spacing, high theoretical capacity, and weak van der Waals forces between interlayers [27-29]. For instance, MoS_2 possesses a large interlayer spacing of 0.615 nm, which can provide more active sites for Na^+ storage and facilitate diffusion of Na^+ between interlayers. Even though layered metal sulfide exhibits several merits mentioned above, the problems of low conductivity, sluggish electrochemical kinetics and large volume expansion are still existed during charging/discharging process, which cause short cycling life and low rate performance [4, 31].

To conquer the above problems, researchers have adopted numerous effective strategies to improve the electrochemical performance of MS_2 -based anode. For examples, Zhang *et al.* [32] synthesized MoS_2 nanobelts with 002 plane edges-enriched flat surfaces as the anode material for SIBs, which possess more active sites for Na^+ storage, short distance for Na^+ diffusion, and stable framework for volume change during cycling. When it is used as anode for SIBs, it delivered specific capacities of 520 mA h g^{-1} at a current density of 1 A g^{-1} and 380 mA h g^{-1} at a current density of 20 A g^{-1} after 100 cycles, respectively. Wang *et al.* [33] use the one-step solvothermal method without additives to fabricate metallic WS_2 hollow microspheres as anode material for SIBs. The hollow structure with expanded interlayer spacing and metallic characteristic can improve Na^+ diffusion and electronic conductivity, resulting in excellent cycling stability with 285 mA h g^{-1} at 2 A g^{-1} after 2000 cycle as well as superb

rate performance with 307.7 mA h g⁻¹ at 1 A g⁻¹. Furthermore, Li *et al.* [34] fabricated SnS₂@C@rGO as anode material for SIBs, which shows a high reversible capacity of 721.9 mA h g⁻¹ at a current density of 0.05 A g⁻¹ and superior rate performance with 397.4 mA h g⁻¹ at a current density of 2 A g⁻¹. Such excellent electrochemical performance is attributed to carbon matrix and rGO shell, which can effectively not only increase the conductivity but also buff the volume expansion during charging/discharging process.

Herein, the main effective strategies achieving high electrochemical performance for anode of SIBs, including the morphology design, structural engineering, doping or combination with non-carbon materials, and carbon material modification, are summarized. The above strategies can effectively enhance the electrochemical performance, which are discussed in the following sections.

1.2 Strategies

1.2.1 Morphology design

In general, morphology design is one of effective way to solve the problems MS₂ face and improve the electrochemical performance of MS₂-based electrodes. The specific morphology can produce more active sites for sodium ion storage, provide short or smooth pathway for sodium ion diffusion, and sufficient distance to buff the volume expansion during charging/discharging process, which can effectively enhance the specific capacity, rate performance, and cycling stability.

Previous work published by P. Wang *et al.* [35] reported that a novel hierarchical tubular MoS₂ was used as anode for SIBs, which was synthesized through a simple hydrothermal method in the presence of tetramethylammonium bromide. As a result, a high reversible capacity of 652.5 mAh g⁻¹ was achieved for tubular MoS₂-based electrode at current density of 100 mA g⁻¹ after 50 cycles. Furthermore, tubular MoS₂-based electrode also exhibits a good cycling stability with a capacity retention rate of 94.2% after 100 cycles at current density of 1 A g⁻¹. Such excellent electrochemical performance is ascribed to specific hierarchical structures formed by loosely stacked nanosheets, which can provide smooth pathway to promote Na⁺ diffusion, more active sites for Na⁺ storage, and stable framework to buff the volume expansion during intercalation/deintercalation process of Na⁺. In addition, K. Yao *et al.* [36] synthesized grain-like MoS₂ particulates through sulfurization process with high concentration of sulfur vapor, which consist of MoS₂ nanoparticle and few layer MoS₂ nanosheets coating on the surface. When it was used as anode for SIBs, it displayed a high specific capacity of 324 mAh g⁻¹ at current density of 500 mA g⁻¹, and good cycling stability with 175 mAh g⁻¹ at current density of 2000 mA g⁻¹ over 400 cycles. The good cycling stability was attributed to unique grain-like MoS₂ structure, which promote dispersion very well and provide enough space to buff the volume change during charging/discharging process.

A three-dimensional hierarchical VS₂ spheres reported by J. Wang *et al.* [29] was synthesized through a one-step hydrothermal method without additive, which was formed by few-layered nanosheets. The VS₂ spheres, as anode for SIBs, delivered a

remarkable specific capacity of 720 mAh g⁻¹ at 0.2 A g⁻¹ after 100 cycles and excellent cycling stability with specific capacity of 565 mAh g⁻¹ at current density of 2 A g⁻¹ over 1000 cycle. The high specific capacity and good cycling stability were attributed to three-dimensional hierarchical structure, which could promote electrolyte diffusion and produce enough space for volume expansion during charging/discharging process. Besides, R. Sun et al. [37] synthesized layer-by-layer VS₂ stacked nanosheets (VS₂-SNSs) using a simple one-step hydrothermal method with polyvinylpyrrolidone as additive. As a result, VS₂-SNSs-based electrode exhibits a specific capacity of 250 mAh g⁻¹ at current density of 0.2 A g⁻¹, superb rate performance with 150 mAh g⁻¹ at current density of 20 A g⁻¹, and excellent cycling stability without capacity fading over 600 cycles at current density of 5 A g⁻¹. The stacked nanosheets possessed large surface area and stable structure, which could not provide more active sites for sodium ions storage and large electrode-electrolyte contact area for charge transfer but also prevent volume change during intercalation/deintercalation of Na⁺.

WS₂ hollow microspheres with large surface area were synthesized via a facile one-step hydrothermal method without additives [33]. It was found that WS₂ hollow microspheres, as anode for SIBs, possess a high specific capacity of 353.2 mAh g⁻¹ at current density of 0.2 A g⁻¹, and a long cycling stability of 285 mAh g⁻¹ after 2000 cycles at current density of 2 A g⁻¹. The superior electrochemical performance was assigned to the hollow structure consisted of nanosheets, which could shorten the pathway for Na⁺ diffusion and provide a large space for volume exchange during charging/discharging process.

SnS₂, as a kind of anode for SIBs, has attracted extensive attention due to high theoretical capacity from alloying reaction. At the same time, it also suffers large volume expansion during charging/discharging process, which cause poor cycling stability. SnS₂ nanosheet assemblies (SnS₂ NSA) were synthesized through solvothermal reaction with N-methyl-2-pyrrolidone as solvent, which is conducive to the formation of the nanostructure due to suitable surface energy [38]. Compare with commercial SnS₂ nanopowders, SnS₂ NSA shows a higher specific capacity. Furthermore, SnS₂ nanosheets assembled hierarchical tubular structures (SnS₂ NS \subset HTSs) have been fabricated by J. Zhao *et al.* via template sacrifice method using cobalt-nitrilotriacetic acid chelate nanowire as template [39]. When it is applied as anode material for SIBs, SnS₂ NS \subset HTSs based electrode delivers a high specific capacity of 708 mAh g⁻¹ at current density of 50 mA g⁻¹. After 50 cycles, a reversible capacity of 414 mAh g⁻¹ was still maintained, which is higher than that of commercial SnS₂ powder, demonstrating better electrochemical performance. The reasons of good performance of SnS₂ NS \subset HTSs are attributed to following three factors: first, the tubular structure can offer a continuous pathway for charge transport and buff the volume expansion; second, SnS₂ nanosheet can shorten the Na⁺ diffusion distance and increase the contact area between electrode and electrolyte; third, the edges with large interspace exposed on the unique hierarchical tubular structure could promote Na⁺ intercalation.

1.2.2 Structural engineering

As for structural engineering, such as making defects, expanding interlayer spacing, mixing 1T with 2H phases and designing plane, can provide more active sites for sodium ion storage, increase the electronic conductivity, facilitate sodium ion diffusion and so on, resulting in good electrochemical performance for MS₂ based materials.

(1) Making defects

A unique architecture of bundled defect-rich MoS₂ (BD-MoS₂) with large vacancies has been synthesized through a simple quenching process [40]. According to experimental results and DFT calculations, it is found that sodium ions can not only diffuse along the interlayers, but also can transport through vacancies, causing 3D diffusion with fast electrochemical kinetics. As a result, BD-MoS₂ based anode exhibited a long cycling life with high reversible capacity of 350 mAh g⁻¹ at current density of 2 A g⁻¹ after 1000 cycles and excellent rate performance with 262 mAh g⁻¹ at 5 A g⁻¹. Y. Li et al fabricated a hollow microcube framework constructed by Mo-defect-rich ultrathin MoS₂ nanosheets (HMF-MoS₂) via a zeolite-like-framework-engaged strategy [41]. The hollow structured HMF-MoS₂ showed a high reversible capacity of 384 mAh g⁻¹ at 100 mA g⁻¹ after 100 cycles and impressive cycling stability with 267 mAh g⁻¹ at 1 A g⁻¹. The results of experiments and DFT calculations revealed that abundant Mo vacancies in MoS₂ can not only effectively facilitate the charge transfer but also enhance the interaction between MoS₂ and sodium, improving capability of Na⁺ storage. Furthermore, DFT calculations performed by G. Barik et al demonstrated

that the vacancy in MoS₂ could improve the diffusion of Na⁺ at the defective region and specific capacity [42].

(2) Mixing 1T and 2H phases

Researchers want to improve the electrochemical performance of MoS₂-based anode by increasing the proportion of 1T phase in framework of MoS₂ due to its metallic conductivity. D. Sun et al synthesized ultrathin 1T MoS₂ nanosheets through thermal-driven Li-ion insertion assisted exfoliation [43]. The prepared 1T MoS₂, as anode for SIBs, possesses a high specific capacity of 450 mAh g⁻¹ at current density of 50 mA g⁻¹ and long cycling life with capacity retention of 94% at current density of 1 A g⁻¹ after 200 cycles. J. Wu et al fabricated a dual-phase MoS₂ (DP-MoS₂) via a simple solvothermal method, which contains 1T phase and 2H phase [44]. When DP-MoS₂ was used as anode for SIBs, a long cycling stability with a high specific capacity of 300 mAh g⁻¹ at current density of 0.5 A g⁻¹ after 200 cycles and outstanding rate performance with 200 mAh g⁻¹ at a current density of 5 A g⁻¹ were achieved. Compared with 2H MoS₂, both of works revealed that 1T phase in MoS₂ could effectively enhance the electronic conductivity and promote Na⁺ diffusion by experimental results and DFT calculations.

(3) Expanding interlayer spacing

Large interlayer spacing can store more sodium ion and provide ion migration channels to accelerate Na⁺ diffusion. Numerous works focus on expanding interlayer spacing to improve the specific capacity and rate performance of MoS₂-based anode. For instance, poly(ethylene oxide)-intercalated MoS₂ composites (PEO-MoS₂) have

been successfully synthesized by a simple exfoliation–restacking method to expand the interlayer spacing of MoS₂ [45]. After PEO intercalation, the interlayer spacing of 1.1 and 1.4 nm corresponding to single PEO layer intercalation (PEO_{1L}-MoS₂) and double PEO layers intercalation (PEO_{2L}-MoS₂) were observed, which were higher than that of commercial MoS₂ (0.62 nm). As a result, PEO_{2L}-MoS₂ based anode shows highest specific capacity and rate performance. MoS₂ nanowires with an expanded interlayer were synthesized by self-sacrificed template method when MoO₃ and a trace amount of (NH₄)₆Mo₇O₂₄•4H₂O were used as template and initiator, respectively [46]. The expanded interlayer spacing was 0.96 nm, which was due to intercalation of methylamine produced by (NH₄)₆Mo₇O₂₄•4H₂O. As anode for SIBs, it exhibited a high capacity of 200 mAh g⁻¹ at a current density of 0.1 A g⁻¹. Furthermore, Z. Gao et al presented MoS₂ nanofibers consisted of nanosheets with expanded interlayer spacing using polyvinyl pyrrolidone (PVP) as structure-directing agent [47]. It is found that the interlayer spacing was increased from 0.615 nm to 0.62-1.14 nm. The expanded interlayer spacing was attributed to the amorphous carbon between the interlayers, which is produced by decomposition of PVP during calcination process. L. Jing et al designed and fabricated a few-atomic-layered hollow nanospheres constructed from alternate intercalation of carbon and MoS₂ monolayers through hydrothermal method followed by heating treatment with in presence of hexadecyl trimethyl ammonium bromide (CTAB) [48]. The CTAB and (NH₄)₂Mo₇O₄ in distilled water will form bilayer-micellar vesicles as soft template. After that, (NH₄)₂Mo₇O₄ was adsorbed on the surfaces of these soft templates due to the high pressure followed by sulfurization to

form MoS₂ monolayer covered on the CTAB templates. In condition of high pressure, a new formed bilayer micelle could effectively prevent growth of MoS₂ along c-axis direction, which result in that a layer of MoS₂ were formed on the surface of second-layer micelle. Finally, alternately carbon layer intercalated MoS₂ hollow nanospheres was obtained after calcination at 800 °C for 2 h, causing large interlayer spacing of 1.08 nm. When it was used as anode for SIBs, it could deliver a high specific capacity of 401 mAh g⁻¹ at a current density of 0.2 A g⁻¹ and 262 mAh g⁻¹ even at a high current density of 2 A g⁻¹. The excellent electrochemical performance of above samples were attributed to the expanded interlayer spacing, which could improve the Na⁺ diffusion and storage capability.

(4) Designing plane

Designing plane was adopted to enhance the structural stability and promote Na⁺ transmission. In this case, MoS₂ nanobelts (NBs) with more exposed (002) plane edges on their flat surfaces reported by Z. Zhang et al was successfully synthesized via in situ sulfurization method using MoO₃ NBs as precursor [32]. Compared with conventional MoS₂ nanosheets, the MoS₂ NBs possessed abundant active edge sites for Na⁺ storage, short ions diffusion pathways for Na⁺ transmission and structural stability during intercalation/deintercalation processes. As a result, the MoS₂ NBs based electrode delivered a stable high reversible capacity with 520 and 380 mAh g⁻¹ at a current density of 1 A g⁻¹ and 20 A g⁻¹ after 100 cycles, respectively. In addition, vertically oriented MoS₂ on nitrogenous reduced graphene oxide sheets (VO-MoS₂/N-RGO) was presented by P. Li et al. [49] via a gel-precursor-based solvothermal method. The MoS₂

nanosheets with different length were prepared through controlling the heating rate. It is found that the length of MoS₂ synthesized at heating rate of 10 °C min⁻¹ (VO-MoS₂/N-RGO-10) was 30 nm, which was shorter than those of VO-MoS₂/N-RGO-30 (110nm prepared at heating rate of 30 °C min⁻¹) and VO-MoS₂/N-RGO-50 (190 nm prepared at heating rate of 50 °C min⁻¹). As anode for SIBs, the VO-MoS₂/N-RGO-10 based anode exhibited highest reversible capacity (255 mAh g⁻¹ at 0.2 A g⁻¹) and most outstanding rate performance (86 mAh g⁻¹ at 50 A g⁻¹) compared with those of VO-MoS₂/N-RGO-30 and VO-MoS₂/N-RGO-50 based ones. The excellent electrochemical performance was attributed to the short MoS₂ nanosheets, which could and reliver the deformation of the MoS₂ nanosheets and facilitate the diffusion of Na⁺.

1.2.3 Doping or combination with non-carbon materials

Commonly, doping or combination with non-carbon materials can be a classical strategy for developing SIBs, which can expand the interlayer spacing, increase the electronic conductivity, and/or enhance the structural stability, resulting in outstanding electrochemical performance.

(1) Doping

In order to develop SIBs, doping or combination with non-carbon materials were adopted to increase the electrochemical performance of MoS₂ based anodes. Mn-doped MoS₂ hollow nanotubes were synthesized via solvothermal method, which exhibited better electrochemical performance compared with bulk MoS₂ [50]. After Mn doped into framework of MoS₂, the expanded interlayer spacing was observed which promote

the diffusion of Na⁺, resulting in good performance. When used as anode for SIBs, a high specific capacity of 441 mAh g⁻¹ was achieved at a current density of 0.1 A g⁻¹ and a stable capacity of 160 mAh g⁻¹ after 1000 cycles was maintained at a current density of 1 A g⁻¹. In addition, G. Jia et al replaced sulfur with selenium to form MoS_{2-x}Se_x through calcination process with existence of selenium powder in a mixed Ar-H₂ atmosphere [51]. Y. Zhang et al also synthesized MoS_{2-x}Se_x by using selenizing treatment process [52]. The above two works demonstrated that MoS_{2-x}Se_x showed a better electrochemical performance compared with MoS₂, which could be attributed to expanded interlayer spacing, enhanced electronic conductivity and more defects after selenium substitution.

(2) Combination with non-carbon materials

Recently, numerous researchers focused on combination with non-carbon materials to enhance the electrochemical performance of MoS₂-based anodes. For instance, Bi₂S₃/MoS₂ heterogeneous with abundant phase boundaries was presented by L. Cao et al through a facile solvothermal method followed by sulfurization treatment [53]. Combination experimental results with DFT calculations, the abundant phase boundaries could form the interior self-built-in electric-field, which could improve the electrochemical kinetics and enhance the electronic conductivity. Furthermore, the Bi/Na₂S interface produced by conversion reaction was so stable due to the homogeneously distributed phase boundaries, which could effectively boost the reversible conversion/alloying reaction and prevent the agglomeration and pulverization of electrode. As a result, an excellent rate performance and outstanding

cycling stability with 323.4 mAh g⁻¹ at a high current density of 10 A g⁻¹ after 1200 cycles were achieved when Bi₂S₃/MoS₂ heterogeneous was used as anode for SIBs. The unique MoS₂/SnS hollow superassemblies (HSs) was fabricated via covalent assembly strategy using SnS nanodots as covalent linkages [54]. It was found that the covalent assembly structure could enhance the electron transfer between the across-interlayers, promote the Na⁺ diffusion, and strengthen the structural stability based on experimental characterization, DTF calculations, and mechanical simulations. Because of above merits, MoS₂/SnS HSs, as anode for SIBs, exhibited excellent electrochemical performance, such as high initial specific capacity of 1182 mAh g⁻¹ at 0.1 A g⁻¹, long cycling life with 634 mAh g⁻¹ at 5 A g⁻¹ after 100 cycles, and superb rate performance with 745 mAh g⁻¹ at 10 A g⁻¹.

W. Li et al synthesized the VS₂ microflowers coated by crystalline VOOH (*c*-VS₂@VOOH) through a simple one-step hydrothermal method as anode for SIBs [55]. As a result, *c*-VS₂@VOOH based anode exhibited a long cycling life (330 mAh g⁻¹ at 0.2 A g⁻¹ after 150 cycles) and excellent rate performance (224 mAh g⁻¹ at 1 A g⁻¹). Compared with VS₂ microflowers coated by amorphous VOOH (*a*-VS₂@VOOH) and pure VS₂, *c*-VS₂@VOOH possessed a better electrochemical performance, which were owing to the crystalline VOOH coating, resulting in fast Na⁺ diffusion and stable structural stability.

W. Ryu et al presented a heterogeneous tungsten sulfide (WS_x)/tungsten oxide (WO₃) core-shell nanofiber (NF) materials with vertically and randomly aligned thorn-bush features via electrospinning and reducing method followed by heating treatment

process in air [56]. As anode for SIBs, the obtained WS_x/WO_3 NFs based anode exhibited a remarkable second specific capacity of 791 mAh g^{-1} at 0.1 A g^{-1} and outstanding cycling stability after 100-cycle compared with WO_3 NFs and WS_x NFs. Such excellent electrochemical performance was attributed to the unique structure. The WS_2/WS_3 hierarchical grown on randomly aligned thorns could provide abundant storage sites for Na^+ . Furthermore, the WO_3 layer coated on surface of tungsten sulfide could prevent the sulfur dissolution, resulting in excellent performance.

Hollow SnO_2/SnS_2 hybrids have been synthesized by a simple two-step hydrothermal method [57]. Because of their unique structure, the obtained hollow SnO_2/SnS_2 hybrids delivered a high specific capacity of $485.64 \text{ mAh g}^{-1}$ at a current density of 300 mA g^{-1} after 100 cycles, which was approximately 25.9 % and 28.5 % higher than those of bare SnO_2 and SnS_2 , respectively.

1.2.4 Combination with carbon materials

Owing to the problems of low conductivity and large volume expansion in a large voltage range, MS_2 -based anodes suffer from agglomeration and pulverization during charging/discharging process, causing short cycling life and poor rate performance. In this case, carbon materials were selected to combine with MS_2 for enhancing the rate performance and cycling stability, due to their high electronic conductivity and good stability.

(1) MS_2 /carbon composite

MS₂/carbon composite is a widely used strategy to improve the electrochemical performance of the anode materials for SIBs. A 3D hierarchical microspheres constructed by ultrathin MoS₂-C nanosheets were synthesized by W. Zhang et al through hydrothermal method using cellulose nanocrystals (CNCs) as carbon source [58]. It was found that the ultrathin MoS₂-C nanosheets could effectively decrease the resistance between MoS₂ and carbon and buff the volume expansion during intercalation of Na⁺. As anode for SIBs, a long cycling life with 298.5 mAh g⁻¹ at 2 A g⁻¹ after 1000 cycles and excellent rate capability of 275 mAh g⁻¹ at 8 A g⁻¹ were achieved. H. Lim et al synthesized nitrogen self-doped MoS₂/carbon spheres (N-MoS₂/C) through a simple wet chemical-based synthesis method followed with carbonization process, using thioacetamide, MoCl₅, and furfural as S, Mo, and C sources [59]. The obtained N-MoS₂/C delivered a high specific capacity of 649 mAh g⁻¹ at 0.1 C and excellent cycling stability of 78% retention maintained after 200 cycle. A superior rate performance of 380 mAh g⁻¹ at 10 C was still achieved. The N-MoS₂ incorporated with porous carbon possessed large surface area, which could increase the electronic conductivity, enhance the mechanical properties, and improve the capability of Na⁺ storage. Hierarchically porous MoS₂-C hollow rhomboids (MCHRs) were synthesized by a simple self-templated solvothermal method, which exhibited outstanding electrochemical performance compared with pure MoS₂, because of the unique hollow architectures [60].

He' group reported VS₂ hollow flower spheres and reduced graphene oxide nanocomposites (VS₂ HFS/RGO), which was synthesized by a simple solvothermal

method [61]. The RGO exhibited high electronic conductivity, large specific area, and rich redox sites, which enhanced the conductivity of nanocomposites and caused high contribution of capacitive. Compared with VS₂ HFS based electrode, VS₂ HFS/RGO based electrode showed higher specific capacity (430 mAh g⁻¹ at 0.1 A g⁻¹) and better rate performance (143 mAh g⁻¹ at 2 A g⁻¹).

(2) Carbon supporting

Carbon supporting for MS₂ growth also can improve the electrochemical performance remarkably. T. Wu et al presented MoS₂ nanoflakes embedded on nitrogen-doping carbon nanotube (MoS₂/N-CNT) fabricated through alternating and hydrothermal approach using Mo metal as raw material [62]. As anode for SIBs, the obtained MoS₂/N-CNT electrode exhibited excellent electrochemical performance, such as high reversible capacity (486 mAh g⁻¹ at 200 mA g⁻¹ after 100 cycles), superior rate performance (332 mAh g⁻¹ at 10 A g⁻¹), and long cycling stability (337 mAh g⁻¹ with high retention of 83.6% after 800 cycles at 2 A g⁻¹). Such excellent performance was attributed to heteroatomic nitrogen doping which produce more active sites and ion diffusion spaces in N-CNT and bonds of C-O-Mo, C-S-Mo and C-O-S formed between MoS₂ and N-CNT which can improve the structural stability and promote the electronic transmission. MoS₂ sheet-like nanostructure grown on nitrogen-doped carbon polyhedral to form hierarchical composite nanospheres (CP@MoS₂ nanospheres) was designed and fabricated [63]. It was found that nitrogen doping could effectively enhance the electrical conductivity, porous structure can significantly buff the volume change during intercalation/deintercalation process, and the ultrathin MoS₂ nanosheets

can increase the contact area of electrolyte/electrode and promote the electron and ion transmission. As a result, a good rate capacity of 266 mAh g⁻¹ at 2 A g⁻¹ was retained and a reversible capacity of 337 mAh g⁻¹ was maintained after 300 cycles at 0.5 A g⁻¹.

Carbon nanofiber substrate anchored by bowl-like VS₂ nanosheet arrays (CNF@VS₂) were successfully fabricated via a simple one-step solvothermal method [64]. Due to the ultrathin thickness of bowl-like VS₂, metallic conductivity of VS₂, and interconnected array architecture, ultrafast Na⁺ transmission and without capacity attenuation below 0.3 V were achieved. DFT calculations revealed that VS₂/C interface exhibited a lower diffusion energy barrier than that of VS₂/VS₂ interface. Because of above merits, CNF@VS₂ based electrode delivered a high reversible capacity of 659 mAh g⁻¹ at 0.2 A g⁻¹, outstanding cycling capacity of 345 mAh g⁻¹ after 6000 cycles at 2 A g⁻¹, and superior rate capacity of 277 mAh g⁻¹ at a large current density of 20 A g⁻¹.

(3) Carbon coating

To prevent pulverization of MS₂-based electrode, carbon coating is widely applied in energy storage field. M. Hou et al fabricated a few-layered MoS₂ nanosheets spaced-confined in N-doped hollow nanospheres with mesoporous carbon shells (MoS₂@NHCS) as anode for SIBs [65]. The specific capacity of MoS₂@NHCS was 370 mAh g⁻¹ at current density of 1 A g⁻¹. Furthermore, at large current density of 2 A g⁻¹, reversible capacity of 351 mAh g⁻¹ with high retention of 94.9 % after 100 cycles was still retained. They also measured the structure of MoS₂@NHCS after cycling, the hollow structure was still maintained after 200 cycles. Thus, the hollow mesoporous carbon nanospheres can effectively keep the structural integrity and prevent the

pulverization of electrode during charging/discharging process. In addition, the N-doped carbon shell can enhance the conductivity and facilitate Na⁺ diffusion. A sandwich structure of nitrogen-doped carbon@MoS₂@polypyrrole (C@MoS₂@PPy) was designed and fabricated by using FeOOH@C as template [66]. When C@MoS₂@PPy was used as anode for SIBs, it delivered a high reversible capacity of 713 mAh g⁻¹ at 0.1 A g⁻¹ after 100 cycles and outstanding cyclin stability with stable capacity of 294 mAh g⁻¹ at 5 A g⁻¹ after 500 cycles, respectively. The excellent electrochemical performance was owing to unique structure. The N-doped carbon layer and PPy contacted with MoS₂ nanosheets through Mo-N bonds, which can effectively buff the volume expansion and prevent the aggregation and pulverization during charging/discharging process.

Few-layer SnS₂ nanosheets grown on nitrogen- and sulfur-doped carbon nanotube (NS-CNT) with amorphous carbon coating to form the carbon/SnS₂/NS-CNT was designed and fabricated by Z. Liu et al through a hydrogel-embedding method [67]. It was found that the N, S-doping could enhance the electronic conductivity of carbon-sandwiched SnS₂ nanosheets. From the results of in operando small-angle X-ray scattering and ex situ X-ray absorption, the obtained carbon-sandwiched SnS₂ nanosheets exhibited higher reversible capacity due to this unique structure compared with SnS₂ nanoparticles. As anode for SIBs, a high specific capacity of 471 mAh g⁻¹ at 50 mA g⁻¹ and superior rate capacity of 344 mAh g⁻¹ at 2.5 A g⁻¹ were achieved, demonstrating excellent electrochemical performance. Y. Liu et al synthesized a series of hollow carbon nanostructures confining SnS₂ ultrathin nanosheets, such as SnS₂

nanosheets confined in carbon nanotubes ($\text{SnS}_2@\text{CNTs}$), SnS_2 nanosheets confined in carbon nanoboxes ($\text{SnS}_2@\text{CNBs}$), and SnS_2 nanosheets confined in carbon nanospheres ($\text{SnS}_2@\text{CNSs}$), through a multistep templating method [68]. The obtained samples all showed an excellent electrochemical performance because of the merits of unique structure. In detail, the thin carbon shell could not only enhance the electronic conductivity, but also prevent the aggregation of SnS_2 nanosheets caused by large volume expansion during charging/discharging process. Furthermore, fast Na^+ diffusion was also achieved owing to the ultrathin SnS_2 nanosheets with large surface area, resulting in dominant capacitive contribution.

(4) $\text{MS}_2/\text{Carbon}$ heterostructure

Recently, MS_2/C heterostructure was designed and used to improve the electrochemical performance of electrode for SIBs. Z. Li et al designed and constructed a MoS_2/C composite with an inter-overlapped hierarchical structure ($\text{MoS}_2\text{-C@C}$) via a bottom-up synthesis method [69]. The alternately stacked MoS_2 and carbon structure resulted in expanded interlayer spacing of 1 nm, which was larger than those of $\text{MoS}_2@\text{C}$ (0.68 nm) nanorod and m- MoS_2 (0.63 nm). Furthermore, the carbon layer in heterostructure could keep the structural stability during intercalation/deintercalation process and promote the electron transfer. As anode for SIBs, the obtained $\text{MoS}_2\text{-C@C}$ showed an excellent electrochemical performance, such as high reversible capacity (590 mAh g^{-1} at 0.1 A g^{-1} after 100 cycles), an outstanding cycling stability (312 mAh g^{-1} at 2 A g^{-1} after 1000 cycles), and superior rate performance (164 mAh g^{-1} at 20 A g^{-1} and 51 mAh g^{-1} at 50 A g^{-1}). $\text{MoS}_2/\text{amorphous carbon microtubes}$ ($\text{MoS}_2/\text{C MTs}$) composed

of heterostructured MoS₂/C nanosheets were synthesized by a facile template approach [70]. The heterointerface of MoS₂/C MTs can significantly stabilize the structure during conversion reaction, promote the electron and Na⁺ transmission, and buff the volume expansion during intercalation of Na⁺. Consequently, a high reversible capacity of 563.5 mAh g⁻¹ at 0.2 A g⁻¹, a superior rate capacity of 401.3 mAh g⁻¹ at 10 A g⁻¹, and stable reversible capacity of 484.9 mAh g⁻¹ after 1500 cycles at 2 A g⁻¹ were achieved, revealing excellent electrochemical performance.

Sandwich-like SnS₂/graphene/SnS₂ (SnS₂/rGO/SnS₂) composite was synthesized via a facile one-step hydrothermal method, in which the ultrathin SnS₂ nanosheets were anchored on both sides of reduced graphene oxide through C-S bonds [30]. It was found that the interlayer spacing was ~0.803 nm after graphene inserting between SnS₂ sheets, which could promote the Na⁺ diffusion. The graphene between SnS₂ sheets also effectively prevent the restacking of SnS₂ nanosheets during intercalation/deintercalation process. The DTF calculation demonstrated that the interlayer spacing of sandwich-like structure is most stable. According to molecular simulation and experimental results, this state exhibited highest diffusion coefficient of Na⁺, resulting in fast Na⁺ transmission. When SnS₂/rGO/SnS₂ was used as anode for SIBs, it delivered a remarkable reversible capacity of 1133 mAh g⁻¹ at 0.1 A g⁻¹ after 100 cycles and superior rate capacity of 765 mAh g⁻¹ at 10 A g⁻¹.

1.3 Objectives of this study

Owing to limited lithium resource, it is significant to develop an anode with high performance for the commercialization of SIBs. Layered metal sulfides are considered as a promising anode for SIBs due to their merits compared with others anode. As mentioned above, in order to enhance the electrochemical performance of MS_2 based anode, morphology design, structural engineering, doping or combination with non-carbon materials, and carbon material modification are adopted, which can effectively provide more active sites for Na^+ storage, promote the Na^+ diffusion, and enhance the structural stability during charging/discharging process.

Unfortunately, even though above strategies are very effective, the synthesis processes of most are so complex and consume too much energy. Therefore, it is urgent to synthesize layered metal sulfides with a simple method. The main objective of this research is to synthesize MS_2 based anode with high electrochemical performance through a facile method.

1.4 Contents of this dissertation

This dissertation contains six chapters.

Chapter 1: The effective strategies such as morphology design, structural engineering, electrolyte selecting, doping or combination with non-carbon material and combination with carbon material for enhancing electrochemical performance of layered metal sulfide are comprehensively summarized and analyzed.

Chapter 2: The information of used chemical reagents, characterization and testing methods are introduced.

Chapter 3: Coral reef-like MoS₂ microspheres (MoS₂-MS) with 1T/2H phase is synthesized by a simple one-step hydrothermal method. Meanwhile, 2H phase MoS₂ is obtained via heating MoS₂-MS at 800 °C for 2h, which is named as MoS₂-MS-800. The morphology and structure of two samples are systematically characterized. Furthermore, the electrochemical performances of MoS₂-MS with 1T/2H phase and MoS₂-MS-800 with 2H phase were evaluated and compared.

Chapter 4: Vanadium is combined into the framework of MoS₂ to form VMoS₂ (VMS₂) through a facile one-step hydrothermal method. To explore the impact of V mediating, the electronic conductivity and electrochemical kinetics of VMS₂ and pure MoS₂ are measured. In addition, the energy barrier of sodium ion transportation in VMS₂ and pure MoS₂ are also calculated by density functional theory (DFT) calculations.

Chapter 5: A novel orderly layered VMoS₂ (OL-VMS) anode material is synthesized through a facile hydrothermal self-assembly method followed by a heating treatment process. The formation mechanism of the orderly layered structure is explored. Furthermore, electrochemical performances of OL-VMS at different voltage range are conducted. Finally, the cycling stabilities of orderly layered structure and flower-like structure are also measured and compared.

Chapter 6: General conclusions of this research, challenges and prospects for future work are introduced.

References

- [1] B. Dunn, H. Kamath, J.-M. Tarascon, Electrical energy storage for the grid: a battery of choices, *Science* 334 (2011) 928-935.
- [2] M. Reddy, G. Subba Rao, B. Chowdari, Metal oxides and oxysalts as anode materials for Li ion batteries, *Chem. Rev.* 113 (2013) 5364-5457.
- [3] Z. Yang, J. Zhang, M.C. Kintner-Meyer, X. Lu, D. Choi, J.P. Lemmon, J. Liu, Electrochemical energy storage for green grid, *Chem. Rev.* 111 (2011) 3577-3613.
- [4] W. Kang, Y. Wang, J. Xu, Recent progress in layered metal dichalcogenide nanostructures as electrodes for high-performance sodium-ion batteries, *J. Mater. Chem. A* 5 (2017) 7667-7690.
- [5] M. Armand, J.-M. Tarascon, Building better batteries, *nature* 451 (2008) 652-657.
- [6] Z. Hu, Q. Liu, S.L. Chou, S.X. Dou, Advances and challenges in metal sulfides/selenides for next-generation rechargeable sodium-ion batteries, *Adv. Mater.* 29 (2017) 1700606.
- [7] Jiajia Wang, Xiyan Yue, Zhengkun Xie, Abuliti Abudula and Guoqing Guan, MOFs-derived transition metal sulfide composites for advanced sodium ion batteries, *Energy Storage Mater.* 41 (2021) 404-426.
- [8] W. Luo, F. Shen, C. Bommier, H. Zhu, X. Ji, L. Hu, Na-ion battery anodes: materials and electrochemistry, *Accounts of chemical research* 49 (2016) 231-240.
- [9] H. Pan, Y.-S. Hu, L. Chen, Room-temperature stationary sodium-ion batteries for large-scale electric energy storage, *Energ. Environ. Sci.* 6 (2013) 2338-2360.

- [10] D. Kundu, E. Talaie, V. Duffort, L.F. Nazar, The emerging chemistry of sodium ion batteries for electrochemical energy storage, *Angewandte Chemie International Edition* 54 (2015) 3431-3448.
- [11] Y.E. Durmus, H. Zhang, F. Baakes, G. Desmaizieres, H. Hayun, L. Yang, M. Kolek, V. Küpers, J. Janek, D. Mandler, S. Passerini, Y. Ein-Eli, Side by side battery technologies with lithium-ion based batteries, *Adv. Energy Mater.* (2020) 2000089.
- [12] S. Chen, F. Wu, L. Shen, Y. Huang, S.K. Sinha, V. Srot, P.A. Aken, Joachim Maier, Y. Yu, Cross-linking hollow carbon sheet encapsulated CuP₂ nanocomposites for high energy density sodium-ion batteries, *ACS Nano* 12 (2018) 7018-7027.
- [13] J.-Y. Hwang, S.-T. Myung, Y.-K. Sun, Sodium-ion batteries: present and future, *Chemical Society reviews* 46 (2017) 3529-3614.
- [14] X. Hu, W. Zhang, X. Liu, Y. Mei, Y. Huang, Nanostructured Mo-based electrode materials for electrochemical energy storage, *Chemical Society reviews* 44 (2015) 2376-2404.
- [15] M.H. Han, E. Gonzalo, G. Singh, T. Rojo, A comprehensive review of sodium layered oxides: powerful cathodes for Na-ion batteries, *Energ. Environ. Sci.* 8 (2015) 81-102.
- [16] Y. Chen, X. Li, K. Park, W. Lu, C. Wang, W. Xue, F. Yang, J. Zhou, L. Suo, T. Lin, Nitrogen-doped carbon for sodium-ion battery anode by self-etching and graphitization of bimetallic MOF-based composite, *Chem* 3 (2017) 152-163.

- [17] L. Xiao, H. Lu, Y. Fang, M.L. Sushko, Y. Cao, X. Ai, H. Yang, J. Liu, Low-Defect and Low-Porosity Hard Carbon with High Coulombic Efficiency and High Capacity for Practical Sodium Ion Battery Anode, *Adv. Energy Mater.* 8 (2018) 1703238.
- [18] T. Li, A. Qin, L. Yang, J. Chen, Q. Wang, D. Zhang, H. Yang, In situ grown Fe₂O₃ single crystallites on reduced graphene oxide nanosheets as high performance conversion anode for sodium-ion batteries, *ACS Appl. Mater. Inter.* 9 (2017) 19900-19907.
- [19] L. Wang, Z. Wei, M. Mao, H. Wang, Y. Li, J. Ma, Metal oxide/graphene composite anode materials for sodium-ion batteries, *Energy Storage Mater.* 16 (2019) 434-454.
- [20] G. Fang, Z. Wu, J. Zhou, C. Zhu, X. Cao, T. Lin, Y. Chen, C. Wang, A. Pan, S. Liang, Observation of pseudocapacitive effect and fast ion diffusion in bimetallic sulfides as an advanced sodium-ion battery anode, *Adv. Energy Mater.* 8 (2018) 1703155.
- [21] L. Cao, X. Gao, B. Zhang, X. Ou, J. Zhang, W.-B. Luo, Bimetallic sulfide Sb₂S₃@FeS₂ hollow nanorods as high-performance anode materials for sodium-ion batteries, *ACS Nano* 14 (2020) 3610-3620.
- [22] W. Ma, K. Yin, H. Gao, J. Niu, Z. Peng, Z. Zhang, Alloying boosting superior sodium storage performance in nanoporous tin-antimony alloy anode for sodium ion batteries, *Nano Energy* 54 (2018) 349-359.
- [23] W.P. Kalisvaart, B.C. Olsen, E.J. Luber, J.M. Buriak, Sb–Si alloys and multilayers for sodium-ion battery anodes, *ACS Applied Energy Materials* 2 (2019) 2205-2213.

- [24] Y. Xiao, S.H. Lee, Y.K. Sun, The application of metal sulfides in sodium ion batteries, *Adv. Energy Mater.* 7 (2017) 1601329.
- [25] Y. Fang, D. Luan, X.W. Lou, Recent Advances on Mixed Metal Sulfides for Advanced Sodium-Ion Batteries, *Adv. Mater.* 32 (2020) 2002976.
- [26] P. Geng, S. Zheng, H. Tang, R. Zhu, L. Zhang, S. Cao, H. Xue, H. Pang, Transition metal sulfides based on graphene for electrochemical energy storage, *Adv. Energy Mater.* 8 (2018) 1703259.
- [27] D. Sun, D. Ye, P. Liu, Y. Tang, J. Guo, L. Wang, H. Wang, MoS₂/Graphene nanosheets from commercial bulky MoS₂ and graphite as anode materials for high rate sodium-Ion batteries, *Adv. Energy Mater.* 8 (2018) 1702383.
- [28] S. Xu, X. Gao, Y. Hua, A. Neville, Y. Wang, K. Zhang, Rapid deposition of WS₂ platelet thin films as additive-free anode for sodium ion batteries with superior volumetric capacity, *Energy Storage Mater.* 26 (2020) 534-542.
- [29] J. Wang, N. Luo, J. Wu, S. Huang, L. Yu, M. Wei, Hierarchical spheres constructed by ultrathin VS₂ nanosheets for sodium-ion batteries, *J. Mater. Chem. A* 7 (2019) 3691-3696.
- [30] Y. Jiang, D. Song, J. Wu, Z. Wang, S. Huang, Y. Xu, Z. Chen, B. Zhao, J. Zhang, Sandwich-like SnS₂/graphene/SnS₂ with expanded interlayer distance as high-rate lithium/sodium-ion battery anode materials, *ACS Nano* 13 (2019) 9100-9111.
- [31] J. Huang, Z. Wei, J. Liao, W. Ni, C. Wang, J. Ma, Molybdenum and tungsten chalcogenides for lithium/sodium-ion batteries: Beyond MoS₂, *J. Energy Chem.* 33 (2019) 100-124.

- [32] Z. Zhang, S. Wu, J. Cheng, W. Zhang, MoS₂ nanobelts with (002) plane edges-enriched flat surfaces for high-rate sodium and lithium storage, *Energy Storage Mater.* 15 (2018) 65-74.
- [33] J. Wang, L. Yu, Z. Zhou, L. Zeng, M. Wei, Template-free synthesis of metallic WS₂ hollow microspheres as an anode for the sodium-ion battery, *Journal of colloid and interface science* 557 (2019) 722-728.
- [34] D. Li, Q. Sun, Y. Zhang, L. Chen, Z. Wang, Z. Liang, P. Si, L. Ci, Surface-confined SnS₂@ C@ rGO as high-performance anode materials for sodium-and potassium-ion batteries, *ChemSusChem* 12 (2019) 2689-2700.
- [35] P. Wang, S. Sun, Y. Jiang, Q. Cai, Y.-H. Zhang, L. Zhou, S. Fang, J. Liu, Y. Yu, Hierarchical Microtubes Constructed by MoS₂ Nanosheets with Enhanced Sodium Storage Performance, *ACS Nano* 14 (2020) 15577-15586.
- [36] K. Yao, Z. Xu, Z. Li, X. Liu, X. Shen, L. Cao, J. Huang, Synthesis of grain-like MoS₂ for high-performance sodium-ion batteries, *ChemSusChem* 11 (2018) 2130-2137.
- [37] R. Sun, Q. Wei, J. Sheng, C. Shi, Q. An, S. Liu, L. Mai, Novel layer-by-layer stacked VS₂ nanosheets with intercalation pseudocapacitance for high-rate sodium ion charge storage, *Nano Energy* 35 (2017) 396-404.
- [38] Y. Wang, J. Zhou, J. Wu, F. Chen, P. Li, N. Han, W. Huang, Y. Liu, H. Ye, F. Zhao, Engineering SnS₂ nanosheet assemblies for enhanced electrochemical lithium and sodium ion storage, *J. Mater. Chem. A* 5 (2017) 25618-25624.
- [39] J. Zhao, X. Yu, Z. Gao, W. Zhao, R. Xu, Y. Liu, H. Shen, One step synthesis of SnS₂ nanosheets assembled hierarchical tubular structures using metal chelate

nanowires as a soluble template for improved Na-ion storage, *Chem. Eng. J.* 332 (2018) 548-555.

[40] K. Yao, Z. Xu, J. Huang, M. Ma, L. Fu, X. Shen, J. Li, M. Fu, Bundled defect-rich MoS₂ for a high-rate and long-life sodium-ion battery: achieving 3D diffusion of sodium ion by vacancies to improve kinetics, *Small* 15 (2019) 1805405.

[41] Y. Li, R. Zhang, W. Zhou, X. Wu, H. Zhang, J. Zhang, Hierarchical MoS₂ hollow architectures with abundant Mo vacancies for efficient sodium storage, *ACS Nano* 13 (2019) 5533-5540.

[42] G. Barik, S. Pal, Defect induced performance enhancement of monolayer MoS₂ for Li-and Na-ion batteries, *J. Phys. Chem. C* 123 (2019) 21852-21865.

[43] D. Sun, D. Huang, H. Wang, G.-L. Xu, X. Zhang, R. Zhang, Y. Tang, D. Abd El-Hady, W. Alshitari, A.S. AL-Bogami, 1T MoS₂ nanosheets with extraordinary sodium storage properties via thermal-driven ion intercalation assisted exfoliation of bulky MoS₂, *Nano Energy* 61 (2019) 361-369.

[44] J. Wu, J. Liu, J. Cui, S. Yao, M. Ihsan-Ul-Haq, N. Mubarak, E. Quattrocchi, F. Ciucci, J.-K. Kim, Dual-phase MoS₂ as a high-performance sodium-ion battery anode, *J. Mater. Chem. A* 8 (2020) 2114-2122.

[45] Y. Li, Y. Liang, F.C.R. Hernandez, H.D. Yoo, Q. An, Y. Yao, Enhancing sodium-ion battery performance with interlayer-expanded MoS₂-PEO nanocomposites, *Nano Energy* 15 (2015) 453-461.

[46] W. Ye, F. Wu, N. Shi, H. Zhou, Q. Chi, W. Chen, S. Du, P. Gao, H. Li, S. Xiong, Metal-Semiconductor Phase Twinned Hierarchical MoS₂ Nanowires with Expanded

Interlayers for Sodium-Ion Batteries with Ultralong Cycle Life, *Small* 16 (2020) 1906607.

[47] Z. Gao, X. Yu, J. Zhao, W. Zhao, R. Xu, Y. Liu, H. Shen, Synthesis of long hierarchical MoS₂ nanofibers assembled from nanosheets with an expanded interlayer distance for achieving superb Na-ion storage performance, *Nanoscale* 9 (2017) 15558-15565.

[48] L. Jing, G. Lian, F. Niu, J. Yang, Q. Wang, D. Cui, C.-P. Wong, X. Liu, Few-atomic-layered hollow nanospheres constructed from alternate intercalation of carbon and MoS₂ monolayers for sodium and lithium storage, *Nano Energy* 51 (2018) 546-555.

[49] P. Li, J.Y. Jeong, B. Jin, K. Zhang, J.H. Park, Vertically Oriented MoS₂ with Spatially Controlled Geometry on Nitrogenous Graphene Sheets for High-Performance Sodium-Ion Batteries, *Adv. Energy Mater.* 8 (2018) 1703300.

[50] T. Zheng, G. Li, J. Dong, Q. Sun, X. Meng, Self-assembled Mn-doped MoS₂ hollow nanotubes with significantly enhanced sodium storage for high-performance sodium-ion batteries, *Inorganic Chemistry Frontiers* 5 (2018) 1587-1593.

51] G. Jia, D. Chao, N.H. Tiep, Z. Zhang, H.J. Fan, Intercalation Na-ion storage in two-dimensional MoS_{2-x}Se_x and capacity enhancement by selenium substitution, *Energy Storage Mater.* 14 (2018) 136-142.

[52] Y. Zhang, H. Tao, S. Du, X. Yang, Conversion of MoS₂ to a Ternary MoS_{2-x}Se_x Alloy for High-Performance Sodium-Ion Batteries, *ACS Appl. Mater. Inter.* 11 (2019) 11327-11337.

- [53] L. Cao, X. Liang, X. Ou, X. Yang, Y. Li, C. Yang, Z. Lin, M. Liu, Heterointerface Engineering of Hierarchical Bi₂S₃/MoS₂ with Self-Generated Rich Phase Boundaries for Superior Sodium Storage Performance, *Adv. Funct. Mater.* 30 (2020) 1910732.
- [54] J. Ru, T. He, B. Chen, Y. Feng, L. Zu, Z. Wang, Q. Zhang, T. Hao, R. Meng, R. Che, Covalent Assembly of MoS₂ Nanosheets with SnS Nanodots as Linkages for Lithium/Sodium-Ion Batteries, *Angewandte Chemie International Edition* 59 (2020) 14621-14627.
- [55] W. Li, J. Huang, L. Feng, L. Cao, Y. Feng, H. Wang, J. Li, C. Yao, Facile in situ synthesis of crystalline VOOH-coated VS₂ microflowers with superior sodium storage performance, *J. Mater. Chem. A* 5 (2017) 20217-20227.
- [56] W.-H. Ryu, H. Wilson, S. Sohn, J. Li, X. Tong, E. Shaulsky, J. Schroers, M. Elimelech, A.D. Taylor, Heterogeneous WS_x/WO₃ thorn-bush nanofiber electrodes for sodium-ion batteries, *ACS Nano* 10 (2016) 3257-3266.
- [57] K. Wang, Y. Huang, X. Qin, M. Wang, X. Sun, M. Yu, Synthesis of hollow SnO₂/SnS₂ hybrids and their application in sodium-ion batteries, *ChemElectroChem* 4 (2017) 2308-2313.
- [58] W. Zhang, H. Zhou, Z. Huang, S. Li, C. Wang, H. Li, Z. Yan, T. Hou, Y. Kuang, 3D hierarchical microspheres constructed by ultrathin MoS₂-C nanosheets as high-performance anode material for sodium-ion batteries, *J. Energy Chem.* 49 (2020) 307-315.

- [59] H. Lim, H. Kim, S.-O. Kim, W. Choi, Self-assembled N-doped MoS₂/carbon spheres by naturally occurring acid-catalyzed reaction for improved sodium-ion batteries, *Chem. Eng. J.* 387 (2020) 124144.
- [60] L. Han, S. Wu, Z. Hu, M. Chen, J. Ding, S. Wang, Y. Zhang, D. Guo, L. Zhang, S. Cao, Hierarchically porous MoS₂-carbon hollow rhomboids for superior performance of the anode of sodium-ion batteries, *ACS Appl. Mater. Inter.* 12 (2020) 10402-10409.
- [61] H. Qi, L. Wang, T. Zuo, S. Deng, Q. Li, Z.H. Liu, P. Hu, X. He, Hollow Structure VS₂@ Reduced Graphene Oxide (RGO) Architecture for Enhanced Sodium-Ion Battery Performance, *ChemElectroChem* 7 (2020) 78-85.
- [62] T. Wu, M. Jing, Y. Liu, X. Ji, Binding low crystalline MoS₂ nanoflakes on nitrogen-doped carbon nanotube: towards high-rate lithium and sodium storage, *J. Mater. Chem. A* 7 (2019) 6439-6449.
- [63] F. Tu, Y. Han, Y. Du, X. Ge, W. Weng, X. Zhou, J. Bao, Hierarchical nanospheres constructed by ultrathin MoS₂ nanosheets braced on nitrogen-doped carbon polyhedra for efficient lithium and sodium storage, *ACS Appl. Mater. Inter.* 11 (2018) 2112-2119.
- [64] D. Xu, H. Wang, R. Qiu, Q. Wang, Z. Mao, Y. Jiang, R. Wang, B. He, Y. Gong, D. Li, Coupling of bowl-like VS₂ nanosheet arrays and carbon nanofiber enables ultrafast Na⁺-Storage and robust flexibility for sodium-ion hybrid capacitors, *Energy Storage Mater.* 28 (2020) 91-100.
- [65] M. Hou, Y. Qiu, G. Yan, J. Wang, D. Zhan, X. Liu, J. Gao, L. Lai, Aging mechanism of MoS₂ nanosheets confined in N-doped mesoporous carbon spheres for sodium-ion batteries, *Nano Energy* 62 (2019) 299-309.

- [66] G. Wang, X. Bi, H. Yue, R. Jin, Q. Wang, S. Gao, J. Lu, Sacrificial template synthesis of hollow C@ MoS₂@ PPy nanocomposites as anodes for enhanced sodium storage performance, *Nano Energy* 60 (2019) 362-370.
- [67] Z. Liu, A. Daali, G.-L. Xu, M. Zhuang, X. Zuo, C.-J. Sun, Y. Liu, Y. Cai, M.D. Hossain, H. Liu, Highly reversible sodiation/desodiation from a carbon-sandwiched SnS₂ nanosheet anode for sodium ion batteries, *Nano Lett.* 20 (2020) 3844-3851.
- [68] Y. Liu, X.-Y. Yu, Y. Fang, X. Zhu, J. Bao, X. Zhou, X.W.D. Lou, Confining SnS₂ ultrathin nanosheets in hollow carbon nanostructures for efficient capacitive sodium storage, *Joule* 2 (2018) 725-735.
- [69] Z. Li, S. Liu, B.P. Vinayan, Z. Zhao-Karger, T. Diemant, K. Wang, R.J. Behm, C. Kuebel, R. Klingeler, M. Fichtner, Hetero-layered MoS₂/C composites enabling ultrafast and durable Na storage, *Energy Storage Mater.* 21 (2019) 115-123.
- [70] Q. Pan, Q. Zhang, F. Zheng, Y. Liu, Y. Li, X. Ou, X. Xiong, C. Yang, M. Liu, Construction of MoS₂/C hierarchical tubular heterostructures for high-performance sodium ion batteries, *ACS Nano* 12 (2018) 12578-12586.

CHAPTER 2 Experimental

2.1 Reagent information

Table 2.1 Reagent information for experiment

Regents	Grade	Company
Sodium trifluoromethanesulfonate (NaCF ₃ SO ₃)	98.0%	Sigma-Aldrich
Diglyme (DGM)	Anhydrous, 99.5%	Sigma-Aldrich
Sodium molybdate dihydrate (NaMoO ₄ •2H ₂ O)	≥99.0%	Sigma-Aldrich
Ammonium metavanadate	≥99.0%	Sigma-Aldrich
Ammonia solution (NH ₃ •H ₂ O)	28.0-30.0%	Wako
Sodium	99.9%	Sigma-Aldrich
Carboxymethylcellulose sodium (CMC)	High viscosity	Sigma-Aldrich
1-Methyl-2-pyrrolidinone (NMP)		MTI Corp.
Polyvinylidene Fluoride (PVDF)		MTI Corp.
Super P		MTI Corp.

2.2 Characterizations

2.2.1 Scanning electron microscope (SEM)

Morphology of the sample was observed using a scanning electron microscope (SU8010, Hitachi, Japan) at an operation voltage of 15.0 kV.

2.2.2 Energy dispersive spectrometer (EDS)

Elemental distribution analysis was carried out using a scanning electron microscope (SU8010, Hitachi, Japan) at an operation voltage of 15.0 kV with an energy dispersive spectrometer (EDS),

2.2.3 Transmission electron microscope (TEM)

The nanostructure was observed using a high-resolution transmission electron microscope (TEM, JEM-2100F, JEOL, Japan) with an accelerating voltage of 200 kV.

2.2.4 X-ray diffractometer (XRD)

Crystalline structure was analyzed by an X-ray diffractometer (XRD, Smartlab 9kW, Rigaku, Japan) with CuK α ($\lambda=1.5418 \text{ \AA}$) as the radiation source.

2.2.5 X-ray photoelectron spectrometer (XPS)

The elemental compositions and chemical valence states were determined by an X-ray photoelectron spectrometer (XPS) (VG ESCALAB 250, Thermo Electron, UK) using an Al K α X-ray source (1486 eV).

2.2.6 Raman

Raman spectra were collected with a Renishaw inVia Raman spectrometer using an excitation wavelength of 532 nm.

2.3 Electrochemical measurement

Charge/discharge measurements were carried out at various current densities over a voltage range of 0.3-3 V using a battery test system (LAND CT2001A model, Wuhan LAND Electronic. Ltd). Cyclic voltammographs (CVs) were recorded on an electrochemistry workstation at a scan rate of 0.1 mV s⁻¹. Electrochemical impedance spectra (EIS) were collected over a frequency range of 0.01 Hz-100 kHz.

CHAPTER 3 Coral reef-like microspheres with 1T/2T phase as high performance anode material for sodium ion batteries

3.1 Introduction

Sodium ion batteries (SIBs), which could replace lithium ion batteries (LIBs) in the future, have drawn increasing attention due to their similar electrochemical performances as LIBs, and low price and abundance of sodium element[1-4]. However, the anode materials of LIBs cannot be used directly as those for SIBs because of the larger radius of Na^+ than that of Li^+ [5, 6]. Thus, it is necessary to seek more suitable anode materials for the SIBs. Recently, many researchers focused on the two-dimensional (2D) transition layered metal dichalcogenides (TMDs) such as MoS_2 [7], VS_2 [8], SnS_2 [9] and WS_2 [10] with the weak van der Waals force between the layers since their structures are benefit for the Na^+ ion intercalation. Among these materials, the low cost MoS_2 with the large interlayer spacing has a high theoretical capacity (670 mAh g^{-1}) so that it has attracted wide attention as the anode for SIBs[11-13]. Unfortunately, pure MoS_2 has poor electronic conductivity and sluggish kinetics during the process of Na^+ ion diffusion, which greatly limit the cycling stability and rate performance of the SIBs[14-16].

In order to solve these issues, various efficient strategies have been taken to improve the electrochemical performance of MoS_2 -based anode. As a general strategy, nanostructure designs such as morphology changing, hollow structuring, interlayer space expanding, and nanosizing are extensively applied for enhancing the

electrochemical performance by providing more active sites and shortening ion diffusion path[17-22]. For instances, Zhang *et al.* reported that MoS₂ nanoblets with rich 002 plane edges exhibited specific capacities in the range of 520-540 mAh g⁻¹ even after 100 cycles at a current density of 1 A g⁻¹[20]. Meanwhile, combination of MoS₂ with the conductive materials to increase the conductivity and to form stable structure for the minimization of the volume expansion effect has also been proposed to enhance the performance of MoS₂-based anodes [7, 23-28]. Jing *et al.* synthesized few-atomic-layered MoS₂ hollow nanosphere with expanded interlayer spacing, and found that it delivered a stable capacity of 320 mAh g⁻¹ over 350 cycles at a current density of 1 A g⁻¹[7]. However, although the above strategies resulted in advantages to improve the anode performance, the fabrication methods were complex and always needed high temperature calcination. Thus, it is necessary to develop facile ways to obtain high-performance MoS₂-based anode materials.

In this work, coral reef-like MoS₂ microspheres (MoS₂-MS) with 1T/2H phase was synthesized by a simple one-step hydrothermal method and used as the anode material for SIBs. Since it had disordered structure with rich defects and large interlayer spacing, the obtained MoS₂-MS-based anode showed high electrochemical performance with a stable specific capacity of 467 mAh g⁻¹ at a current density of 100 mA g⁻¹ even after 100-cycle testing. Moreover, it also exhibited good cycling stability and excellent rate performance. After 500-cycle testing at 1 A g⁻¹, the specific capacity still stably maintained at 412 mAh g⁻¹. In addition, even at a high current density of 20 A g⁻¹, the MoS₂-MS-based anode delivered a specific capacity of 100 mAh g⁻¹. It is

confirmed that the disordered structure with 1T/2H phase could enhance the electrical conductivity to improve the rate performance, the rich defects provide more active sites for Na⁺ storage, and the large interlayer spacing allow rapid diffusion of the Na⁺ ions when the obtained MoS₂-MS was used as the anode material for SIBs.

3.2 Experimental

3.2.1 Synthesis of MoS₂-MS and MoS₂-MS-800

MoS₂-MS was synthesized through a hydrothermal method. Firstly, 1.5 mmol of Na₂MoO₄·H₂O was dissolved in the mixture of 30 ml of distilled water and 2 ml of ammonia solution. Then, 12 mmol of C₂H₅NS (TAA) was added into the above solution with ultrasonic treatment. Thereafter, the solution was transferred to a 50 ml Teflon-lined sealed autoclave and heated at 220 °C for 24 h. The obtained product was collected by centrifugation and washed several times using distilled water and ethanol successively. Finally, the products were dried at 80 °C in a vacuum oven for 12 h. For comparison, MoS₂-MS-800 was obtained by calcining the MoS₂-MS at 800 °C for 2 h under an Argon gas flow.

3.2.2 Materials characterizations

Morphology of the sample was observed using a scanning electron microscope (SU8010, Hitachi, Japan) at an operation voltage of 15.0 kV and the nanostructure was detected using a high-resolution transmission electron microscope (TEM, JEM-2100F, JEOL, Japan) with an accelerating voltage of 200 kV. X-ray diffraction (XRD) pattern was obtained on an X-ray diffractometer (Smartlab 9 kW, Rigaku, Japan) with CuKα

($\lambda=1.5418 \text{ \AA}$) as the radiation source. The elemental composition and valence states were determined by an X-ray photoelectron spectrometer (XPS) (VG ESCALAB 250, Thermo Electron, UK) using an Al Ka X-ray source (1486 eV). Raman spectrum was collected with a Renishaw inVia Raman spectrometer using an excitation wavelength of 633 nm.

3.2.3 Electrochemical measurements

Electrochemical properties of MoS₂-MS and MoS₂-MS-800 as the anode material for SIBs were evaluated by a galvanostatic charging/discharging method. Before testing, the active material was dried under vacuum at 80 °C over 12 h. For the preparation of the working electrode, 80 wt% of active material, 10 wt% of conductive carbon black and 10 wt% of sodium carboxymethylcellulose (CMC) were dissolved and mixed in deionized water at first. The obtained slurry was pasted onto a copper foil (CF) and dried in a vacuum oven at 80 °C overnight. The loading amount of active material on the CF was $\sim 0.9 \text{ mg cm}^{-2}$. Sodium metal and glass fiber were used as the counter electrode and the separator, respectively, and the electrolyte was 1 M sodium trifluoromethanesulfonate (NaSO₃CF₃) in diglyme (DGM). The cell was assembled in an argon-filled glove box. Charging/discharging measurements were carried out at various current densities over a voltage range of 0.3-3 V using a battery test system (LAND CT2001A model, Wuhan LAND Electronic. Ltd). Cyclic voltammographs (CVs) were recorded on an electrochemistry workstation at a scan rate of 0.1 mV s⁻¹. Electrochemical impedance spectra (EIS) were collected over a frequency range of 0.01 Hz-100 kHz.

3.3 Results and discussion

3.3.1 Characterization of MoS₂-MS and MoS₂-MS-800

Figures. 3.1a-c displays the SEM images of MoS₂-MS. One can see that the obtained MoS₂-MS had coral reef-like sphere shape with the nanosheet structure in it. Meanwhile, after the calcination, as shown in Figures. 3.2a-c, the obtained MoS₂-MS-800 remained unchanged particle shape when compared with that of MoS₂-MS. Figure 3.1d shows the energy disperse spectroscopic (EDS) elemental mapping of MoS₂-MS, which demonstrated the existence of Mo and S elements. The nanostructures of MoS₂-MS and MoS₂-MS-800 were further analyzed by TEM as shown in Figures 3.1e-i and Figure 3.2d-g. Obviously, the interlayer spacings corresponding to (002) plane of MoS₂-MS (either 0.65 or 0.64 nm, Figures 3.1e and h) were larger than that of MoS₂-MS-800 (0.615 nm, Figure 3.2e). The larger interlayer spacing may be caused by the insertion of NH₄⁺ and Na⁺ into the 002 plane of MoS₂ during the hydrothermal process[29]. After calcination, the interlayer spacing of MoS₂-MS-800 decrease to 0.615 nm, which can be ascribed to the arrangement of the crystal structure in MoS₂-MS-800[30]. Moreover, disordered structure with more defects were observed in MoS₂-MS (Figures 3.1h and i) than that in MoS₂-MS-800 (Figures 3.2e and f). Furthermore, as shown in Figures 3.1f and i, the 1T and 2H phases were found to be co-existed in MoS₂-MS with the more disordered structure whereas a uniform structure corresponding to 2H phase (Figure 3.2g) was observed in MoS₂-MS-800, indicating that MoS₂-MS-800 had a higher crystallinity than MoS₂-MS.

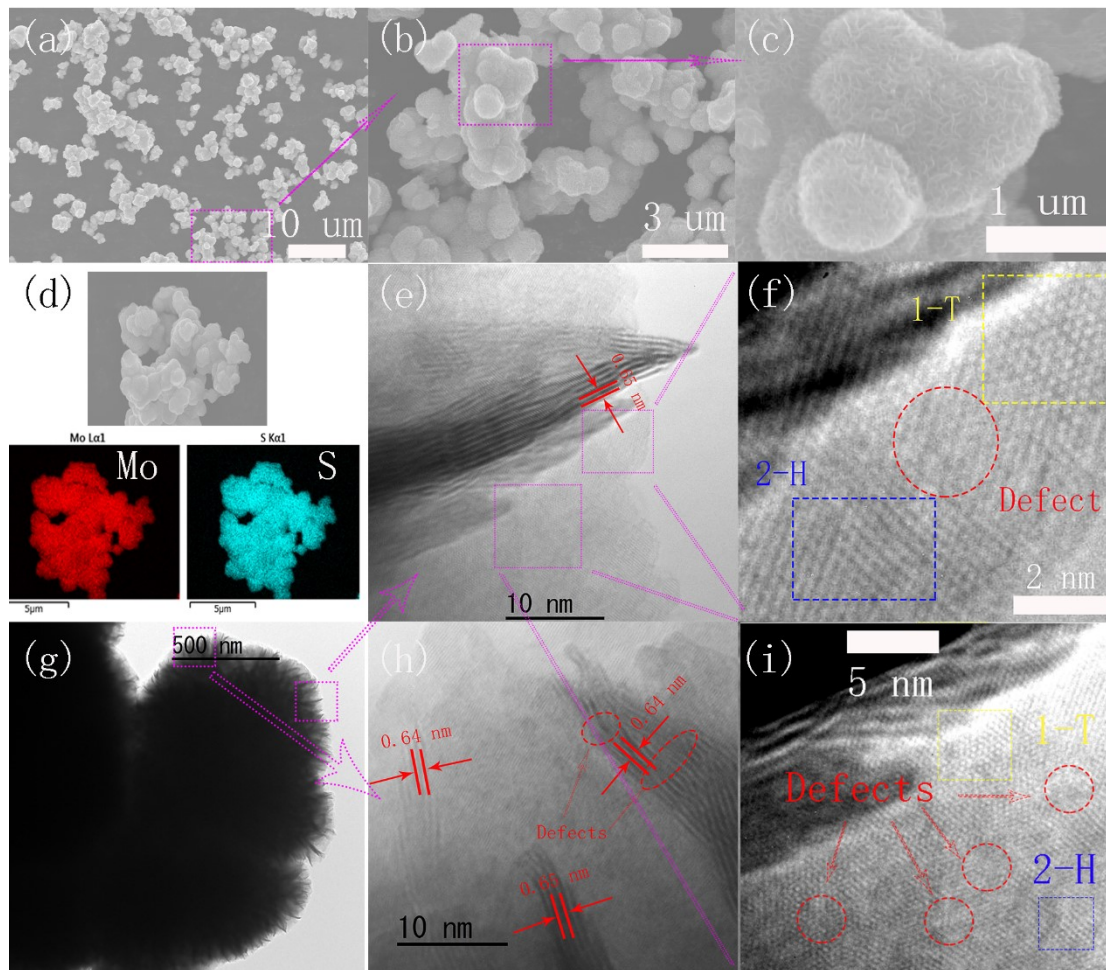


Figure 3.1 (a), (b) and (c) SEM morphologies of the MoS₂-MS. (d) elemental mapping images of MoS₂-MS. (g) TEM image of MoS₂-MS; (e), (f), (h) and (i) HRTEM images of the MoS₂-MS.

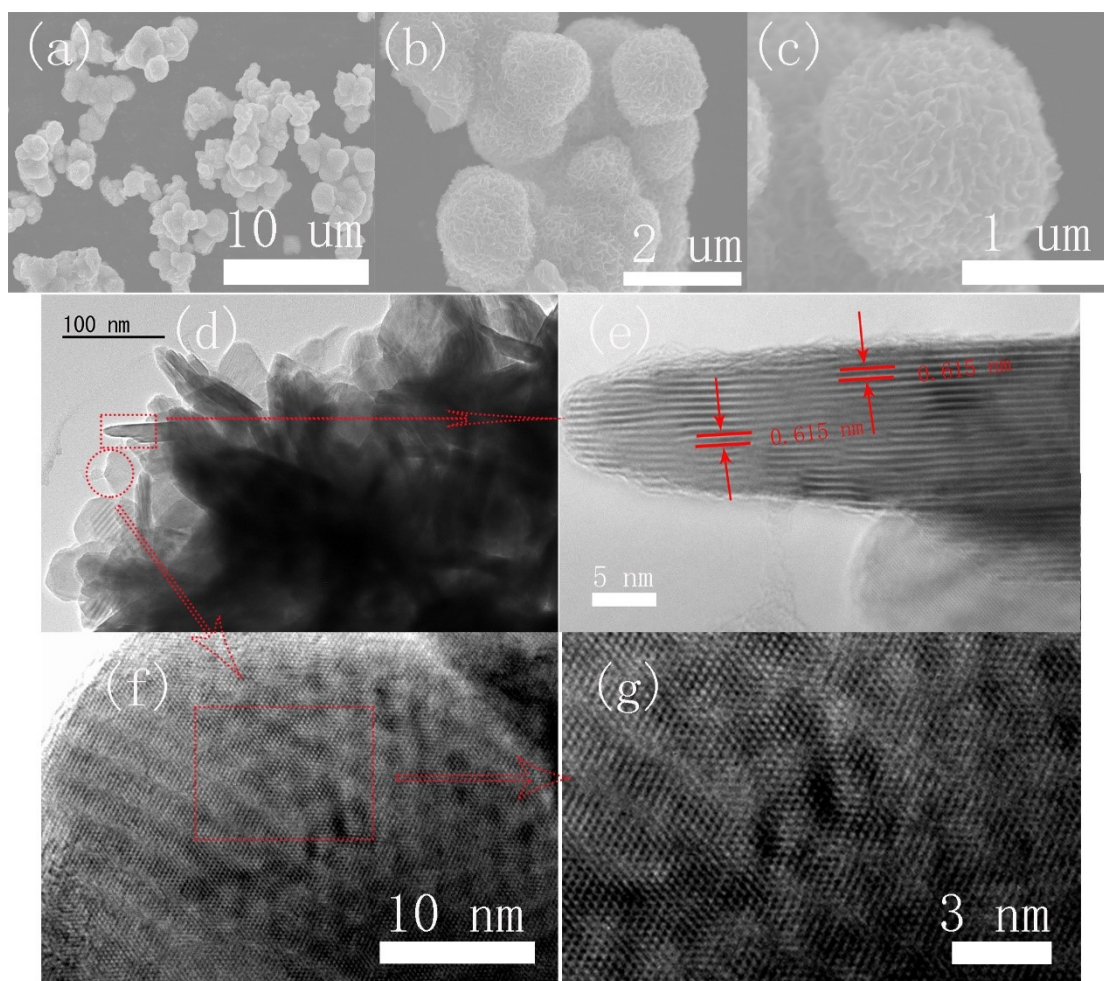


Figure 3.2 (a), (b) and (c) SEM morphologies of the MoS₂-MS-800. (d) TEM image of MoS₂-MS-800; (e), (f), and (g) HRTEM images of the MoS₂-MS-800.

Figure 3.3a shows XRD patterns of MoS₂-MS and MoS₂-MS-800. The diffraction peaks appeared at 14.32°, 33.83°, 39.43°, and 58.33° assigned to the (002), (100), (103) and (110) planes of 2H phase of MoS₂ (JCPDS No. 37-1492) were obviously observed for MoS₂-MS-800. Especially, based on the main diffraction peak at 14.32°, the interlayer distance of MoS₂ was calculated to be 0.618 nm, which is in good agreement with the HRTEM observation (Figure 3.2e). In comparison, only two broad peaks at 32.5° and 56.4° appeared in the XRD pattern of MoS₂-MS, indicating the much lower crystallinity of MoS₂-MS than MoS₂-MS-800. This result is consistent with TEM

analysis results. Figure 3.3b shows the Raman spectra of the as-prepared MoS₂-MS and MoS₂-MS-800. One can see that there were three peaks located at ~ 149, 224 and 345 cm⁻¹, which are belonged to the J₁, J₂ and J₃ peaks of 1T-phase MoS₂, respectively[31-33]. In addition, another two peaks at ~ 373 and 403 cm⁻¹ correspond to the in-plane Mo-S mode (E_{2g}¹) and out-plane Mo-S mode (A_{1g}) modes of 2H-MoS₂, respectively[34]. The Raman results demonstrate that 1T and 2H phases co-exist in structure of MoS₂-MS, which is in good agreement with the HRTEM observation (Figure 3.1f and i). After calcination, the peaks at ~ 149, 224 and 345 cm⁻¹ disappear for MoS₂-MS-800, indicating that 1-T phase existed in MoS₂-MS was changed to 2-H phase.

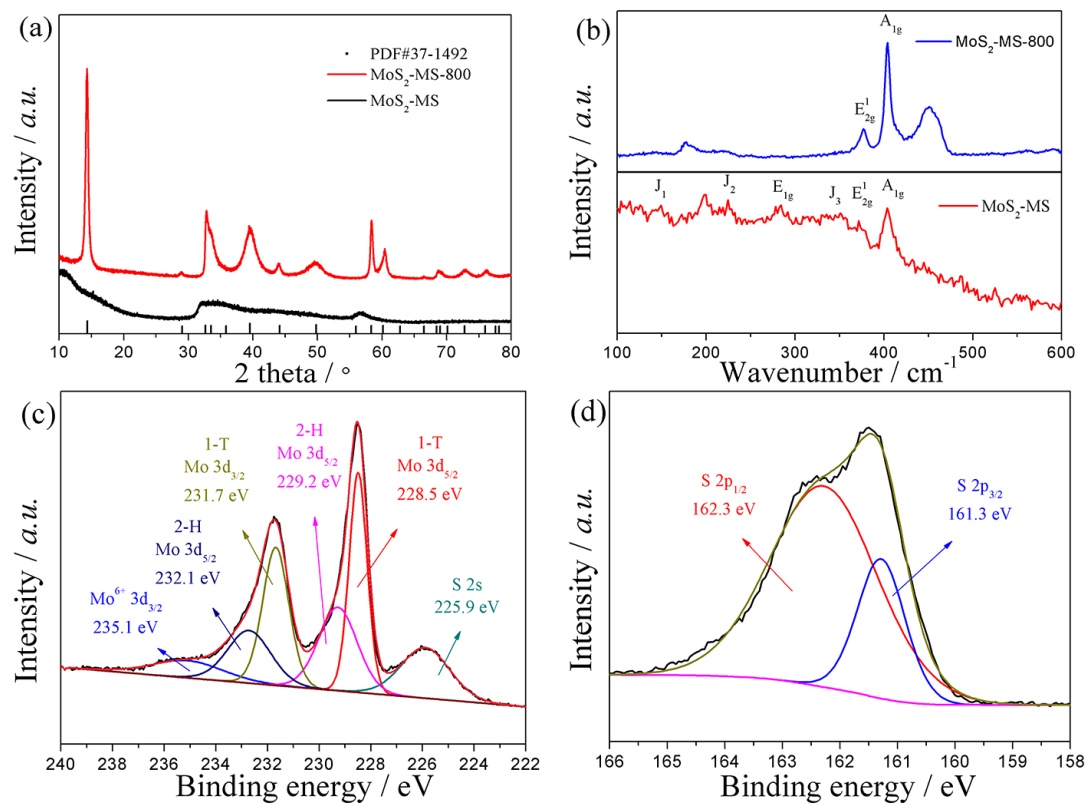


Figure 3.3 (a) XRD patterns of MoS₂-MS and MoS₂-MS-800. (b) Raman spectra of MoS₂-MS and MoS₂-MS-800. High-resolution XPS spectra of the (c) Mo 3d peak and (d) S 2p peak in MoS₂-MS.

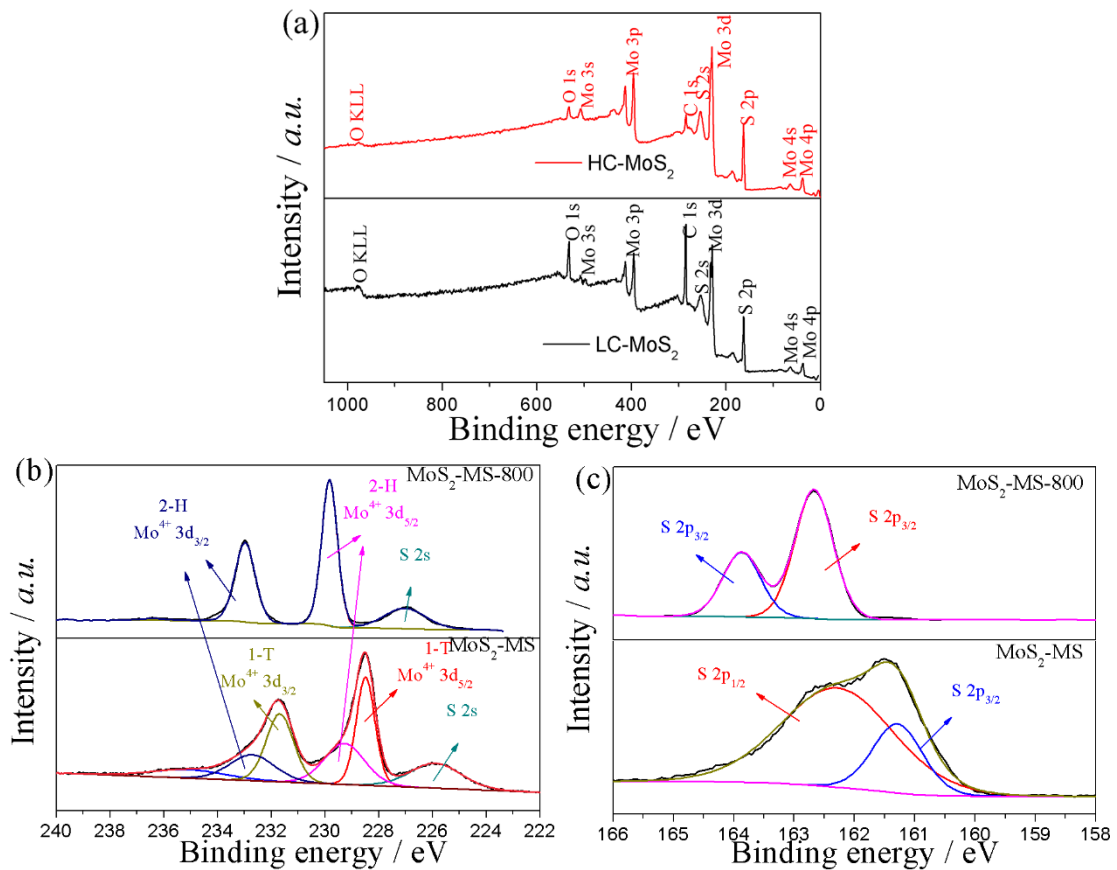


Figure 3.4 (a) XPS survey spectra of MoS₂-MS and MoS₂-MS-800. Comparison of high-resolution XPS spectra of Mo 3d (b) and S 2p (c).

Figure 3.4a shows XPS survey spectra of MoS₂-MS-800 and MoS₂-MS. The survey spectra demonstrated the presence of Mo and S elements in both of them. Figure 3.3c displays the high-resolution XPS spectra of Mo 3d peak for MoS₂-MS. Herein, the two peaks located at 228.5 and 231.7 eV attributed to Mo⁴⁺ 3d_{5/2} and Mo⁴⁺ 3d_{3/2} of 1-T phase[35, 36], respectively, which also confirmed the existence of 1-T phase in the MoS₂-MS. The result is also in good agreement with the HRTEM observation (Figure 3.1c). According to the XPS peak fitting, the concentration of 1-T phase in MoS₂-MS was 64.5 %. Meanwhile, two small peaks at 235.1 and 225.9 eV corresponding to Mo⁶⁺ and S 2s [37, 38] were also found (Figure 3.3c). In addition, two peaks at 161.3 and 162.3 eV in the high-resolution XPS spectrum of S 2p were assigned to S 2p_{3/2} and S

2p_{1/2}, respectively[39]. Moreover, the Mo 3d and S 2p spectra of MoS₂-MS and MoS₂-MS-800 are compared in Figure 3.4b and c. It is worth noting that the locations of the Mo 3d and S 2p peaks of MoS₂-MS shifted to higher binding energies after calcination, which revealed that 1-T phase existed in MoS₂-MS changed to 2-H phase after the calcination[35, 36]. This result is also consistent with the HRTEM observations (Figure 3.1f and Figure 3.2g).

3.3.2 Electrochemical performance

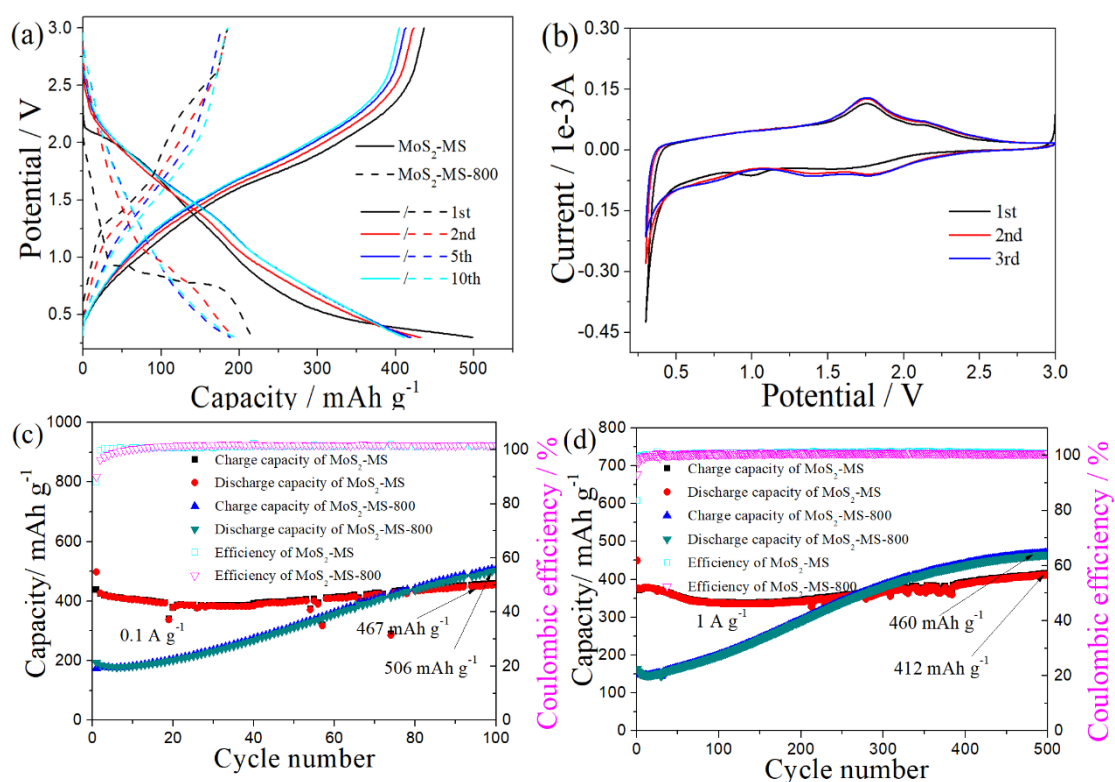


Figure 3.5 (a) Typical galvanostatic charging/discharging profiles for the the 1st, 2nd, 5th and 10th cycles at a current density of 100 mA g⁻¹ for MoS₂-MS and MoS₂-MS-800 based anodes; (b) Typical CV curves of MoS₂-MS based anode for the first 3 cycles at a scanning rate of 0.1 mV s⁻¹ in the voltage range of 0.3–3 V; and cycling performances

of MoS₂-MS and MoS₂-MS-800-based anodes at current rates of (c) 100 mA g⁻¹ and (d) 1 A g⁻¹.

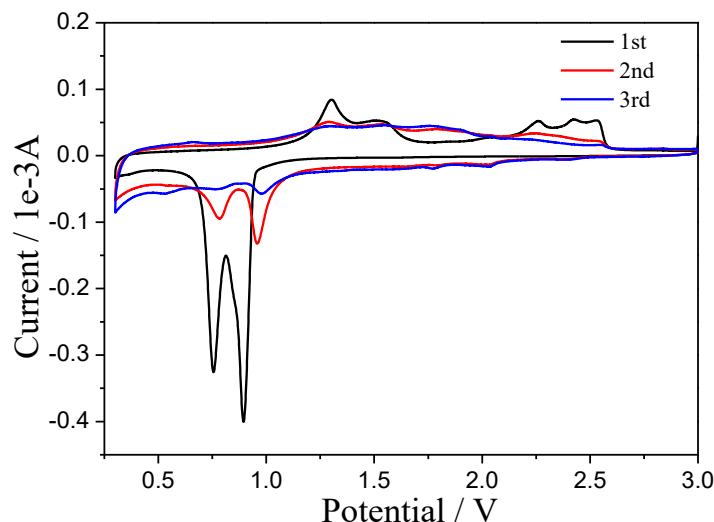


Figure 3.6 Typical CV curves of MoS₂-MS-800-based anode for the first three cycles at a scanning rate of 0.1 mV s⁻¹ in the voltage range of 0.3–3 V.

Figure 3.5a shows typical galvanostatic charging/discharging profiles for the 1st, 2nd, 5th and 10th cycles at a current density of 100 mA g⁻¹ in the voltage range of 0.3-3 V for MoS₂-MS and MoS₂-MS-800-based anodes. One can see that the discharge and charge capacities of 498 and 438 mA h g⁻¹ were delivered respectively with a Coulombic efficiency up to 88.04% in the 1st cycle in the case of MoS₂-MS-based anode for the SIBs. Herein, the initial Coulombic efficiency belongs to a high value for the metal sulfide as the anode for SIBs. The reason of high initial Coulombic efficiency is that the SEI layer formed by ether-based electrolyte was stable and thin, which is benefit for Na⁺ transport[40]. In contrast, for the MoS₂-MS-800, the initial discharge and charge capacities were only 193.5 and 174.2 mA h g⁻¹, respectively, indicating that the

large interlayer spacing of MoS₂-MS should play an important role in the capacity of MoS₂ as the anode material.

To investigate electrochemical reactions occurred in the charging/discharging process, the cycle voltammograms (CVs) of MoS₂-MS and MoS₂-MS-800-based anodes were collected at a scanning rate of 0.1 mV s⁻¹ in the voltage range of 0.3-3 V (Figures 3.5b and 3.6). As shown in Figure 3.5b, three cathodic peaks at 1.6, 1.0, 0.3 V were observed during the first discharging process. Herein, the peaks at 1.6 and 1.0 V are assignable to the intercalation of Na⁺ ions into the interlayers with the formation of Na_xMoS₂, which can be described as the equation of $\text{MoS}_2 + x\text{Na} \rightarrow \text{Na}_x\text{MoS}_2$ [19, 41]. In the subsequent cycles (i.e., 2nd and 3rd cycles), one can see that the sharp cathodic peak intensity at 0.3 V gradually decreased, indicating that the solid electrolyte interphase (SEI) layer was gradually forming during the discharging/charging process. Remarkably, a broad oxidation peak appeared in the range of 1.5-2.5 V in the first charging process, indicating the deintercalation of Na⁺ ions from MoS₂-MS. Furthermore, it should be noted that the CV curves during the discharging/charging cycles maintained the similar shape, indicating the good cycling stability of MoS₂-MS.

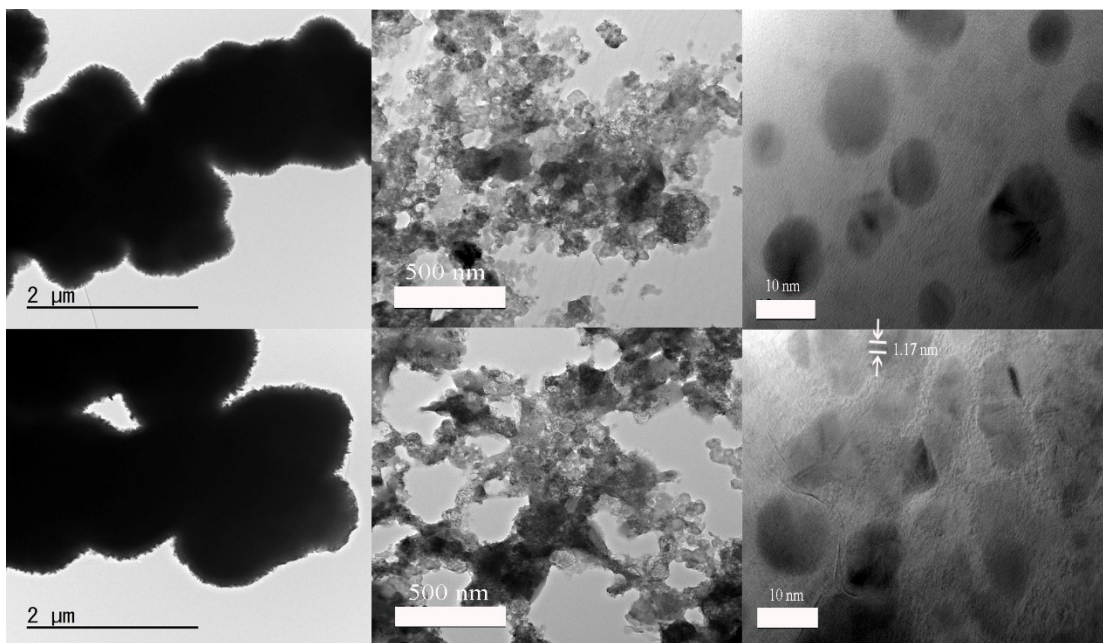


Figure 3.7 TEM images of (a) MoS₂-MS and (d) MoS₂-MS-800 before cycling; TEM and HRTEM images of (b, c) MoS₂-MS and (e, f) MoS₂-MS-800 after 500 cycles at the current density of 1 A g⁻¹.

Figure 3.5c shows the cycling stability of MoS₂-MS as the anode for SIBs at a current density of 100 mA g⁻¹. It is obvious that the specific capacity maintained at 467 mAh g⁻¹ with a Coulombic efficiency of ~100% after 100 cycles, revealing the good stability of MoS₂-MS electrode. Furthermore, as shown in Figure 3.5d, at a larger current density of 1 A g⁻¹, the cycling stability of MoS₂-MS anode with a specific capacity of 412 mAh g⁻¹ and a Coulombic efficiency of ~100% was maintained until 500 cycles. In contrast, for the MoS₂-MS-800, the specific discharging capacity was much lower than those of MoS₂-MS in the first several cycles at the current density of 100 mA g⁻¹ (Figure 3.5c), but increased gradually during the following discharging/charging cycles, and finally exceeded that of MoS₂-MS after the 78th cycle. Similarly, this phenomenon was observed at the current density of 1 A g⁻¹ (Figure 3.5d)

for the MoS₂-MS-800-based anode. It is possible that the interlayer spacing of MoS₂-MS-800 could be gradually enlarged during the discharging/charging cycling. Figure 3.7 e and f shows the morphology of MoS₂-MS-800 after 500-cycle test at a current density of 1 mA g⁻¹. It is clearly seen that the size of MoS₂-MS-800 almost decreased to 10 nm, indicating the pulverization of the MoS₂-MS-800 material during the discharging/charging process. Furthermore, the 002 plane almost disappeared with the charge/discharge process, and large interlayer spacing of 1.17 nm was observed, which is larger than that of the initial MoS₂-MS-800 (0.615 nm).

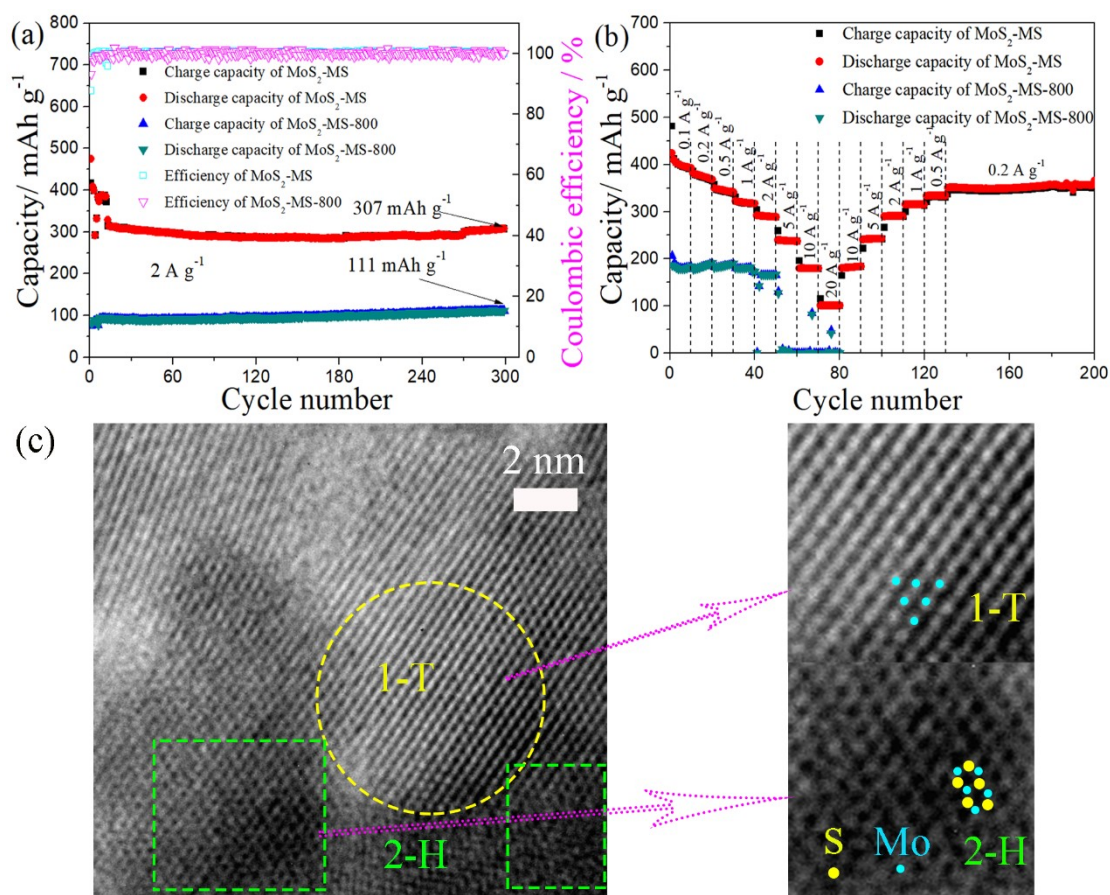


Figure 3.8 (a) Cycling performances of the MoS₂-MS and MoS₂-MS-800-based anodes at a current rate of 2 A g⁻¹; (b) Rate performances of MoS₂-MS and MoS₂-MS-800-

based anodes. HRTEM images of (c) MoS₂-MS after 500 cycles at the current density of 1 A g⁻¹.

Figure 3.8a shows cycling performances of the MoS₂-MS and MoS₂-MS-800-based anodes at a current rate of 2 A g⁻¹. One can see that MoS₂-MS-based anode delivered a stable capacity of 307 mAh g⁻¹ after 300 cycles, indicating good stability at a larger current density. In contrast, for the MoS₂-MS-800-based anode, only a specific capacity of 111 mAh g⁻¹ was achieved after the 300th cycle. Figure 3.8b shows rate performances of MoS₂-MS and MoS₂-MS-800-based anodes. One can see that the MoS₂-MS-based anode delivered well reversible specific capacities of 392, 368, 234, 317, 288, 237, and 179 mAh g⁻¹ at the current densities of 0.1, 0.2, 0.5, 1, 2, 5, 10 A g⁻¹, respectively. Furthermore, even at a very high current density of 20 A g⁻¹, a stable reversible capacity of 100 mAh g⁻¹ was achieved. Especially, it is worth noting that when the current density gradually returned back to 10, 5, 2, 1, 0.5, and 0.2 A g⁻¹, the reversible capacity also gradually recovered to 183, 242, 290, 315, 333, and 356 mAh g⁻¹, respectively. In contrast, the MoS₂-MS-800-based anode showed a low rate performance with the specific capacities of 182, 189, 189, 181, and 166 mAh g⁻¹ at the current densities of 0.1, 0.2, 0.5, 1, and 2 A g⁻¹, respectively. Especially, when the current density was increased to 5 A g⁻¹, the capacity decreased to 0 mAh g⁻¹. Thus, the MoS₂-MS should be a stable anode materials for SIBs with a high performance. To confirm the structure after cycling, the TEM and HRTEM after 500 cycles were measured as shown in Figure 3.7. From the Figure 3.7 a-c, it can be seen that the morphology of MoS₂-MS has changed from microspheres to nanospheres after 500

cycles. However, the 1T and 2H phases still could be observed as shown in Figure 3.8 c, indicating that the mixed phase can be maintained after cycling.

3.3.3 Electrochemical kinetics

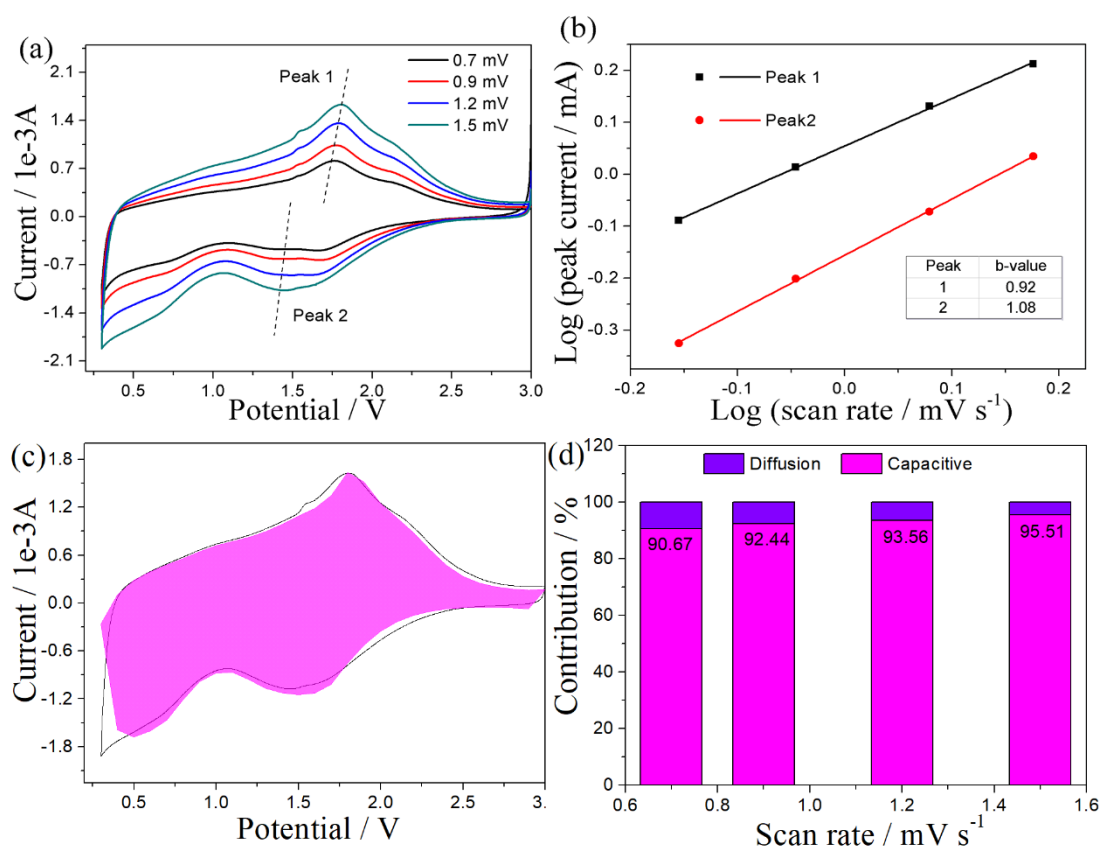


Figure 3.9 (a) CV curves of MoS₂-MS at different scan rates from 0.7 to 1.5 mV s⁻¹, (b) corresponding log *i* vs. log *v* plots of peaks 1, 2 and 3; (c) capacitive contribution of MoS₂-MS in comparison to the total current at 1.5 mV s⁻¹; (d) capacitive contribution of MoS₂-MS at different scan rate from 0.7 to 1.5 mV s⁻¹.

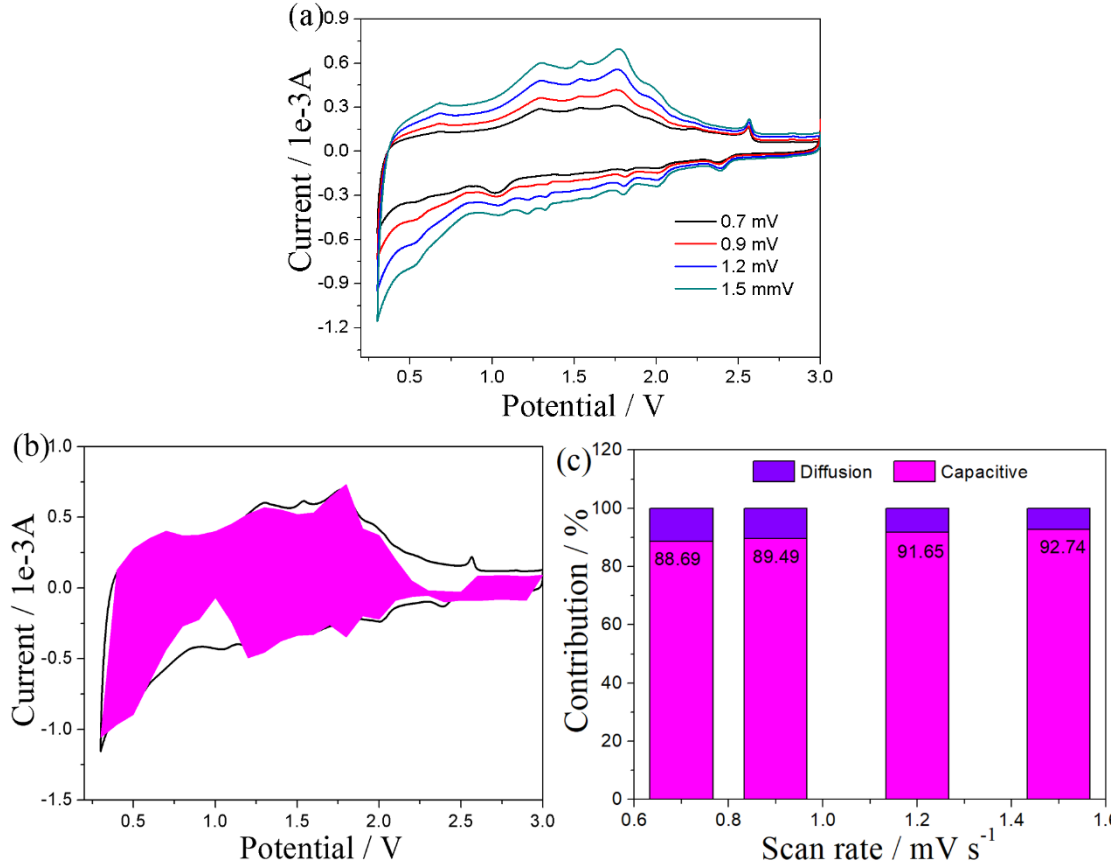


Figure 3.10 (a) CV curves of MoS₂-MS-800 at different scan rates from 0.7 to 1.5 mV s⁻¹, (b) capacitive contribution of MoS₂-MS-800 in comparison to the total current at 1.5 mV s⁻¹; (C) capacitive contribution of MoS₂-MS-800 at different scan rate from 0.7 to 1.5 mV s⁻¹.

Figure 3.9a shows CV curves of MoS₂-MS-based anode at different scan rates from 0.7 to 1.5 mV s⁻¹. In general, the diffusion-controlled process and the pseudocapacitive controlled by surface process will affect the charge storage ability of anode materials [20, 42, 43]. To gain the information of capacitive effect of the battery system, the following equation is generally used for the calculation:

$$i = av^b \quad \text{Eq. (1)}$$

where i and v are the current density and the scan rate, respectively; a and b are adjustable constants. The storage mechanism depends on the b -value, whose value is in a range from 0.5 to 1. If the b -value approaches 0.5, which means that ion diffusion plays a major role in the system. In contrast, the b -value is close to 1, indicating a surface-controlled process. According to the equation (2), the b -values of 0.92 and 1.08 were obtained as shown in Figure 3.9b, corresponding to the peaks 1 and 2 (in Figure 3.9a), respectively, indicating a surface-controlled process, which is benefit for the rate performance. Furthermore, the pseudocapacitive contribution can be quantified by following equation[44]:

$$i = k_1v + k_2v^{1/2} \quad \text{Eq. (2)}$$

where i and v are the current value at different voltages and the scan rate, respectively; k_1v and $k_2v^{1/2}$ correspond to the contribution of capacitive and diffusion. Figure 3.9c displays the comparison of the current of capacitive (pink line) with the total current at the scan rate of 1.5 mV s^{-1} . The capacitive contribution of $\sim 95.51\%$ was achieved for $\text{MoS}_2\text{-MS}$ -based anode, which is higher than that of $\text{MoS}_2\text{-MS-800}$ -based anode (Figure 3.10a). In addition, the contribution of capacitive at different scan rates was further calculated. As shown in Figure 3.9d. $\text{MoS}_2\text{-MS}$ -based anode delivered the capacitive contribution ratios of 90.67, 92.44, 93.56, and 95.51 % at the scan rates of 0.7, 0.9, 1.2, and 1.5 mV s^{-1} , respectively. In contrast, for $\text{MoS}_2\text{-MS-800}$ -based anode, the capacitive contribution ratios were only 88.69, 89.49, 91.65, and 92.74 % at the different scan rates of 0.7, 0.9, 1.2, and 1.5 mV s^{-1} , respectively (Figure 3.10c). Thus, the capacitive contribution of $\text{MoS}_2\text{-MS}$ -based was higher than that of $\text{MoS}_2\text{-MS-800}$ -

based anode, indicating a favorable charge transfer kinetics, which is attributed the disordered structure with more defects.

3.3.4 EIS analysis

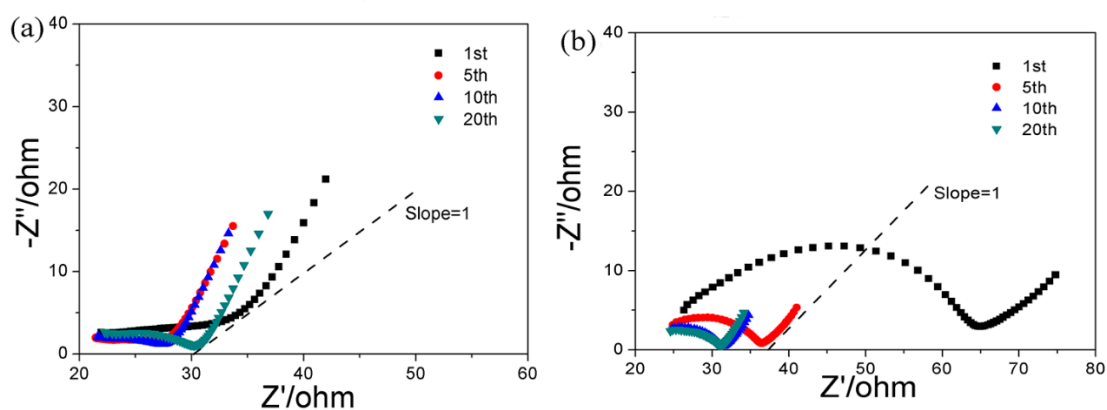


Figure 3.11 Nyquist plots of the (a) MoS₂-MS-based and (b) MoS₂-MS-800-based anodes.

Figures 3.11a and b show the Nyquist plots related to the MoS₂-MS and MoS₂-MS-800-based anodes after different cycles, respectively, in which a semicircle in the high frequency region and a slope line in the low frequency region correspond to the charge-transfer process and the Warburg process during the Na⁺ ion diffusion, respectively[45, 46]. Compared with the impedance spectra of MoS₂-MS-800-based anode (Figure 3.11b), it is obvious that the diameter of semicircle at the high-frequency for the MoS₂-MS-based anode (Figure 3.11a) was smaller, indicating its lower charge-transfer resistance. This can be attributed to the 1-T phase existed in disordered structure of MoS₂-MS[47, 48]. Meanwhile, the slope of line at the low-frequency related to the MoS₂-MS-based anode was steeper than that of MoS₂-MS-800-based one, also indicating that the MoS₂-MS-based anode possessed a lower diffusion resistance

due to the larger interlayer spacing and more defects, which facilitated the intercalation of Na^+ . As stated above, the large interlayer spacing and more defects should be favorable for the rapid diffusion of Na^+ ions while the 1-T phase could enhance the electrical conductivity. As a result, the MoS_2 -MS-based anode exhibited more excellent rate performance.

3.4 Conclusions

In summary, the MoS_2 -MS anode material with 1T/2H phase was successfully synthesized by a one-step hydrothermal method. The obtained MoS_2 -MS was confirmed to have disordered structure, rich defects and large interlayer spacing. As it was used as the anode material for SIBs, the MoS_2 -MS-based anode displayed a highly stable specific capacity of 467 mAh g^{-1} over 100 cycles at 100 mA g^{-1} , good cycling stability with a specific capacity of 412 mAh g^{-1} over 500 cycles at 1 A g^{-1} , and superb rate performance with a specific capacity of 100 mAh g^{-1} maintaining at 20 A g^{-1} . Such an excellent electrochemical performance was considered to be ascribed to its specific structure. Especially, the 1-T phase presented in the disordered structure enhanced the electrical conductivity, the rich defects provided more active sites for Na^+ ion storage and the large interlayer spacing facilitated the diffusion of the Na^+ ions. This work might provide a strategy to increase the electrochemical performance and decrease the cost for developing electrode materials in energy storage field.

References

- [1] W. Luo, F. Shen, C. Bommier, H. Zhu, X. Ji, L. Hu, Na-Ion Battery Anodes: Materials and Electrochemistry, *Acc. Chem. Res.* 49 (2016) 231-240.
- [2] H. Pan, Y.-S. Hu, L. Chen, Room-temperature stationary sodium-ion batteries for large-scale electric energy storage, *Energy Environ. Sci.* 6 (2013) 2338.
- [3] D. Kundu, E. Talaie, V. Duffort, L.F. Nazar, The emerging chemistry of sodium ion batteries for electrochemical energy storage, *Angew. Chem. Int. Ed. Engl.* 54 (2015) 3431-3448.
- [4] N. Ortiz-Vitoriano, N.E. Drewett, E. Gonzalo, T. Rojo, High performance manganese-based layered oxide cathodes: overcoming the challenges of sodium ion batteries, *Energy Environ. Sci.* 10 (2017) 1051-1074.
- [5] X. Hu, W. Zhang, X. Liu, Y. Mei, Y. Huang, Nanostructured Mo-based electrode materials for electrochemical energy storage, *Chemical Society reviews* 44 (2015) 2376-2404.
- [6] J.Y. Hwang, S.T. Myung, Y.K. Sun, Sodium-ion batteries: present and future, *Chem. Soc. Rev.* 46 (2017) 3529-3614.
- [7] L. Jing, G. Lian, F. Niu, J. Yang, Q. Wang, D. Cui, C.-P. Wong, X. Liu, Few-atomic-layered hollow nanospheres constructed from alternate intercalation of carbon and MoS₂ monolayers for sodium and lithium storage, *Nano Energy* 51 (2018) 546-555.
- [8] D. Yu, Q. Pang, Y. Gao, Y. Wei, C. Wang, G. Chen, F. Du, Hierarchical flower-like VS₂ nanosheets – A high rate-capacity and stable anode material for sodium-ion battery, *Energy Storage Mater.* 11 (2018) 1-7.

- [9] Y. Liu, X.-Y. Yu, Y. Fang, X. Zhu, J. Bao, X. Zhou, X.W.D. Lou, Confining SnS₂ ultrathin nanosheets in hollow carbon nanostructures for efficient capacitive sodium storage, *Joule* 2 (2018) 725-735.
- [10] Y. Wang, D. Kong, S. Huang, Y. Shi, M. Ding, Y. Von Lim, T. Xu, F. Chen, X. Li, H.Y. Yang, 3D carbon foam-supported WS₂ nanosheets for cable-shaped flexible sodium ion batteries, *J. Mater. Chem. A* 6 (2018) 10813-10824.
- [11] T. Wang, S. Chen, H. Pang, H. Xue, Y. Yu, MoS₂-Based Nanocomposites for Electrochemical Energy Storage, *Adv Sci (Weinh)* 4 (2017) 1600289.
- [12] Y. Xiao, S.H. Lee, Y.-K. Sun, The Application of Metal Sulfides in Sodium Ion Batteries, *Adv. Energy Mater.* 7 (2017) 1601329.
- [13] S.H. Choi, Y.N. Ko, J.-K. Lee, Y.C. Kang, 3D MoS₂-Graphene Microspheres Consisting of Multiple Nanospheres with Superior Sodium Ion Storage Properties, *Adv. Funct. Mater.* 25 (2015) 1780-1788.
- [14] X. Xu, R. Zhao, W. Ai, B. Chen, H. Du, L. Wu, H. Zhang, W. Huang, T. Yu, Controllable Design of MoS₂ Nanosheets Anchored on Nitrogen-Doped Graphene: Toward Fast Sodium Storage by Tunable Pseudocapacitance, *Adv. Mater.* 30 (2018) e1800658.
- [15] Z. Hu, Q. Liu, S.L. Chou, S.X. Dou, Advances and Challenges in Metal Sulfides/Selenides for Next-Generation Rechargeable Sodium-Ion Batteries, *Adv. Mater.* 29 (2017).
- [16] X. Zhao, G. Wang, X. Liu, X. Zheng, H. Wang, Ultrathin MoS₂ with expanded interlayers supported on hierarchical polypyrrole-derived amorphous N-doped carbon

- tubular structures for high-performance Li/Na-ion batteries, *Nano Research* 11 (2018) 3603-3618.
- [17] K. Yao, Z. Xu, Z. Li, X. Liu, X. Shen, L. Cao, J. Huang, Synthesis of Grain-like MoS₂ for High-Performance Sodium-Ion Batteries, *ChemSusChem* 11 (2018) 2130-2137.
- [18] Y. Li, Y. Liang, F.C. Robles Hernandez, H. Deog Yoo, Q. An, Y. Yao, Enhancing sodium-ion battery performance with interlayer-expanded MoS₂-PEO nanocomposites, *Nano Energy* 15 (2015) 453-461.
- [19] Z. Hu, L. Wang, K. Zhang, J. Wang, F. Cheng, Z. Tao, J. Chen, MoS₂ nanoflowers with expanded interlayers as high-performance anodes for sodium-ion batteries, *Angew. Chem. Int. Ed. Engl.* 53 (2014) 12794-12798.
- [20] Z. Zhang, S. Wu, J. Cheng, W. Zhang, MoS₂ nanobelts with (002) plane edges-enriched flat surfaces for high-rate sodium and lithium storage, *Energy Storage Mater.* 15 (2018) 65-74.
- [21] K. Yao, Z. Xu, J. Huang, M. Ma, L. Fu, X. Shen, J. Li, M. Fu, Bundled Defect-Rich MoS₂ for a High-Rate and Long-Life Sodium-Ion Battery: Achieving 3D Diffusion of Sodium Ion by Vacancies to Improve Kinetics, *Small* 15 (2019) e1805405.
- [22] M. Wang, G. Li, H. Xu, Y. Qian, J. Yang, Enhanced lithium storage performances of hierarchical hollow MoS₂ nanoparticles assembled from nanosheets, *ACS Appl. Mater. Interfaces* 5 (2013) 1003-1008.

- [23] X. Hu, Y. Li, G. Zeng, J. Jia, H. Zhan, Z. Wen, Three-Dimensional Network Architecture with Hybrid Nanocarbon Composites Supporting Few-Layer MoS₂ for Lithium and Sodium Storage, *ACS Nano* 12 (2018) 1592-1602.
- [24] P. Li, J.Y. Jeong, B. Jin, K. Zhang, J.H. Park, Vertically Oriented MoS₂ with Spatially Controlled Geometry on Nitrogenous Graphene Sheets for High-Performance Sodium-Ion Batteries, *Adv. Energy Mater.* 8 (2018) 1703300.
- [25] J. Li, W. Qin, J. Xie, R. Lin, Z. Wang, L. Pan, W. Mai, Rational design of MoS₂-reduced graphene oxide sponges as free-standing anodes for sodium-ion batteries, *Chem. Eng. J.* 332 (2018) 260-266.
- [26] B. Lu, J. Liu, R. Hu, H. Wang, J. Liu, M. Zhu, C@MoS₂@PPy sandwich-like nanotube arrays as an ultrastable and high-rate flexible anode for Li/Na-ion batteries, *Energy Storage Mater.* 14 (2018) 118-128.
- [27] H. Zhu, F. Zhang, J. Li, Y. Tang, Penne-Like MoS₂ /Carbon Nanocomposite as Anode for Sodium-Ion-Based Dual-Ion Battery, *Small* 14 (2018) e1703951.
- [28] Y. Lu, Q. Zhao, N. Zhang, K. Lei, F. Li, J. Chen, Facile Spraying Synthesis and High-Performance Sodium Storage of Mesoporous MoS₂/C Microspheres, *Adv. Funct. Mater.* 26 (2016) 911-918.
- [29] A. Zak, Y. Feldman, V. Lyakhovitskaya, G. Leitus, R. Popovitz-Biro, E. Wachtel, H. Cohen, S. Reich, R. Tenne, Alkali metal intercalated fullerene-like MS₂ (M= W, Mo) nanoparticles and their properties, *J. Am. Chem. Soc.* 124 (2002) 4747-4758.
- [30] K. Chang, W. Chen, L. Ma, H. Li, H. Li, F. Huang, Z. Xu, Q. Zhang, J.-Y. Lee, Graphene-like MoS₂/amorphous carbon composites with high capacity and excellent

stability as anode materials for lithium ion batteries, *Journal of Materials Chemistry* 21 (2011) 6251.

[31] X. Chen, Z. Wang, Y. Wei, X. Zhang, Q. Zhang, L. Gu, L. Zhang, N. Yang, R. Yu, High Phase-Purity 1T-MoS₂ Ultrathin Nanosheets by a Spatially Confined Template, *Angew. Chem. Int. Ed.* 58 (2019) 17621-17624.

[32] C. Xu, L. Jiang, X. Li, C. Li, C. Shao, P. Zuo, M. Liang, L. Qu, T. Cui, Miniaturized high-performance metallic 1T-Phase MoS₂ micro-supercapacitors fabricated by temporally shaped femtosecond pulses, *Nano Energy* 67 (2020) 104260.

[33] D. Sun, D. Huang, H. Wang, G.-L. Xu, X. Zhang, R. Zhang, Y. Tang, D. Abd Ei-Hady, W. Alshitari, A. Saad Al-Bogami, K. Amine, M. Shao, 1T MoS₂ nanosheets with extraordinary sodium storage properties via thermal-driven ion intercalation assisted exfoliation of bulky MoS₂, *Nano Energy* 61 (2019) 361-369.

[34] S. Zhang, B. Chowdari, Z. Wen, J. Jin, J. Yang, Constructing highly oriented configuration by few-layer MoS₂: toward high-performance lithium-ion batteries and hydrogen evolution reactions, *ACS Nano* 9 (2015) 12464-12472.

[35] X. Geng, W. Sun, W. Wu, B. Chen, A. Al-Hilo, M. Benamara, H. Zhu, F. Watanabe, J. Cui, T.P. Chen, Pure and stable metallic phase molybdenum disulfide nanosheets for hydrogen evolution reaction, *Nat. Commun.* 7 (2016) 10672.

[36] D.R. A Trends Guide Cummins, U. Martinez, A. Sherehiy, R. Kappera, A. Martinez-Garcia, R.K. Schulze, J. Jasinski, J. Zhang, R.K. Gupta, J. Lou, M. Chhowalla, G. Sumanasekera, A.D. Mohite, M.K. Sunkara, G. Gupta, Efficient hydrogen evolution

- in transition metal dichalcogenides via a simple one-step hydrazine reaction, *Nat. Commun.* 7 (2016) 11857.
- [37] J. Wang, C. Luo, T. Gao, A. Langrock, A.C. Mignerey, C. Wang, An advanced MoS₂/carbon anode for high-performance sodium-ion batteries, *Small* 11 (2015) 473-481.
- [38] X. Fan, P. Xu, D. Zhou, Y. Sun, Y.C. Li, M.A. Nguyen, M. Terrones, T.E. Mallouk, Fast and Efficient Preparation of Exfoliated 2H MoS₂ Nanosheets by Sonication-Assisted Lithium Intercalation and Infrared Laser-Induced 1T to 2H Phase Reversion, *Nano Lett.* 15 (2015) 5956-5960.
- [39] Z. Li, A. Ottmann, T. Zhang, Q. Sun, H.-P. Meyer, Y. Vaynzof, J. Xiang, R. Klingeler, Preparation of hierarchical C@MoS₂@C sandwiched hollow spheres for lithium ion batteries, *J. Mater. Chem. A* 5 (2017) 3987-3994.
- [40] K. Li, J. Zhang, D. Lin, D.W. Wang, B. Li, W. Lv, S. Sun, Y.B. He, F. Kang, Q.H. Yang, L. Zhou, T.Y. Zhang, Evolution of the electrochemical interface in sodium ion batteries with ether electrolytes, *Nat. Commun.* 10 (2019) 725.
- [41] Z.-H. Zhao, X.-D. Hu, H. Wang, M.-Y. Ye, Z.-Y. Sang, H.-M. Ji, X.-L. Li, Y. Dai, Superelastic 3D few-layer MoS₂/carbon framework heterogeneous electrodes for highly reversible sodium-ion batteries, *Nano Energy* 48 (2018) 526-535.
- [42] T. Brezesinski, J. Wang, S.H. Tolbert, B. Dunn, Ordered mesoporous alpha-MoO₃ with iso-oriented nanocrystalline walls for thin-film pseudocapacitors, *Nature materials* 9 (2010) 146-151.

- [43] D. Chao, C. Zhu, P. Yang, X. Xia, J. Liu, J. Wang, X. Fan, S.V. Savilov, J. Lin, H.J. Fan, Z.X. Shen, Array of nanosheets render ultrafast and high-capacity Na-ion storage by tunable pseudocapacitance, *Nat. Commun.* 7 (2016) 12122.
- [44] F. Zheng, W. Zhong, Q. Deng, Q. Pan, X. Ou, Y. Liu, X. Xiong, C. Yang, Y. Chen, M. Liu, Three-dimensional (3D) flower-like MoSe₂/N-doped carbon composite as a long-life and high-rate anode material for sodium-ion batteries, *Chem. Eng. J.* 357 (2019) 226-236.
- [45] Y. Zhang, S. Yu, H. Wang, Z. Zhu, Q. Liu, E. Xu, D. Li, G. Tong, Y. Jiang, A novel carbon-decorated hollow flower-like MoS₂ nanostructure wrapped with RGO for enhanced sodium-ion storage, *Chem. Eng. J.* 343 (2018) 180-188.
- [46] T.T. Shan, S. Xin, Y. You, H.P. Cong, S.H. Yu, A. Manthiram, Combining Nitrogen-Doped Graphene Sheets and MoS₂: A Unique Film–Foam–Film Structure for Enhanced Lithium Storage, *Angew. Chem. Int. Ed.* 55 (2016) 12783-12788.
- [47] W. Tang, X. Wang, D. Xie, X. Xia, C. Gu, J. Tu, Hollow metallic 1T MoS₂ arrays grown on carbon cloth: a freestanding electrode for sodium ion batteries, *J. Mater. Chem. A* 6 (2018) 18318-18324.
- [48] J. Wu, J. Liu, J. Cui, S. Yao, M. Ihsan-Ul-Haq, N. Mubarak, E. Quattrocchi, F. Ciucci, J.-K. Kim, Dual-phase MoS₂ as a high-performance sodium-ion battery anode, *J. Mater. Chem. A* 8 (2020) 2114-2122.

CHAPTER 4 A novel vanadium-mediated MoS₂ with metallic behavior for sodium ion batteries: achieving fast Na⁺ diffusion to enhance electrochemical kinetics

4.1 Introduction

With the rapid developments and applications of electronic devices, electric vehicles and renewable energy, lithium ion battery (LIB) cannot meet the ever-increasing demand due to the limited lithium resource [1, 2]. As such, it is essential to find potential substitute materials of LIBs. Sodium ion battery (SIB) is one of choices since it has the similar electrochemical performance as the LIB but there are abundant sodium resources on the earth [3-5]. However, since the radius of Na⁺ (1.02 Å) is much larger than that of Li⁺ (0.76 Å) [1, 6, 7], the sluggish reaction kinetics and large volume expansion in the anode still hinder the application of the SIBs. Moreover, the large Na⁺ radius also easily causes the electrode pulverized during the charging/discharging process, which always leads to the bad cyclic stability and poor rate performance. Thus, it is still full of challenge to find effective strategy to overcome these issues for the anode in order to promote the commercialization of SIBs.

Recently, two-dimensional transition metal dichalcogenides (2D TMDs) such as MoS₂ [8], VS₂ [9], SnS₂ [10] and WS₂ [11] have been considered as the promising anode candidates for SIBs since their weak interlayer van der Waals forces are benefit for the intercalation and deintercalation of Na⁺. Among these 2D TMDs, MoS₂ based anodes have been widely studied due to its large interlayer spacing and high theoretical

capacity (670 mAh g^{-1}) [12-16]. Nevertheless, pure MoS_2 based anode still faces the issues of poor electronic conductivity, sluggish electrochemical kinetics and large volume expansion during the intercalation/deintercalation of Na^+ [17-19]. Numerous efficient strategies have been attempted to solve the above-mentioned issues. Among them, nanostructure designing with the carbon modification is the main one for the generation of more active sites for Na^+ storage with the increase of conductivity as well as the hindrance of electrode pulverization [20-25]. Unfortunately, even though these strategies are very effective, the fabrication process is too complex. Therefore, it is necessary to find simpler synthesis process for the preparation of 2D TMDs.

Another 2D TMD of VS_2 was found to possess good electrochemical performance even without the combination with carbon-based materials [26, 27]. The theoretical study also indicated that VS_2 has a faster Li^+ diffusion rate than MoS_2 , which may be also applied for SIBs [28]. To combine the merits of MoS_2 and VS_2 , in the present work, VMoS_2 , a vanadium mediated molybdenum disulfide material, was synthesized by a facile one-step hydrothermal method and used as the anode material for the SIBs. The obtained VMoS_2 was characterized in details and the performance as the anode material was investigated. Meanwhile, the density functional theory (DFT) calculations were performed to understand the relationship between the modified structure and the electronic conductivity and further identify the electrochemical performance. It is expected to significantly increase the conductivity of MoS_2 and decrease diffusion barrier of Na^+ by the mediating of V species, thereby enhancing the electrochemical kinetics of Na^+ in the SIBs.

4.2 Experimental

4.2.1 Synthesis of VM-23, VM-33, VM-43, VM-53, MoS₂, A-MoS₂, and VS₂

VMoS₂ materials prepared with the different molar ratios of V:Mo in the precursors, i.e., 2:3, 3:3, 4:3, 5:3, namely VM-23, VM-33, VM-43 and VM-53, respectively, were synthesized by a facile one-step hydrothermal method. For example, for the synthesis of VM-43, firstly, 2.0 mmol of NH₄VO₃, 1.5 mmol of Na₂MoO₄•H₂O and 32 mmol of C₂H₅NS (TAA) were dissolved in 30 ml of distilled water with ultrasonic treatment at 45 °C for 60 min. Thereafter, the suspension was transferred to a 50 ml Teflon-lined sealed autoclave and heated at 220 °C for 24 h. The obtained product was collected by centrifugation and washed for several times successively using distilled water and ethanol, and finally dried at 60 °C in a vacuum oven for 12 h. For comparison, the pure MoS₂ was also synthesized using the same procedure but without the addition of NH₄VO₃, A-MoS₂ was synthesized in the presence of 2 ml of ammonia solution in the same hydrothermal process, and VS₂ was synthesized using the same procedure in presence of 2 ml of ammonia solution but without Na₂MoO₄•H₂O.

4.2.2 Characterizations

Morphology and elemental distribution analysis were carried out using a scanning electron microscope (SU8010, Hitachi, Japan) at an operation voltage of 15.0 kV with an energy dispersive spectrometer (EDS), and the nanostructure was observed using a high-resolution transmission electron microscope (TEM, JEM-2100F, JEOL, Japan) with an accelerating voltage of 200 kV. Crystalline structure was analyzed by an X-ray

diffractometer (XRD, Smartlab 9kW, Rigaku, Japan) with CuK α ($\lambda=1.5418 \text{ \AA}$) as the radiation source. The elemental compositions and chemical valence states were determined by an X-ray photoelectron spectrometer (XPS) (VG ESCALAB 250, Thermo Electron, UK) using an Al K α X-ray source (1486 eV). Raman spectra were collected with a Renishaw inVia Raman spectrometer using an excitation wavelength of 532 nm.

4.2.3 Electrochemical measurements

For fabricating the working electrode, 80 wt % of active material, 10 wt% of conductive carbon black and 10 wt% of sodium carboxymethylcellulose (CMC) were mixed in the deionized water to prepare a slurry at first. Then, the obtained slurry was pasted onto a copper foil and dried in a vacuum oven at 60 °C overnight. After that, the active material coated copper foil was cut into round pieces with a diameter of 12 mm as the electrode. Herein, the active material loading amount was $\sim 1.0 \text{ mg cm}^{-2}$. Sodium metal and glass fiber were used as the counter electrode and the separator, respectively. The electrolyte was 1 M sodium trifluoromethanesulfonate (NaSO₃CF₃) in diglyme (DGM). The cells were assembled in an argon-filled glove box. Charge/discharge measurements were carried out at various current densities over a voltage range of 0.3-3 V using a battery test system (LAND CT2001A model, Wuhan LAND Electronic. Ltd). Cyclic voltammographs (CVs) were recorded on an electrochemistry workstation at a scan rate of 0.1 mV s^{-1} . Electrochemical impedance spectra (EIS) were collected over a frequency range of 0.01 Hz-100 kHz.

4.2.4 Density functional theory (DFT) calculations

All DFT calculations were performed with the Cambridge Serial Total Energy Package (CASTEP) implemented in Materials Studio software using the pseudopotential method [29]. Electron-electron exchange and correlation energy was employed in the Perdew-Burke-Ernzerhof form of generalised gradient approximations (GGA) [30, 31]. The plane-wave cut-off was chosen to be 370 eV to ensure acceptable precision, and $3 \times 3 \times 2$ k-point grids were used in the calculation. The convergence criterion was within 1.0×10^{-5} eV per atom for the total energy, and internal stress was less than 0.05 GPa. The transition state search and confirmation were used to calculate the ion migration energy barrier.

4.3 Results and discussion

4.3.1 Characterizations

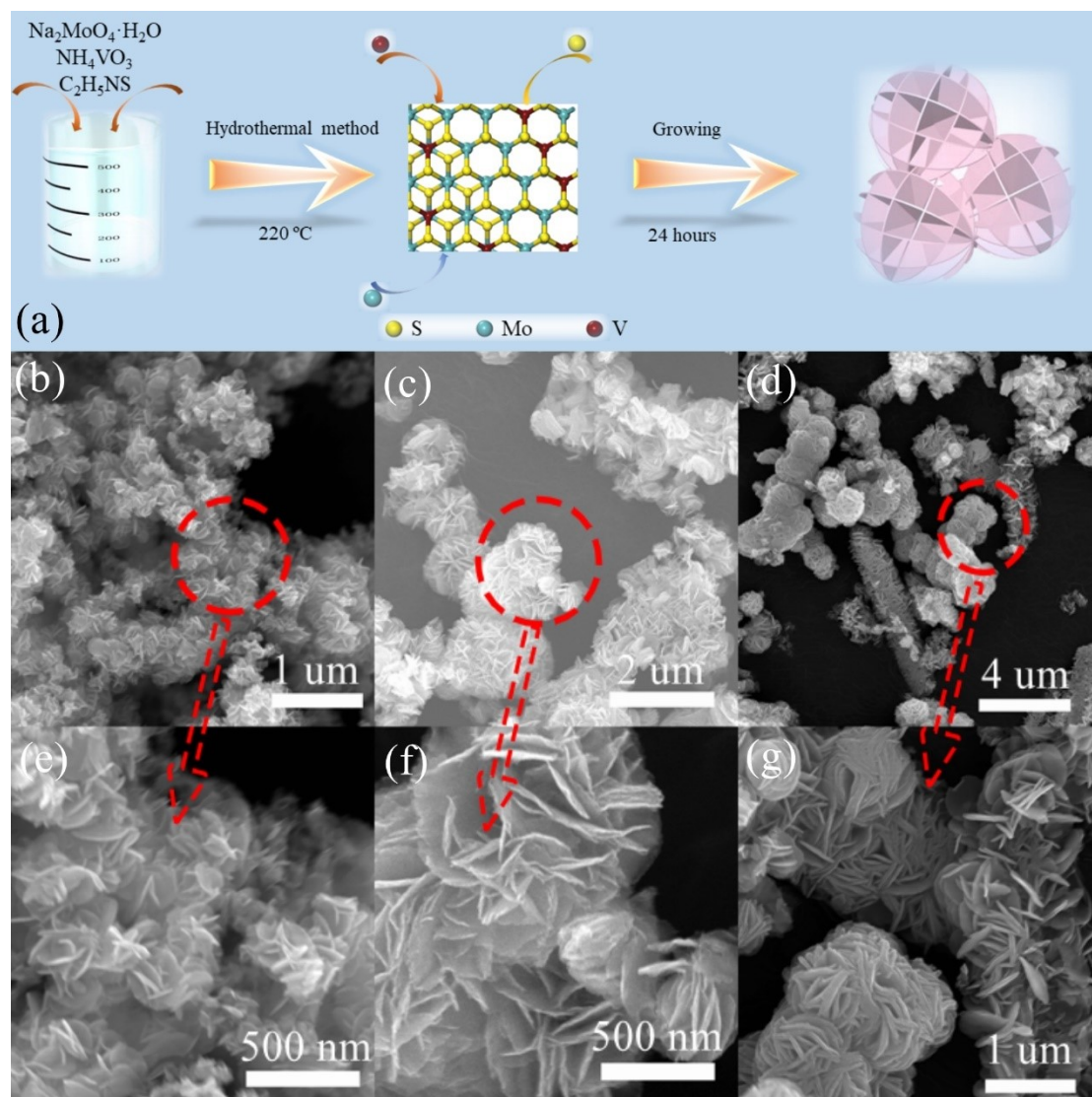


Figure 4.1 (a) Schematic illustration of the VMS₂ synthesis; FESEM images of the (b, e) VM-33, (c, f) VM-43, and (d, g) VM-53.

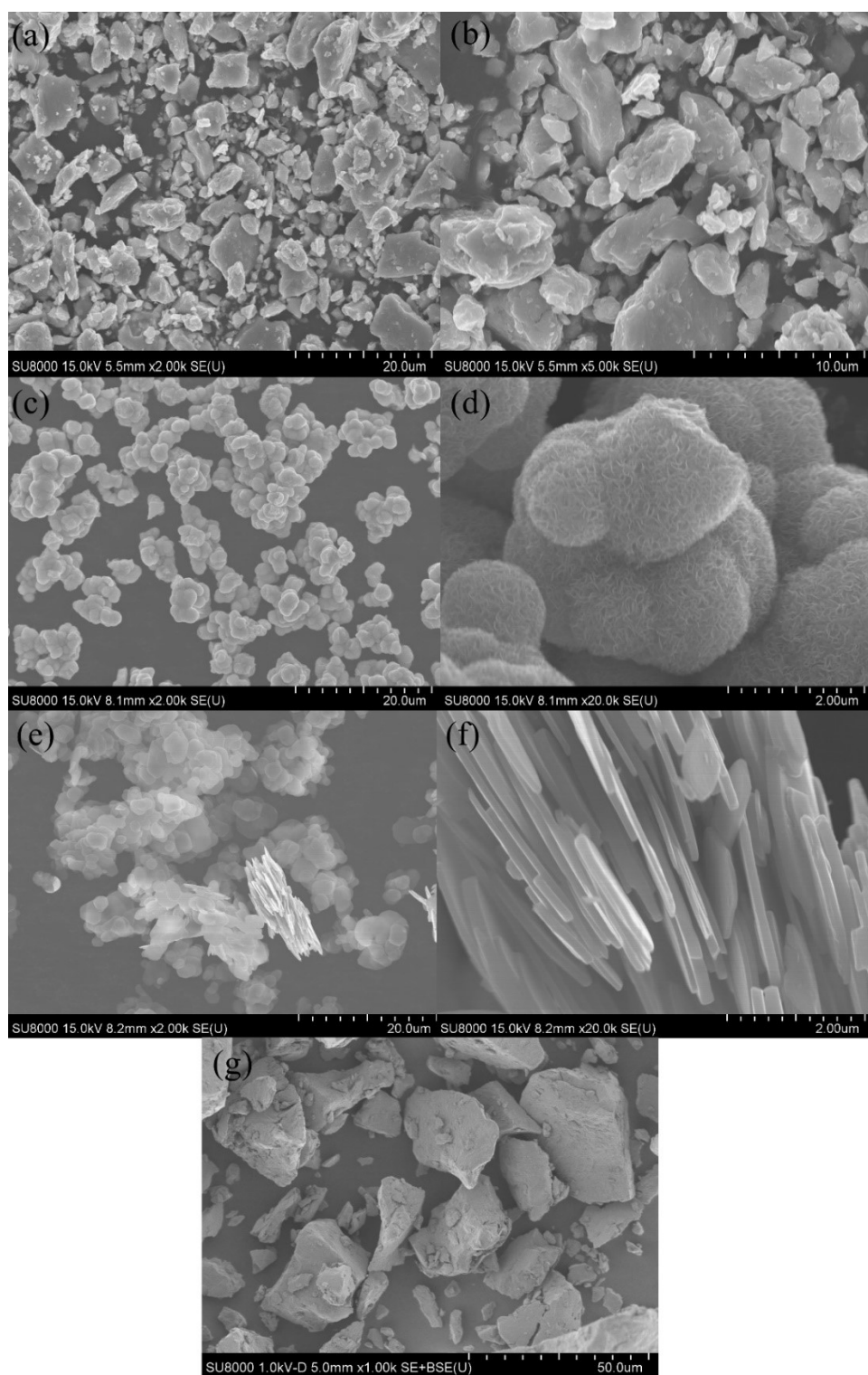


Figure 4.2 SEM morphologies of (a), (b) pure MoS₂; (c), (d) A-MoS₂; (e), (f) VS₂; and (g) VM-23.

Figure 4.1a schematically illustrates the formation of VMoS_2 material in the hydrothermal process. In order to explore the growth of flower-like morphology, a series of experiments were conducted. Firstly, pure MoS_2 was synthesized without the addition of NH_4VO_3 . The morphologies of pure MoS_2 are shown in Figures 3.2a and b, and the lumpy structure without any nanosheets were observed. Then, the precursors with different molar ratios of V:Mo were used to prepare the VMoS_2 materials. As shown in Figure 3.2g, VM-23 material still had a lumpy structure as the pure MoS_2 . Interestingly, with the increasing of NH_4VO_3 amount in the initial precursor, the flower-like morphology was gradually formed for VM-33, VM-43, and VM-53 as shown in Figure 4.1b-g, especially for VM-43 (Figure 4.1c). Close examination revealed that the nanosheets grew alternately to form flower-like morphology (Figure 4.1f). As a comparison, the morphology of VM-33 (Figure 4.1b and e) was similar as that of VM-43, but the particle size was smaller than that of VM-43. Notably, when the molar ratio of V:Mo was increased to 5:3, in addition to flower-like structure, the nanorod structure was also observed (Figure 4.1d and g). To prove that the formation of flower-like structure is not caused by NH_4^+ , A- MoS_2 was also synthesized in the presence of 2 ml of ammonia solution in the same hydrothermal process. The coral-like morphology with nanosheet structure was observed in Figures 4.2 c and d for A- MoS_2 . In addition, the VS_2 was also prepared using the same procedure in presence of 2 ml of ammonia solution but without $\text{Na}_2\text{MoO}_4 \cdot \text{H}_2\text{O}$. The flower-like morphology was not formed but the microsheet structure was observed for VS_2 (Figures 4.2 e and f). Herein, 2D TMD nuclei could be generated by the reactions of Mo and V species in the solution with S

species and then, the Mo and V species in the solution could continuously interact with the primary 2D nuclei from different directions, resulting in the further formation of nanosheets, which were intersected along different directions, resulting in the flower-like particle morphology during the hydrothermal process. The elemental analysis of VM-33, VM-43, and VM-53 were carried out using EDS (Figure 4.3). The atomic ratios of V to Mo were 1.42, 1.62, and 1.84 for VM-33, VM-43, and VM-53, respectively, which are summarized in Table 4.1.

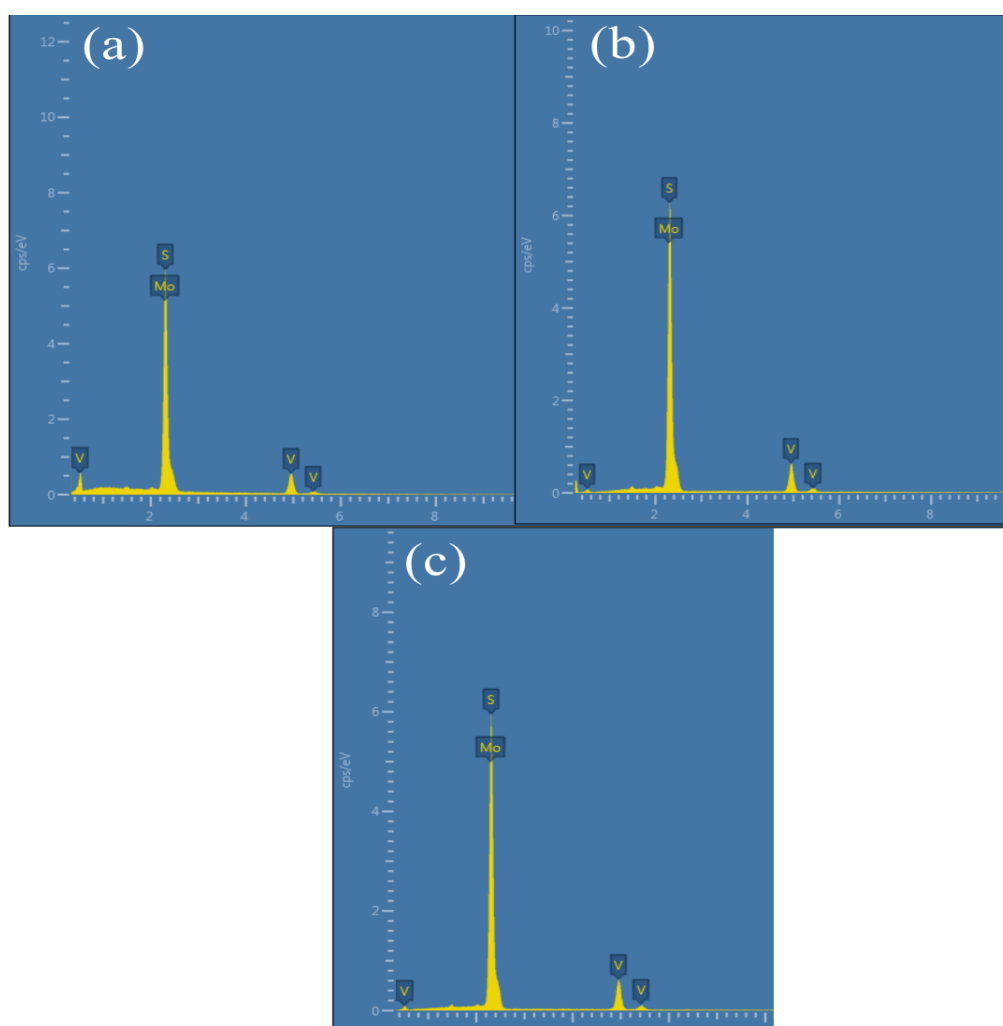


Figure 4.3 Elemental analysis of (a) VM-33, (b) VM-43, and (c) VM-53.

Table 4.1 Atomic contents in the VM-33, VM-43, and VM-53 based on elemental analysis.

Samples	S At%	Mo At%	V At%	V : Mo
VM-33	67.8	13.3	18.9	1.42
VM-43	68.3	12.1	19.6	1.62
VM-53	68.5	11.1	20.4	1.84

The nanostructure of VM-43 was further determined by TEM measurement. As shown in Figure 4.4, the flower-like morphology was also observed (Figure 4.4a and b), which is consistent with the SEM observation (Figure 4.1). From the HRTEM images of VM-43 (Figures 4.4d and e), it was worth noting that the interlayer spacing of ~ 0.60 nm was observed, which was smaller than that of 002 plane of MoS_2 (0.615 nm) [32] and larger than that of 001 plane of VS_2 (0.57 nm) [26]. The smaller interlayer spacing might be attributed to the V replacing Mo in the structure of MoS_2 . The inset HRTEM image in Figure 4.4e revealed that VM-43 had a disorder structure. Furthermore, the 1-T and 2-H phases with more defects were observed to be co-existed in nanostructure of VM-43 (Figure 4.4c and f). Figure 4.5 shows the TEM and HRTEM images of VM-33 and VM-53. One can see that the particle diameters of VM-33 and VM-53 were ~ 500 nm (smaller than that of VM-43, Figure 4.5a) and ~ 1500 nm (larger than that of VM-43, Figure 4.5c), respectively. In addition, the interlayer spacing of ~ 0.60 nm, 1-T and 1-H phases were observed for both of them (Figure 4.5b, c, e, and f), which is the same as that of VM-43. From energy disperse spectroscopic (EDS)

elemental mappings of VM-43 (Figure 4.4g-j), the Mo, V, and S elements were uniformly distributed on the VM-43, which also demonstrated that V elements were successfully combined in the nanostructure of MoS₂.

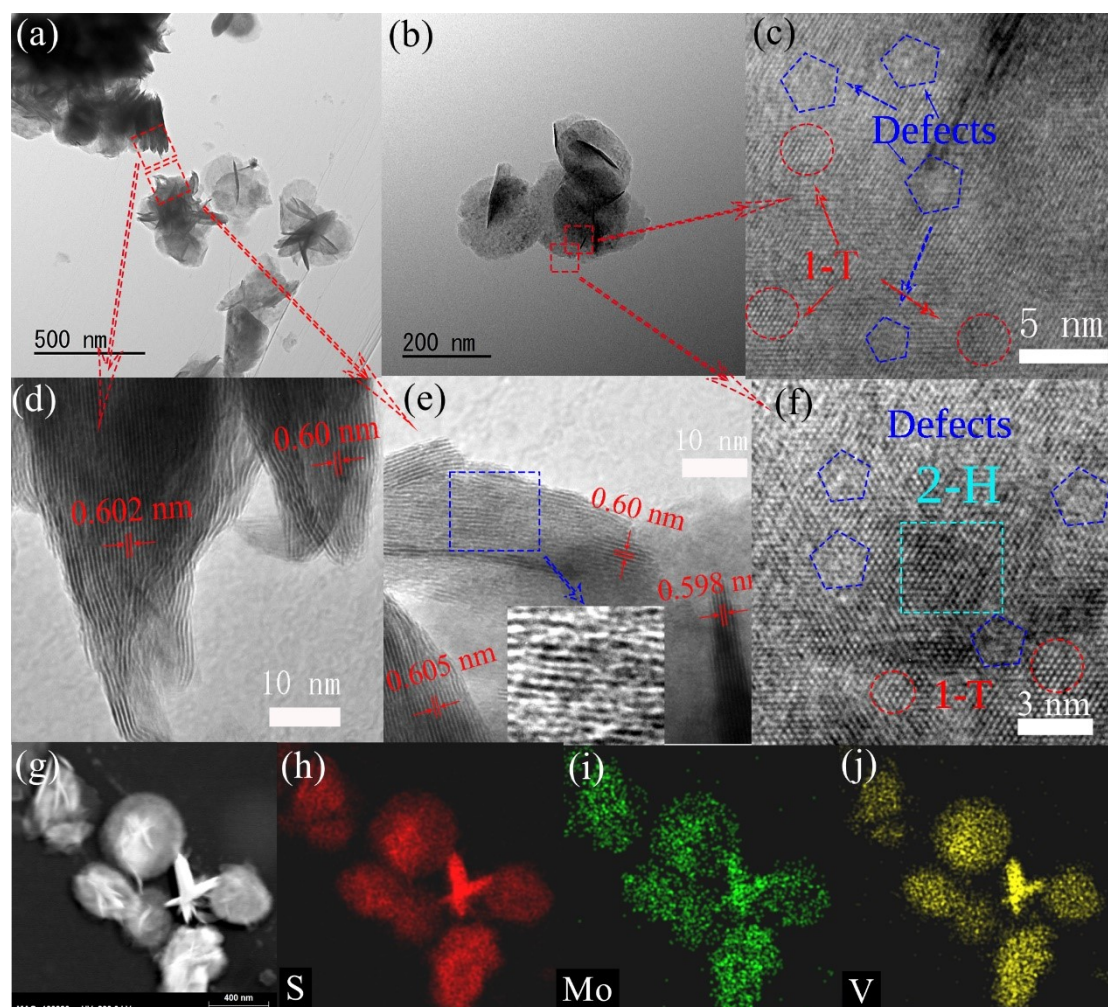


Figure 4.4 (a and b) TEM and (c-f) HRTEM images of VM-43 sample. (g) STEM elemental mappings of (h) S, (i) Mo and (j) V.

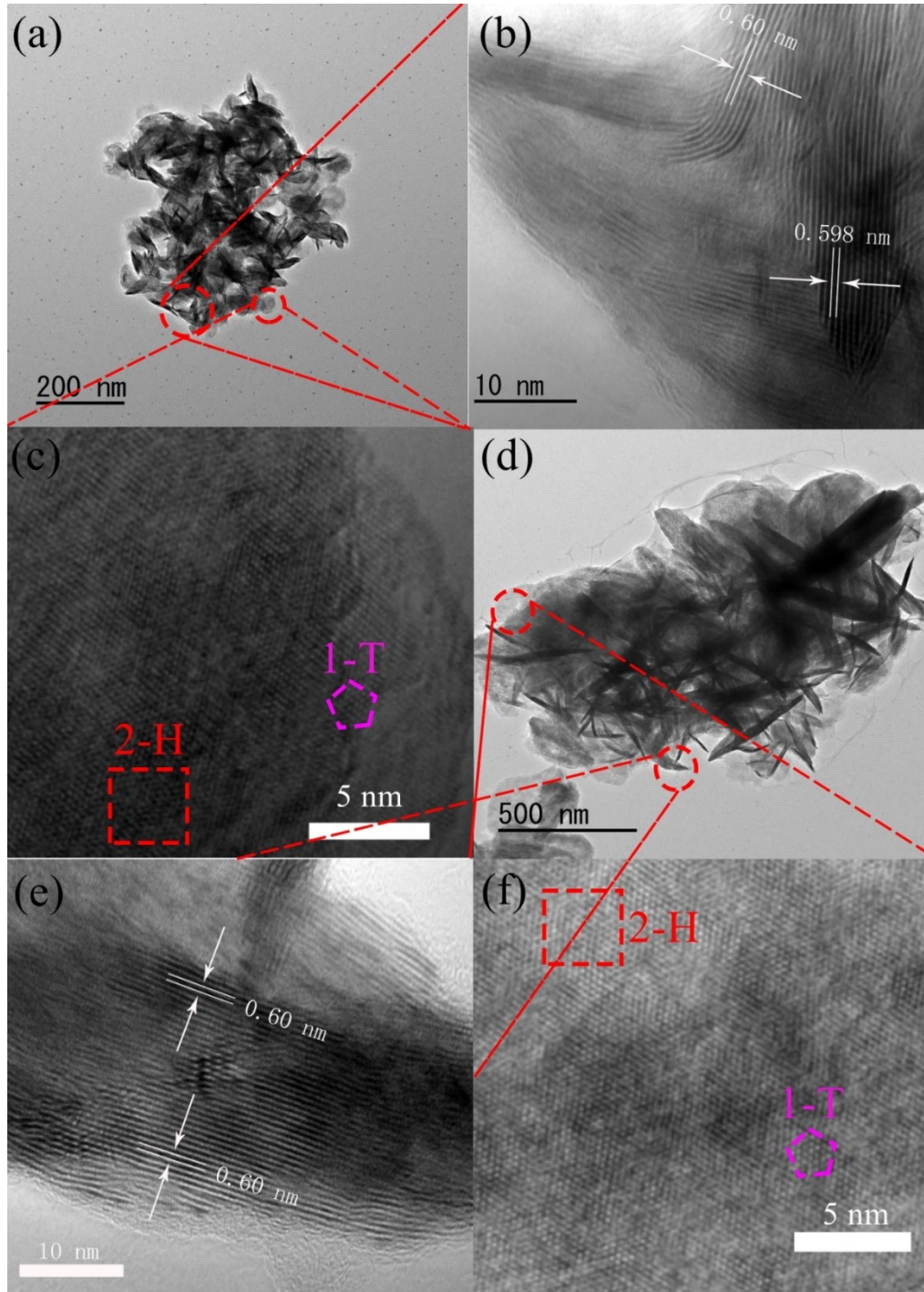


Figure 4.5 TEM images of (a) VM-33 and (d) VM-53; HRTEM images of (b), (c) VM-33 and (e), (f) VM-53.

In order to confirm the crystalline structure of sample, the X-ray diffraction (XRD) analysis was carried out. As shown in Figure 4.6a, four peaks located at $2\theta=14.72^\circ$,

$2\theta=33.46^\circ$, $2\theta=40.05^\circ$ and $2\theta=58.53^\circ$ were obviously observed, which corresponded to the (002), (100), (103) and (110) planes of 2H-MoS₂ (JCPDS No. 37-1492), respectively [33, 34]. According to Bragg's Law, the interlayer spacing of 002 plane of VM-43 was calculated to be 0.601 nm, which was also consistent with the HRTEM result (Figure 4.4d and e). It was worth noting that the intensity of 002 peak was gradually increased with the increasing of NH₄VO₃ amount in the initial precursor for the hydrothermal synthesis. However, in comparison, there were some broad peaks in Figure 4.7a and no any sharp peaks were observed for MoS₂ and A-MoS₂, indicating that VM-43 should be grown along the 002 plane in the existence of vanadium ions in the precursor. All peaks in the XRD pattern of VS₂ (Figure 4.7b) corresponded to the characteristic peaks of hexagonal VS₂ (JCPDS No. 89-1640). Interestingly, the characteristic peaks related to the vanadium disulfide were not found from the XRD patterns in the Figure 4.6a and Figure 4.7c, revealing that V⁴⁺ could be successfully combined into the framework of MoS₂, which was also in good agreement with the STEM elemental analysis (Figure 4.4g-j). Raman analysis of the as-prepared VM-43 was further employed to explore the structure. As shown in Figure 4.9, Raman peaks at ~ 290 , 388, and 410 cm⁻¹ were indexed to the E_{1g}, in-plane E_{2g}¹, and the out-of-plan A_{1g} modes of MoS₂ [35, 36], respectively. In addition, the peaks of 1-T phase were also observed, which were in good agreement with HRTEM results (Figure 4.4c and f). The intensity of J₁ peaks (Figure 4.9) was high, which was attributed to almost same position of 1-T phase peaks in Raman spectra of MoS₂ and VS₂ [36, 37]. However, the characteristic peak of VS₂ was not observed, which might be due to the locations

coincided with those of E_{1g} , E_{2g}^1 , and A_{1g} of MoS_2 . Meanwhile, the XRD patterns as well as the Raman spectra of VM-33 and VM-53 were similar as those of VM-43, indicating that VM-33 and VM-53 had the similar structure as the VM-43.

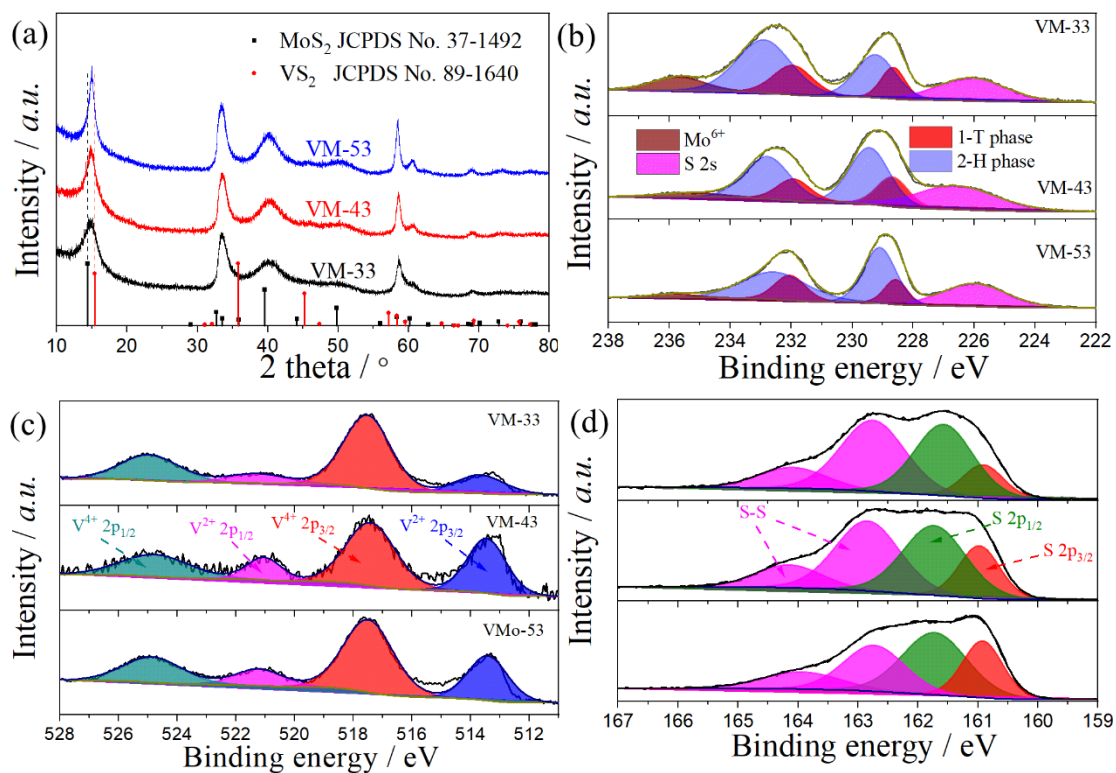


Figure 4.6 (a) XRD patterns of VM-33, VM-43 and VM-53. High-resolution XPS spectra of (b) Mo 3d, (c) V 2p and (d) S 2p.

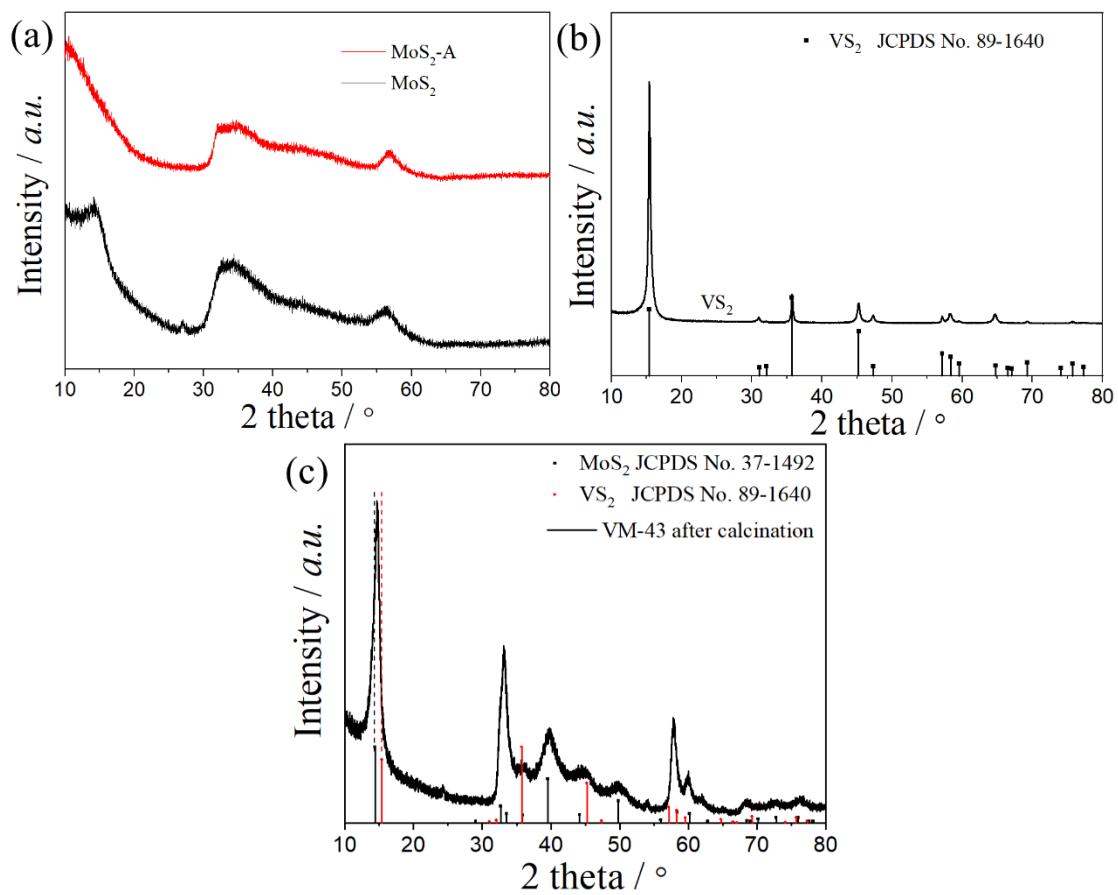


Figure 4.7 XRD patterns of (a) MoS₂, A-MoS₂, (b) VS₂, and (c) VM-43 after calcination at 800 °C for 2h in Argon gas.

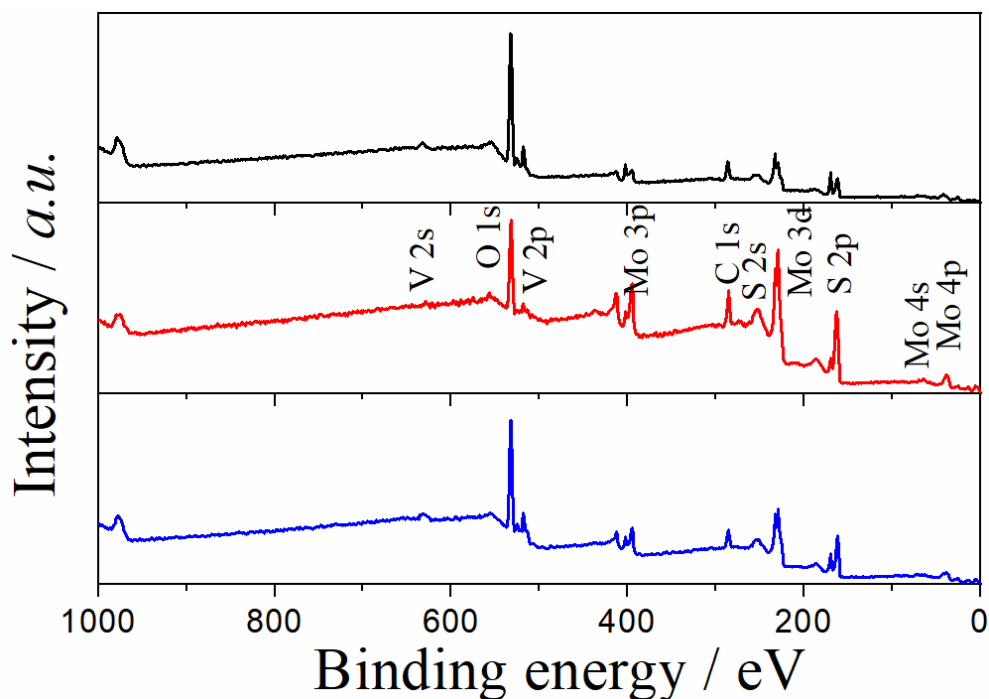


Figure 4.8 XPS survey spectra of VM-33, VM-43 and VM-53.

In order to further understand the elemental compositions and chemical valences, XPS analysis was adopted. As shown in Figure 4.8, the existences of V, Mo and S were confirmed in the structures of VM-33, VM-43 and VM-53. Two peaks at 228.6 eV and 231.9 eV in the high-resolution XPS spectrum of Mo 3d were assigned to $\text{Mo}^{4+} 3d_{5/2}$ and $\text{Mo}^{4+} 3d_{3/2}$ of 1-T phase, respectively (Figure 4.6b), indicating the existence of 1-T phase in the VM-43 [38]. However, the proportions of 1-T phase in VM-33, VM-43 and VM-53 were 29.3%, 26.7% and 27.2%, respectively, according to the XPS peak fitting. Compared with A-MoS₂ [39], the proportion of the 1-T phase based on XPS of Mo 3d was so low that no obvious peaks of J₂ and J₃ were observed from Raman (Figure 4.9). Because the presence of J₁, J₂, and J₃ peaks in Raman is formed by superlattice distortion in the plane of MoS₂ [40]. The phenomenon of no obvious J₂ and J₃ peaks may be due to the low concentration of 1T phase [41], low content of Mo-S bonds in

whole sample, and change of the crystal lattice after V mediating. The small peak of 235.8 eV corresponded to Mo^{6+} , which was attributed to the surface oxidation of MoS_2 [42]. Meanwhile, the V 2p spectrum (Fig. 3c) consisted of four peaks at 524.8, 517.5, 521.0 and 513.3 eV, which were ascribed to $\text{V}^{4+} 2p_{1/2}$, $\text{V}^{4+} 2p_{3/2}$, $\text{V}^{2+} 2p_{1/2}$ and $\text{V}^{2+} 2p_{3/2}$, respectively [43, 44]. Herein, the existences of $\text{V}^{2+} 2p_{1/2}$ and $\text{V}^{2+} 2p_{3/2}$ might be assigned to the strong reducibility of S^{2-} from the decomposition of thioacetamide during the hydrothermal process [45, 46]. The S 2p high-resolution XPS spectrum (Fig. 3f) had two peaks at 161.7 eV and 161.0 eV, which were assigned to S $2p_{1/2}$ and S $2p_{3/2}$, respectively [41]. The other two peaks at 164.1 eV and 162.8 eV were attributed to the supersaturated S-S bonds, which were formed due to the excessive TAA and anchored on the surface of sample [47]. These results indicated that vanadium species was successfully incorporated with MoS_2 to form VMS_2 .

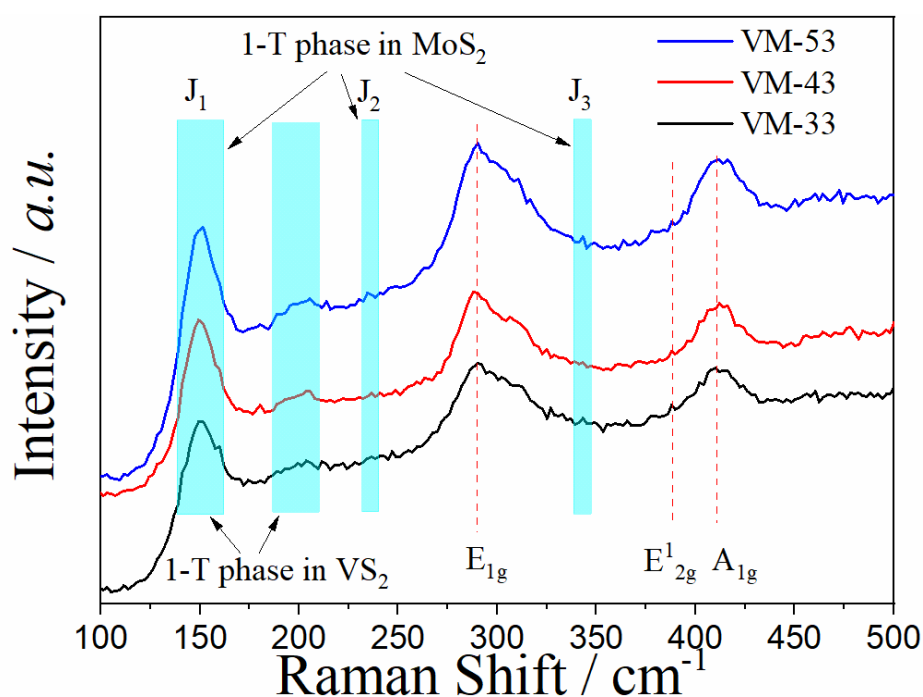


Figure 4.9 Raman spectra of VM-33, VM-43 and VM-53.

4.3.2 Na⁺ storage mechanism

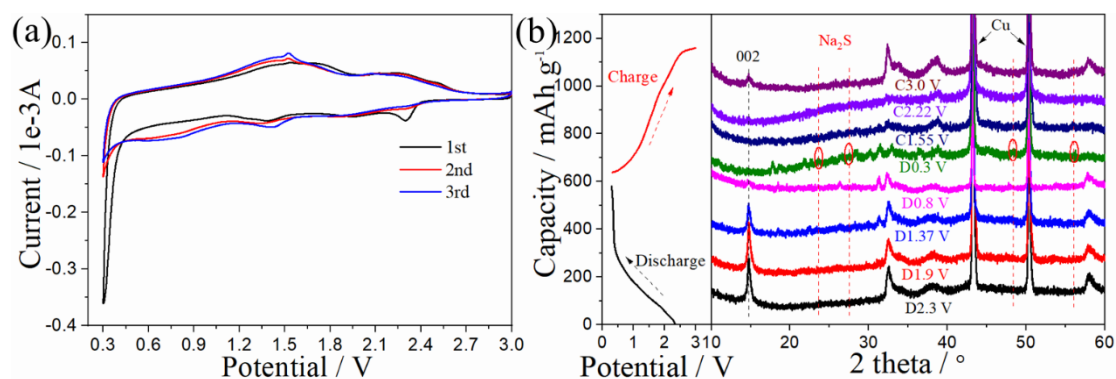


Figure 4.10 (a) Typical CV curves of VM-43 based anode in the first three cycles at a scanning rate of 0.1 mV s⁻¹ in a voltage range of 0.3-3 V; (b) *Ex-situ* XRD patterns of VM-43 at different voltages during the discharging/charging process.

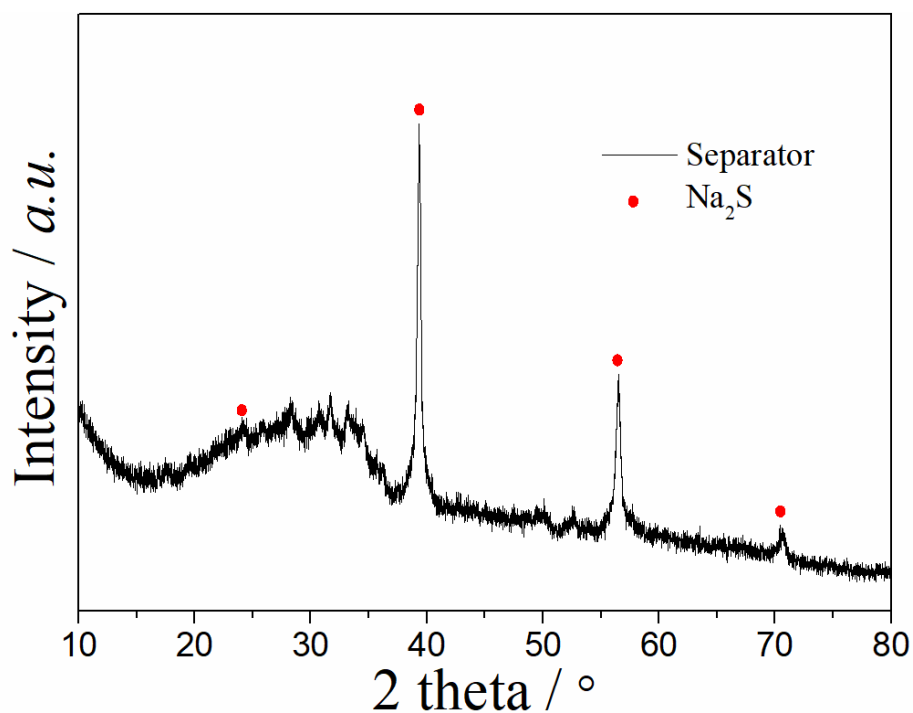


Figure 4.11 XRD pattern of glass fiber separator after the 200th cycle.

Figure 4.10a shows the cycle voltammograms (CVs) of the VM-43 based anode at a scan rate of 0.1 mV s^{-1} in the voltage range of 0.3-3 V. Four reduction peaks located at 2.3, 1.9, 1.37 and 0.3 V were observed during the first discharging process. Meanwhile, two oxidation peaks at 1.55 and 2.22 V appeared in the first charging process. To confirm the crystalline structure changing during the discharging/charging process and understand the Na^+ intercalation/deintercalation mechanism, the *ex-situ* XRD patterns at different stages were measured. As shown in Fig. 4.10b, in the discharging process until the voltage decreased to 0.8 V, the intensity of peak at 14.72° gradually decreased but no any peaks corresponding to Na_2S were observed, revealing that the reduction peaks at 2.3, 1.9 and 1.37 V should be resulted from the multistep intercalations of Na^+ ions into the interlayers of MoS_2 with the formation of Na_xMoS_2 . Subsequently, when the voltage in the discharging process decreased to 0.3 V, three peaks enclosed by the red cycles appeared, which should be associated with the conversion of Na_xMoS_2 to MoS_2 and Na_2S . Interestingly, during the discharge process, a new peak at 31.3° appeared, which may be attributed to the sodium polysulfide produced by supersaturated S-S bonds [48]. It was certificated that polysulfides were the common products during the discharging process when metal sulfides were used as the anode material for batteries [49-51]. Subsequently, the sharp reduction peak appeared at 0.3 V gradually became weaker (Figure 4.10a), which should be due to the gradual formation of solid electrolyte interphase (SEI) layer. Remarkably, the peaks enclosed by the red cycles gradually disappeared during the charging process and the peak corresponding to the (002) plane of MoS_2 was also recovered at 3 V. Herein, the

oxidation peaks at 1.55 and 2.22 V indicated not only the conversion of Mo to MoS₂ but also the deintercalation of Na⁺ ions from the interlayer. In order to further confirm the formation of Na₂S, the XRD analysis for the separator after 200 cycles at 1 A g⁻¹ was also conducted. As shown in Figure 4.11, four peaks appeared at 24.1, 39.2, 56.5 and 70.6° were assigned to (111), (220), (400) and (422) planes of Na₂S, respectively, also demonstrating the formation of Na₂S during the discharging process.

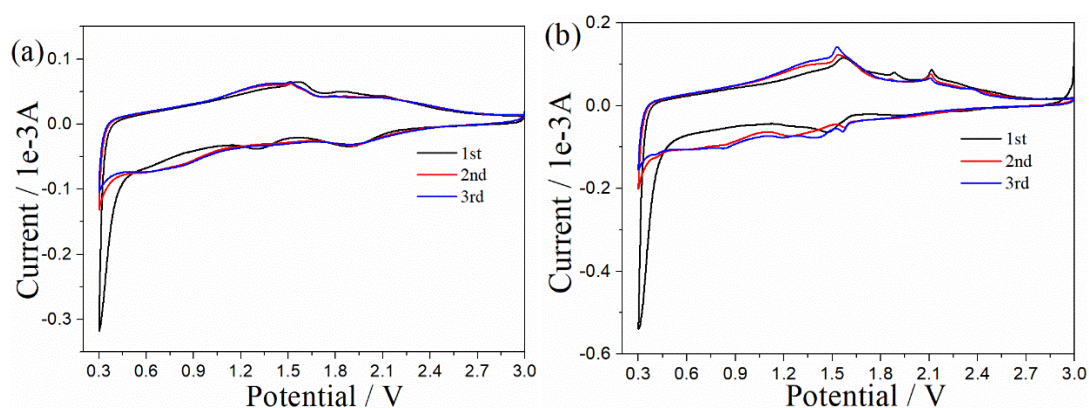


Figure 4.12 Typical CV curves of (a) VM-33 and (b) VM-53 for the first three cycles at a scanning rate of 0.1 mV s⁻¹ in the voltage range of 0.3-3 V.

In addition, the CV curves of VM-33 and VM-53 based anodes were also measured. As shown in Figure 4.12, the same curve pattern as the VM-43 based anode was observed, indicating the same Na⁺ intercalation/deintercalation mechanism during the discharging/charging process.

4.3.3 Electrochemical performance

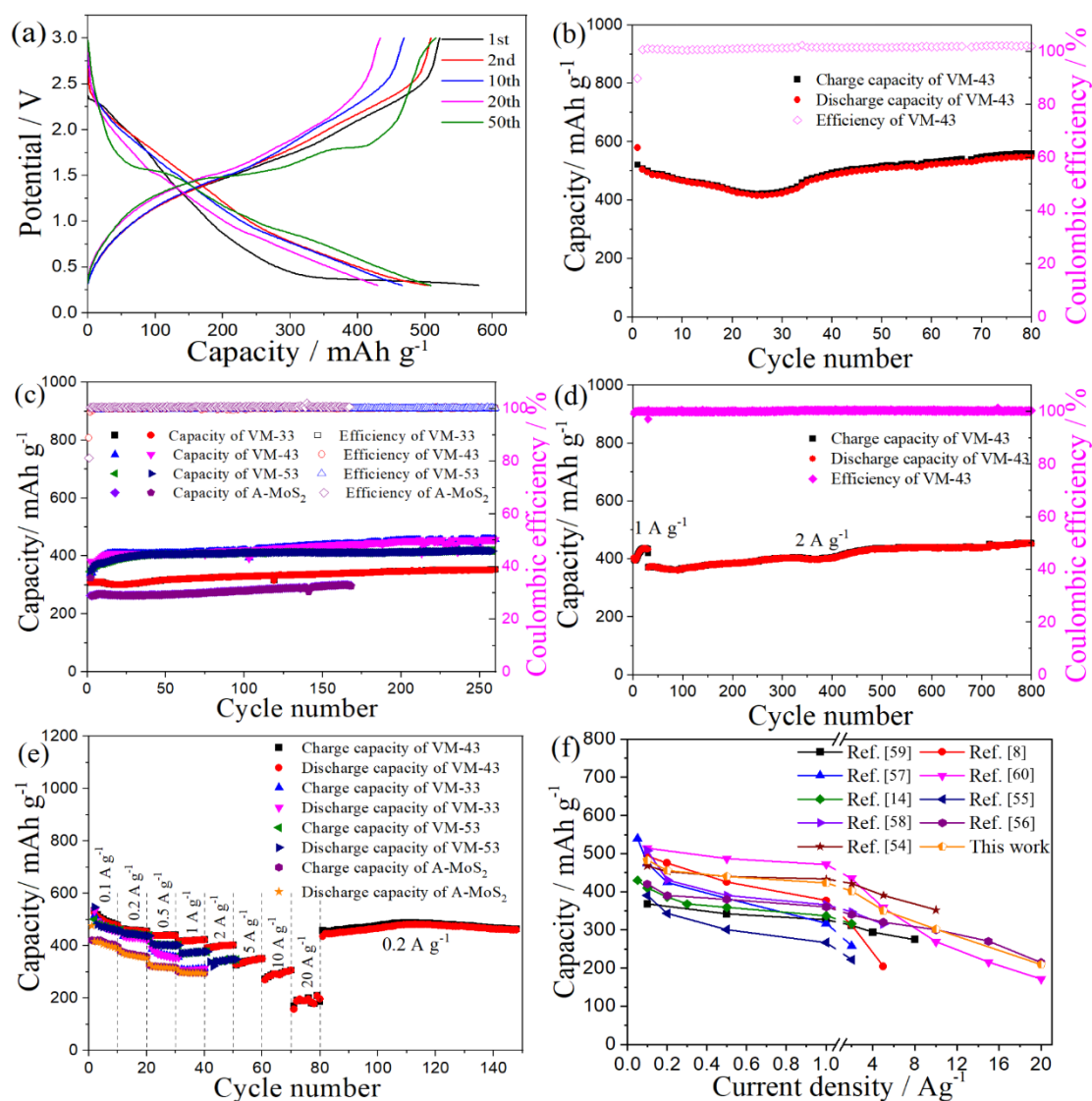


Figure 4.13 (a) Typical galvanostatic charging/discharging profiles in the 1st, 2nd, 10th, 20th, and 50th cycles for the VM-43 based anode at a current density of 100 mA g⁻¹; Cycling performance of the VM-43 based anode at current densities of (b) 100 mA g⁻¹ and (d) 2 A g⁻¹; (c) Cycling performances of the VM-33, VM-43, and VM-53 based anodes at a current density of 1 A g⁻¹; (e) Rate performances of A-MoS₂, VM-33, VM-43 and VM-53 based anodes; (f) Comparison of rate performance of the VM-43 based anode with other MoS₂-based anodes.

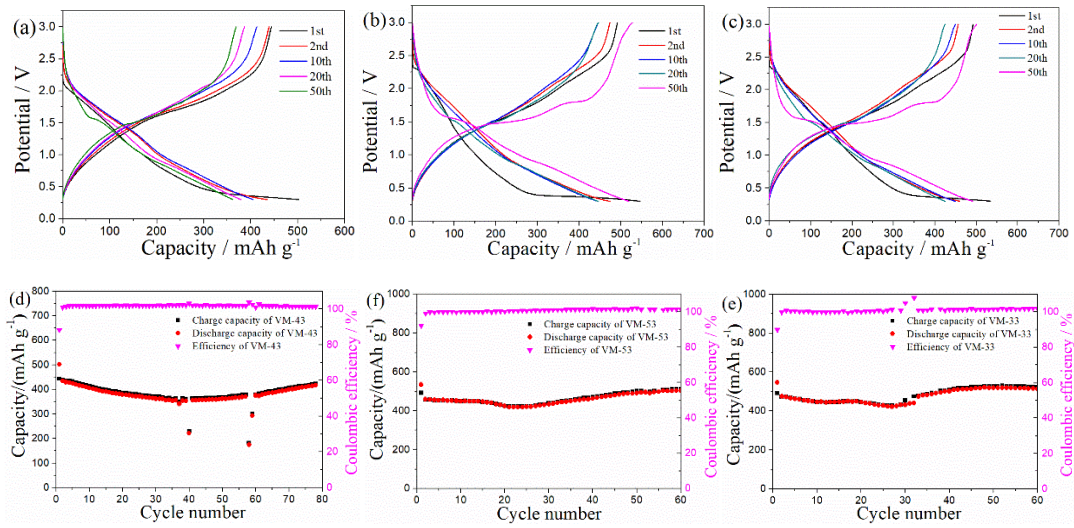


Figure 4.14 Typical galvanostatic charging/discharging profiles at the 1st, 2nd, 10th, 20th and 50th cycles of (a) A-MoS₂, (b) VM-33 and (c) VM-53 at a current density of 100 mA g⁻¹; Cycling performance of (d) A-MoS₂, (e) VM-43 and (f) VM-53 at a current density of 100 mA g⁻¹.

Figure 4.13a shows the galvanostatic charging-discharging profiles in the 1st, 2nd, 10th, 20th and 50th cycles for the VM-43 based anode in the SIBs with a voltage range of 0.3-3 V at a current density of 100 mA g⁻¹. As shown in Figure 4.13a, the initial discharge and charge capacities of 580.1 and 521.5 mAh g⁻¹ were achieved, respectively, with a high initial Coulombic efficiency of 89.88%. Such a high initial Coulombic efficiency should be resulted from the stable and thin SEI layer formed with the ether-based electrolyte, which was benefit for the Na⁺ ions transportation [52]. Subsequently, the second cycle delivered discharge and charge capacities of 505.1 and 508.7 mAh g⁻¹, respectively, with an increased Coulombic efficiency of ~ 100%. For the 10th and 20th cycles, the discharge capacity gradually decreased to 468.6 and 434.1 mAh g⁻¹, respectively. However, after the 50th cycle, a discharge capacity of 509.2 mAh g⁻¹ was

achieved also with a Coulombic efficiency at $\sim 100\%$. The continuous and progressive capacity changing during the cycling process is shown in Figure 4.13b. One can see that the discharge capacity continuously decreased in the first several cycles and thereafter gradually increased and finally remained at 548.1 mAh g^{-1} after the 80th cycle. In contrast, as shown in Figure 4.14a-c, the initial discharge and charge capacities of 502 and 443.9 mAh g^{-1} , 547 and 491.8 mAh g^{-1} , 534 and 492 mAh g^{-1} were delivered for A-MoS₂, VM-33 and VM-53 based anodes, respectively, which were lower than those of VM-43. In addition, at a current density of 100 mA g^{-1} , the A-MoS₂, VM-33 and VM-53 based anodes exhibited reversible specific capacities of 375.5 , 514 and 504 mAh g^{-1} , respectively, after the 60th cycle (Figure 4.14d-f), they were also lower than that of the VM-43 based anode (521.8 mAh g^{-1}).

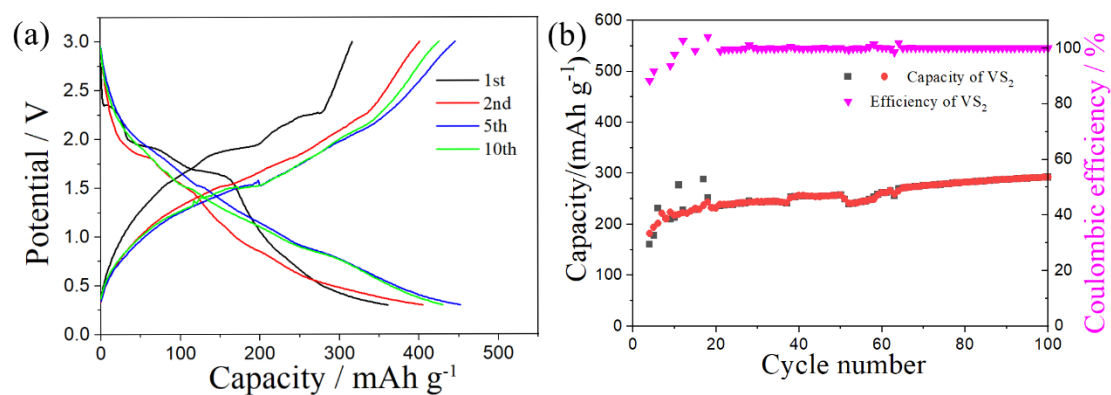


Figure 4.15 (a) Typical galvanostatic charging/discharging profiles at the 1st, 2nd, 5th, and 10th cycles of VS₂; (b) Cycling performance of VS₂ at a current density of 1 A g^{-1} .

In addition, the specific capacity of VM-43 was higher than that of VS₂ (425 mAh g^{-1} at a current density of 100 mA g^{-1} as shown in Figure 4.15a). Notably, the coulombic efficiency was higher than 100% in the later stage of cycling test in Fig. 5b, which may be attributed to the partial decomposition of the SEI layer and the reduction of sodium

polysulfides during the charging process [50, 53]. Both of them could provide higher charging capacity, resulting in a coulomb efficiency even higher than 100%.

The cycling stability test results of the A-MoS₂, VM-33, VM-43 and VM-53 based anodes are shown in Figure 4.13c, in which the anodes were tested at a current density of 1 A g⁻¹. It is clearly seen that the VM-43 based anode delivered a high specific capacity of 455.6 mAh g⁻¹ with a Coulombic efficiency of ~100% even after the 260th cycle. In comparison, the A-MoS₂, VM-33, VM-53, and VS₂ (Figure 4.15b) based anodes only exhibited reversible capacities of 297.1, 352.7, 417.5 and 293.4 mA g⁻¹, respectively, which were lower than that of VM-43 based anode. Furthermore, at a large current density of 2A g⁻¹, the cycling stability of VM-43 based anode was extended to 800 cycles with a reversible capacity of 451.6 mAh g⁻¹ as well as a ~100% Coulombic efficiency (Figure 4.13d). All these results obviously revealed that the VM-43 based anode had excellent cycling stability.

Figure 4.13e shows the rate performances of A-MoS₂, VM-33, VM-43 and VM-53 based anodes. It is clearly seen that the VM-43 based anode delivered reversible capacities of 479.8, 453.4, 438.7, 422, 401.8, 349.8 and 305.6 mAh g⁻¹ at current densities of 0.1, 0.2, 0.5, 1, 2, 5 and 10 A g⁻¹, respectively. In particular, even at a very high current density of 20 A g⁻¹, the VM-43 based anode also exhibited a high reversible capacity of 207.4 mAh g⁻¹. Most importantly, when the current density was returned to 0.2 A g⁻¹, the reversible capacity was also recovered to 460 mAh g⁻¹ after the 150th cycle, revealing its excellent rate performance. By contrast, the A-MoS₂, VM-33 and VM-53 based anodes showed lower rate performances with reversible capacities of 294.5,

312.8 and 377.4 mAh g⁻¹, respectively, at a large current density of 1 A g⁻¹ than the VM-43 based anode. Interestingly, at lower current densities of 0.1 and 0.2 A g⁻¹, the reversible capacity of VM-43 based anode decreased at first and then gradually increased at larger current densities of 0.5, 1, 2, 5, 10 and 20 A g⁻¹, indicating the fast kinetics of Na⁺ intercalation/deintercalation in this anode. This phenomenon was also observed in Figure 4.13b.

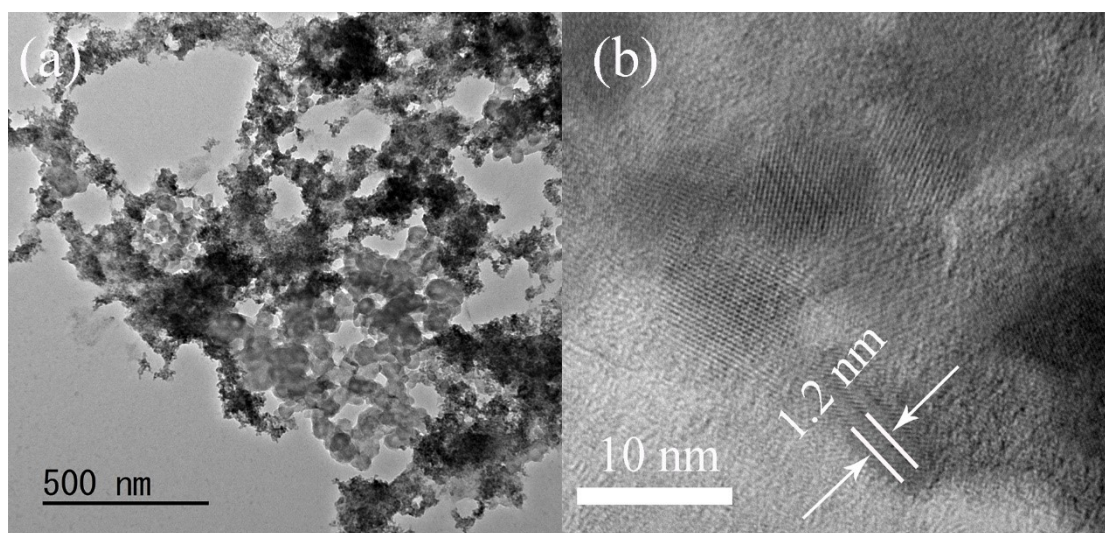


Figure 4.16 (a) TEM and (b) HRTEM images of VM-43 after the 800th cycle at the current density of 2 A g⁻¹.

Herein, as shown in Fig. 4.16, the interlayer spacing could be expanded during the discharging/charging process, which should be benefit for the Na⁺ storage and intercalation/deintercalation. Fig. 5e compared the rate performances of the VM-43 based anode with other reported MoS₂-based ones. Notably, the rate performance of the present VM-43 based anode was more excellent than those of most MoS₂-based ones [8, 14, 54-60].

4.3.4 Electrochemical kinetics and EIS analysis

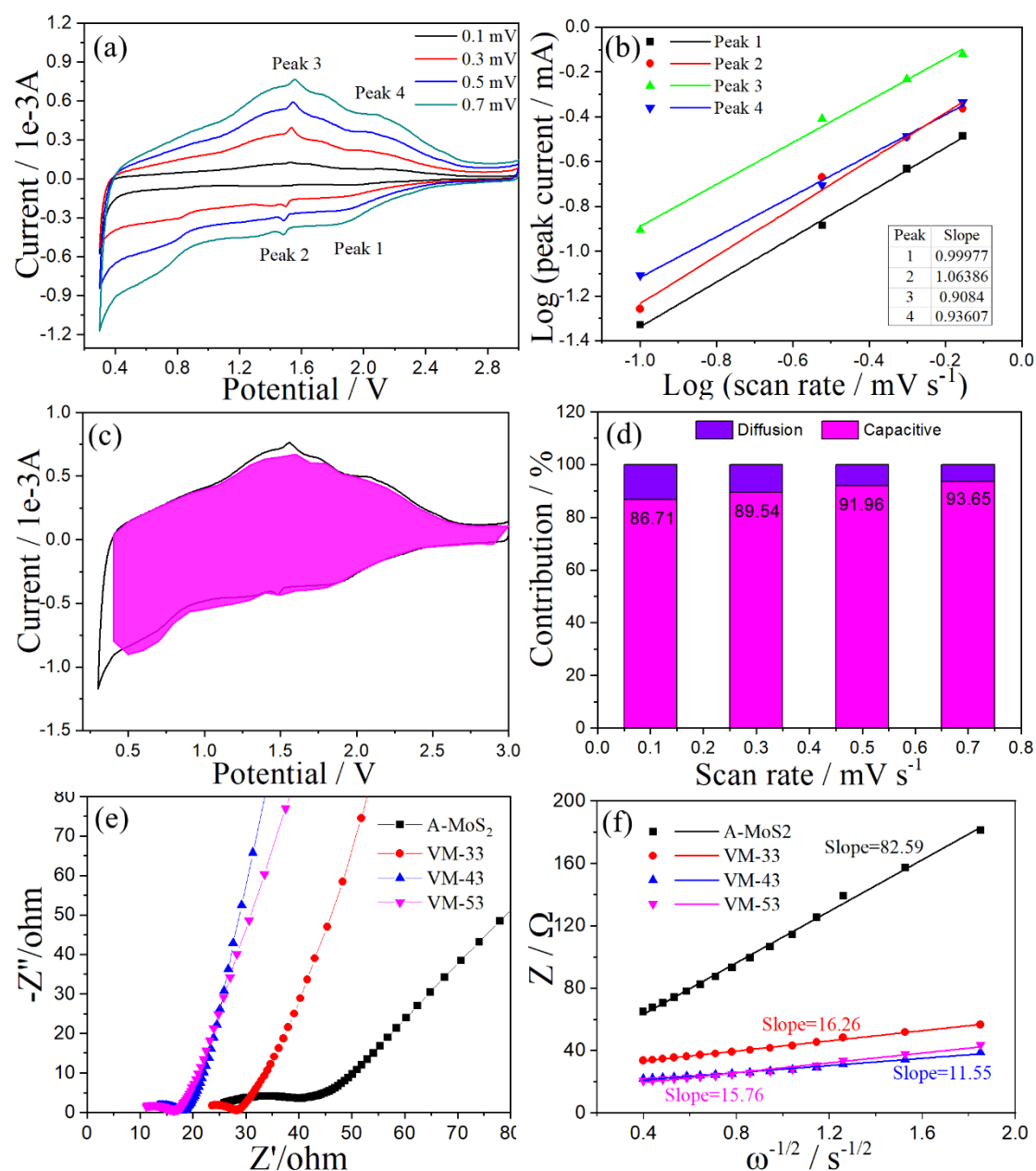


Figure 4.17 (a) CV curves of VM-43 based anode at different scan rates from 0.1 to 0.7 mV s^{-1} , (b) corresponding $\log i$ vs. $\log v$ plots of peaks 1, 2, 3 and 4; (c) capacitive contribution of the VM-43 material in comparison to the total current at 0.7 mV s^{-1} ; (d) capacitive contribution of MoS₂-MS at different scan rates from 0.1 to 0.7 mV s^{-1} , (e) Nyquist plots of the A-MoS₂, VM-33, VM-43, and VM-53 based anodes.

Figure 4.17a shows the reaction kinetics related to the VM-43 based anode. One can see that similar CV curves were obtained at different scan rates from 0.1 to 0.7 mV s⁻¹. Generally, the charge storing in nanomaterials can be realized by a diffusion-controlled process or a surface-controlled process (pseudocapacitive) [61, 62], which can be evaluated based on the following equation [63, 64]:

$$i = av^b \tag{1}$$

where both of a and b are constants, i and v are the current and the scan rate, respectively. Herein, the b -value is generally in a range of 0.5-1, in which b -value approaching 0.5 indicates a diffusion-controlled process whereas b -value close to 1 means a surface-controlled pseudo-capacitive process. In this study, as shown in Figure 4.17b, the b -values of 0.999, 1.063, 0.908 and 0.936 corresponding to the peaks 1, 2,3 and 4 were obtained by the fitting of $\log i$ vs. $\log v$ related to the VM-43 based anode, indicating a surface-controlled pseudo-capacitive occurred for the charge storage in this material. In addition, for the VM-33 and VM-53 based anodes, the b -values were also close to 1 (Figures 4.19b and 4.20b) since they were the same type materials as the VM-43.

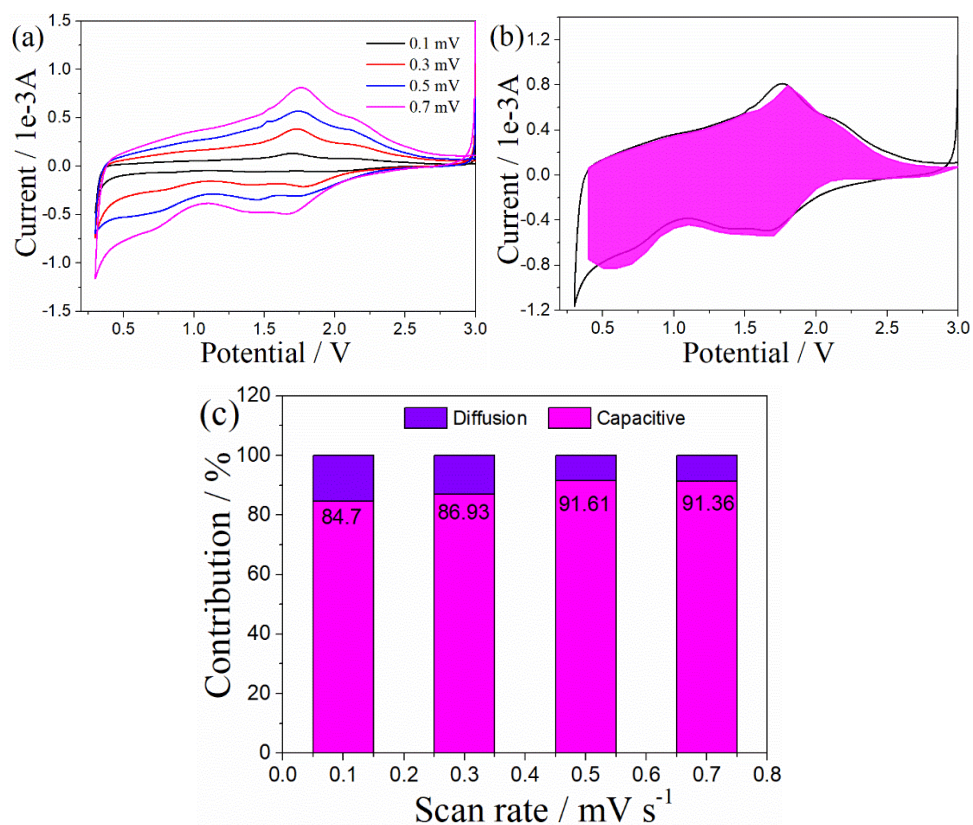


Figure 4.18 (a) CV curves of A-MoS₂ at different scan rates from 0.1 to 0.7 mV s⁻¹, (b) capacitive contribution of A-MoS₂ related to the total current at 0.7 mV s⁻¹; (c) capacitive contribution of A-MoS₂ at different scan rates from 0.1 to 0.7 mV s⁻¹.

Meanwhile, the contributions from the diffusion-controlled process and the pseudocapacitive process can be calculated using the following equation [65]:

$$i = k_1v + k_2v^{1/2} \quad (2)$$

where k_1 and k_2 are constants, i and v stand for the current value at the specific voltage and the scan rate, respectively; k_1v and $k_2v^{1/2}$ represent the contributions of capacitive and diffusion processes, respectively. Thus, the contributions of pseudocapacitive process at different scan rates can be calculated by the values of k_1 and k_2 obtained from the fixed voltage. As shown in Figure 4.17c, the capacitive contribution reached to ~93.65% at the scan rate of 0.7 mV s⁻¹ for the VM-43 based anode, indicating excellent

charge transfer kinetics. Figure 4.17d displays the contributions of capacitive process at different scan rates. One can see that the capacitive contributions of 86.71, 89.54, 91.96 and 93.65 % were achieved at the scan rates of 0.1, 0.3, 0.5, and 0.7 mV s^{-1} , respectively. In contrast, the capacitive contributions of 84.7, 86.93, 91.61, and 91.36 % were achieved for the A-MoS₂-based anode at the different scan rates of 0.1, 0.3, 0.5, and 0.7 mV s^{-1} , respectively (Figure 4.18), which were also lower than those of VM-33 and VM-53 based anodes (Figures 4.19 and 4.20). Thus, the capacitive contribution of the VMS₂-based anode was higher than that of A-MoS₂ based anode, indicating a favorable charge transfer kinetics after the V species mediating.

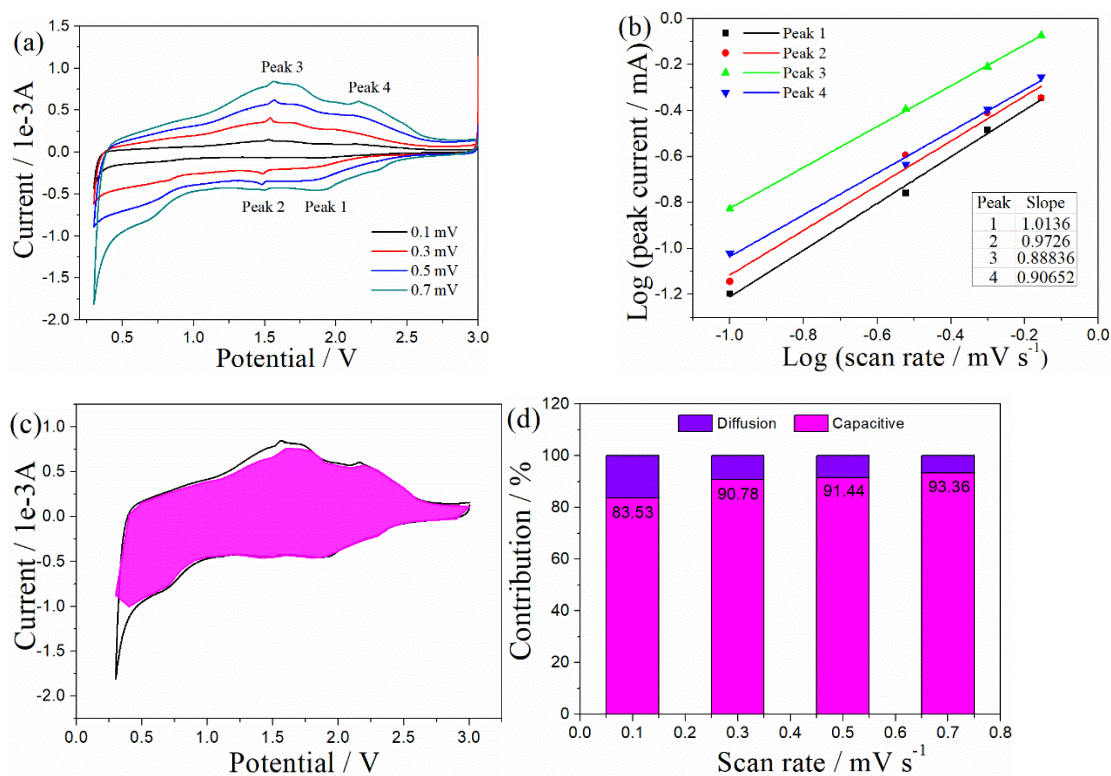


Figure 4.19 (a) CV curves of VM-33 based anode at different scan rates from 0.1 to 0.7 mV s^{-1} , (b) corresponding $\log i$ vs. $\log v$ plots of the peaks 1, 2, 3, and 4; (c) capacitive contribution of VM-43 related to the total current at 0.7 mV s^{-1} ; (d) capacitive contribution of MoS₂-MS at different scan rates from 0.1 to 0.7 mV s^{-1} .

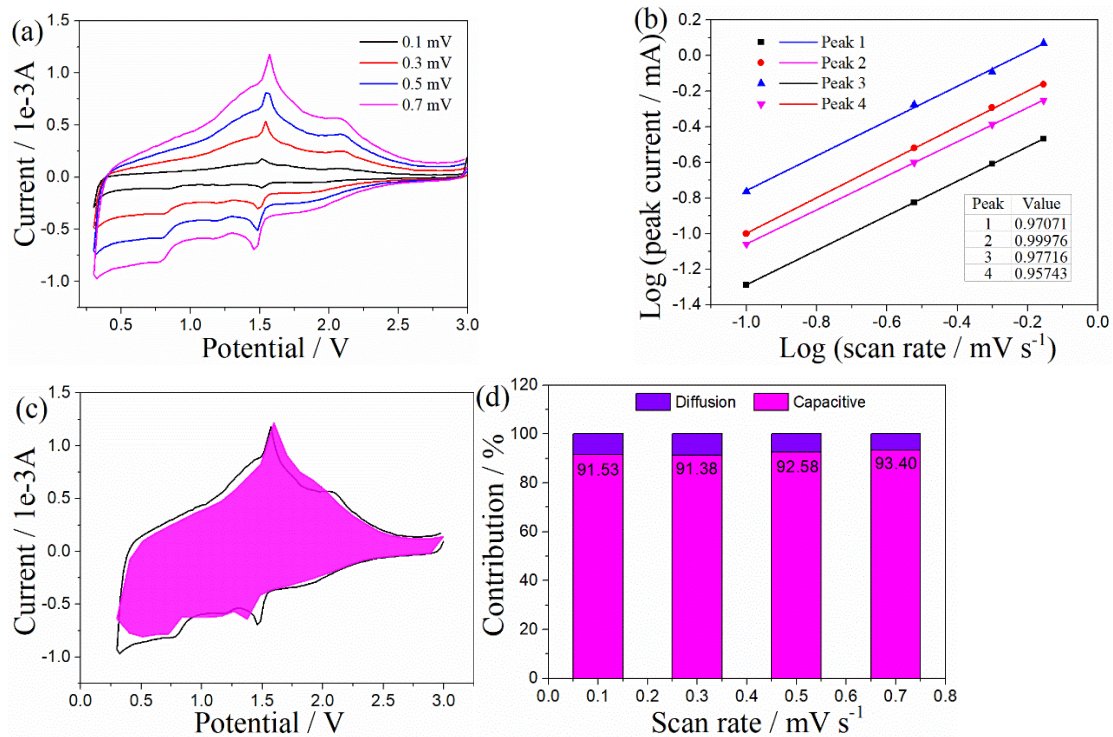


Figure 4.20 (a) CV curves of VM-53 based anode at different scan rates from 0.1 to 0.7 mV s^{-1} , (b) corresponding $\log i$ vs. $\log v$ plots of peak 1, 2, 3, and 4; (c) capacitive contribution of VM-43 related to the total current at 0.7 mV s^{-1} ; (d) capacitive contribution of $\text{MoS}_2\text{-MS}$ at different scan rates from 0.1 to 0.7 mV s^{-1} .

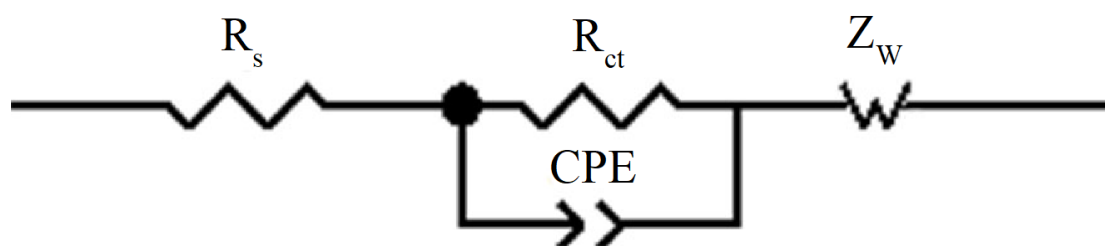


Figure 4.21 The equivalent circuit used for the analysis of the impedance plots.

Table 4.2 Fitting results of Nyquist plots based on the equivalent circuit in Fig. S8 after the 20th cycle.

Electrode	R_s	R_{ct}
A-MoS ₂	22.66	21.38
VM-33	20.23	7.635
VM-43	10.51	7.149
VM-53	8.92	7.115

Figure 4.17e shows Nyquist plots of the A-MoS₂, VM-33, VM-43, and VM-53 based anode after 20 cycles at a current density of 0.2 A g⁻¹, which contained a slope line in the low frequency region and a semicircle in the high frequency region, corresponding to the Warburg impedance (Z_w) related to the Na⁺ diffusion and the charge-transfer resistance (R_{ct}), respectively [66, 67]. Based on the equivalent circuit as shown in Figure 4.21, the R_{ct} was calculated. As summarized in Table 4.2, the R_{ct} values were 21.38, 7.635, 7.149, and 7.115 Ω for A-MoS₂, VM-33, VM-43 and VM-53 based anodes, respectively, indicating that mediating of vanadium species effectively improved the electronic conductivity. To gain the diffusion characteristics of Na⁺ ions, the Warburg impedance at the low frequency region was further analyzed by using the following two equations [68, 69]:

$$Z' = R_s + R_{ct} + \sigma_w \omega^{-0.5} \quad (3)$$

$$D = \frac{R^2 T^2}{2A^2 n^4 F^4 C^2 \sigma_w^2} \quad (4)$$

where σ_w is the Warburg impedance coefficient, which can be obtained from the slope (Figure 4.17f) by linear fitting of Z' vs. $\omega^{-0.5}$ using Eqn. (3); R , T , A , n , F , and C are the gas constant, the absolute temperature, the surface area of the anode, the number of electrons transferred, the Faraday's constant, and the molar concentration of the Na^+ ions, respectively. After 20 cycles, the Warburg coefficient of the VM-43 based anode was 11.55, which was lower than those of A-MoS₂ (82.59), VM-33 (16.26) and VM-53 (15.76) based anodes, indicating the faster Na^+ ion diffusion in it. This result was also consistent with the superb rate performance of the VM-43 based anode (Figure 4.13e).

4.3.5 DFT calculations

Table 4.3. The unit cell parameters of pure MoS₂ and VMoS₂ based on DFT calculations.

Species	a (Å)	b (Å)	c (Å)
MoS ₂	6.36184	6.36184	7.72638
VMS ₂	6.38210	6.38210	7.59891

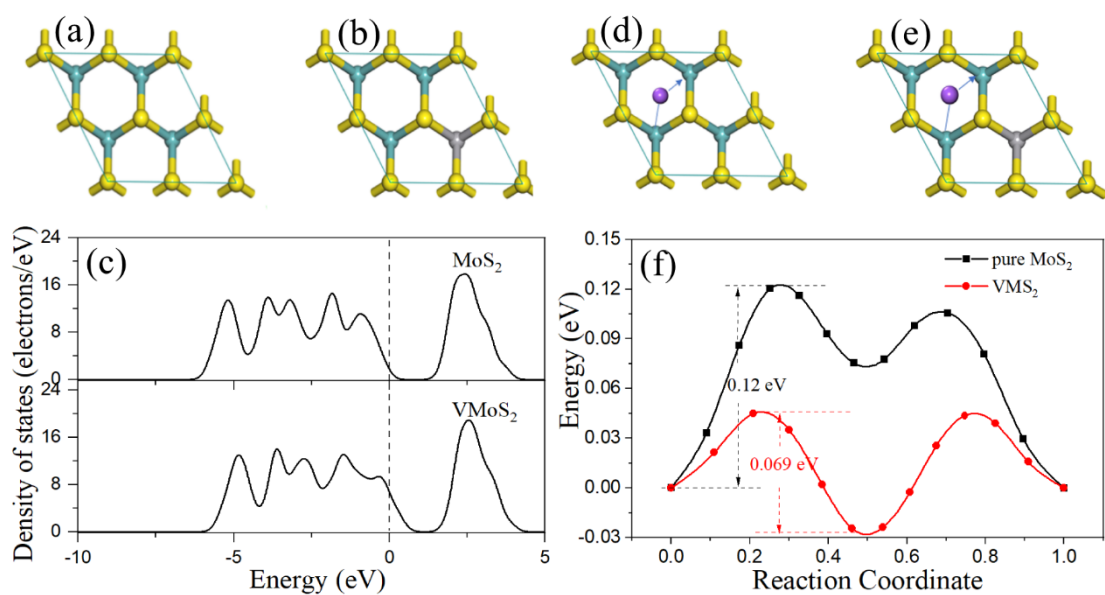


Figure 4.22 Optimized structures of the (a) pure MoS₂ and (b) VMS₂; (c) density of states of the pure MoS₂ and VMS₂; Na⁺ migration path in the interlayer of the (d) pure MoS₂ and (e) VMS₂; (f) energy profiles along the diffusion path.

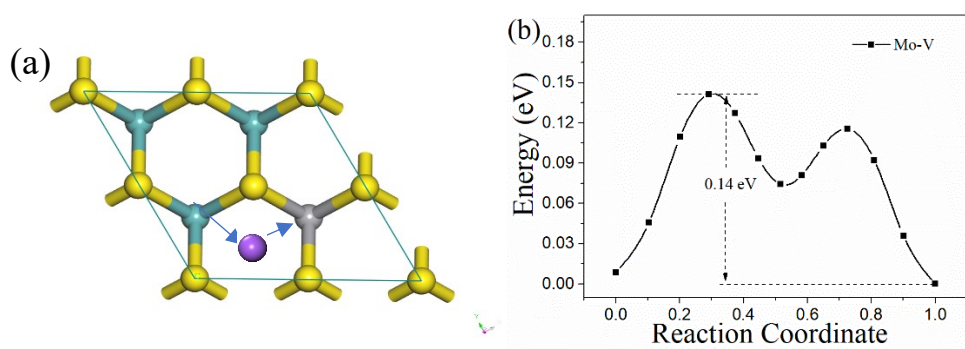


Figure 4.23 (a) Na⁺ migration path in the interlayer of VMS₂ from Mo to V; (b) energy profiles along the diffusion path.

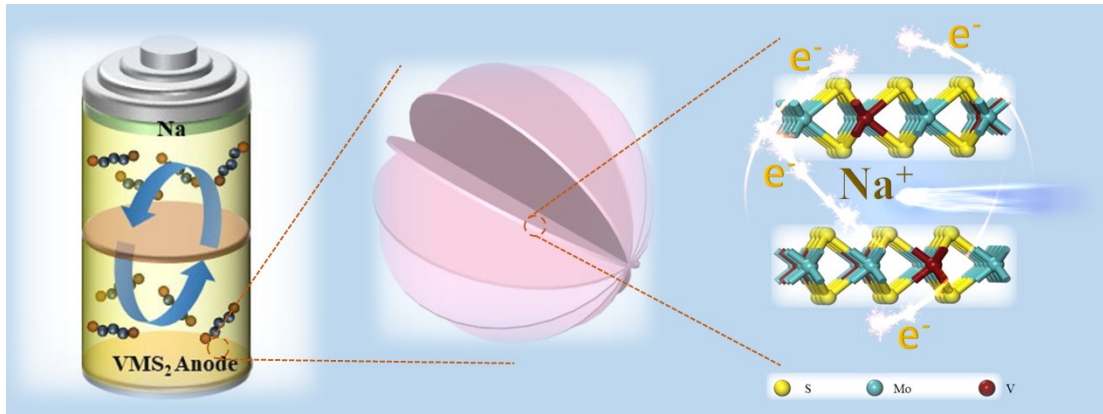


Figure 4.24 Illustration of Na^+ diffusion and electronic transmission during the charging/discharging processes in the VMS_2 based anode.

DFT calculations were carried out to further confirm the effect of V-mediating on the enhancement of the conductivity and promoting of the Na^+ ion diffusion. Figures 4.22a and b show the structure models of the pure MoS_2 and VMS_2 , respectively. The calculated unit cell parameters of MoS_2 and VMS_2 are summarized in Table 4.3. The distance between the VMoS_2 layers was 7.59891, which was narrower than that of pure MoS_2 (7.72638), indicating the decrease of interlayer spacing after the V mediating. This result was consistent with the TEM observations (Figures 4.4d and e). Meanwhile, the density of states of the pure MoS_2 and VMS_2 are shown in Figure 4.22c. It is obvious that the Fermi level after the V-mediating merged into the valence band, demonstrating that VMS_2 possessed the metallic property. Thus, V-S bond in the structure of MoS_2 could obviously increase the electrical conductivity, which was also in good agreement with EIS result (Figure 4.17e). In addition, the defects and 1-T phase also could contribute to the conductivity improvement [70]. It was reported that the energy barrier of diffusion paths as shown in Figures 4.22d and e should be the lowest ones [71, 72], therefore, we choose these diffusion paths to calculate the energy barrier by the

CASTEP implemented in Materials Studio software using the pseudopotential method [29]. As shown in Figure 4.22f, the energy barrier in VMS_2 was 0.069 eV, which was approximately 42.5% lower than that calculated for the pure MoS_2 (0.12 eV). In addition, the energy barrier of diffusion path from Mo to V was calculated to be 0.14 eV (Figure 4.23), which was slightly higher than that of diffusion path from Mo to Mo in the pure MoS_2 . The smaller energy barrier related to the VMS_2 indicated that Na^+ could migrate more easily between the layers of VMS_2 material when compared with the pure MoS_2 . Thus, the higher electrical conductivity, smaller energy barrier and lower Warburg coefficient after the V mediating could promote the electron and Na^+ ion transportation, thereby improving the electrochemical kinetics, resulting in more the contribution from pseudocapacitive process as illustrated in Figure 4.24.

4.4 Conclusions

In summary, a series of high-performance VMS_2 based anode materials for SIBs were successfully synthesized with different V:Mo molar ratios in the precursors through a facile one-step hydrothermal method. The experimental and DFT calculation results revealed that the V mediating in the structure of MoS_2 not only significantly enhanced the conductivity, but also greatly increased the electrochemical kinetics with dominated the pseudocapacitive contribution for the sodium ion storage. As a result, the VMoS_2 material named VM-43 prepared with the V:Mo molar ratio of 4:3 was found to have the disordered structure with rich defects, and exhibited high reversible capacity (i.e., maintaining at 548.1 mAh g^{-1} over 80 cycles with 100 mA g^{-1}), excellent

cycling stability (i.e., maintaining at 451.6 mAh g⁻¹ over 800 cycles with 2 A g⁻¹) and superb rate performance (maintaining 207.4 mAh g⁻¹ with 20 A g⁻¹). It is expected that this the novel electrode material preparation strategy could significantly decrease the cost, increase the electrochemical performance, and promote the commercialization of SIBs.

References

- [1] Z. Hu, Z. Tai, Q. Liu, S.-W. Wang, H. Jin, S. Wang, W. Lai, M. Chen, L. Li, L. Chen, Z. Tao, S.L. Chou, Ultrathin 2D TiS₂ nanosheets for high capacity and long-life sodium ion batteries, *Adv. Energy Mater.* 9 (2019) 1803210.
- [2] P.K. Nayak, L. Yang, W. Brehm, P. Adelhelm, From lithium-ion to sodium-ion batteries: advantages, challenges, and surprises, *Angew. Chem. Int. Edit.* 57 (2018) 102-120.
- [3] C. Delmas, Sodium and sodium-ion batteries: 50 years of research, *Adv. Energy Mater.* 8 (2018) 1703137.
- [4] N. Yabuuchi, K. Kubota, M. Dahbi, S. Komaba, Research development on sodium-ion batteries, *Chem. Rev.* 114 (2014) 11636-11682.
- [5] H. Pan, Y.S. Hu, L. Chen, Room-temperature stationary sodium-ion batteries for large-scale electric energy storage, *Energ. Environ. Sci.* 6 (2013) 2338.
- [6] Q. Pan, Q. Zhang, F. Zheng, Y. Liu, Y. Li, X. Ou, X. Xiong, C. Yang, M. Liu, Construction of MoS₂/C hierarchical tubular heterostructures for high-performance sodium ion batteries, *ACS Nano* 12 (2018) 12578-12586..

- [7] X. Hu, W. Zhang, X. Liu, Y. Mei, Y. Huang, Nanostructured Mo-based electrode materials for electrochemical energy storage, *Chem. Soc. Rev.* 44 (2015) 2376-2404.
- [8] M. Hou, Y. Qiu, G. Yan, J. Wang, D. Zhan, X. Liu, J. Gao, L. Lai, Aging mechanism of MoS₂ nanosheets confined in N-doped mesoporous carbon spheres for sodium-ion batteries, *Nano Energy* 62 (2019) 299-309.
- [9] J. Zhou, L. Wang, M. Yang, J. Wu, F. Chen, W. Huang, N. Han, H. Ye, F. Zhao, Y. Li, Y. Li, Hierarchical VS₂ nanosheet assemblies: a universal host material for the reversible storage of alkali metal ions, *Adv. Mater.* 29 (2017).
- [10] Z. Liu, A. Daali, G.L. Xu, M. Zhuang, X. Zuo, C.J. Sun, Y. Liu, Y. Cai, M.D. Hossain, H. Liu, K. Amine, Z. Luo, Highly reversible sodiation/desodiation from a carbon-sandwiched SnS₂ nanosheet anode for sodium ion batteries, *Nano Lett.* 20 (2020) 3844-3851.
- [11] X. Hu, Y. Liu, J. Li, G. Wang, J. Chen, G. Zhong, H. Zhan, Z. Wen, Self-assembling of conductive interlayer-expanded WS₂ nanosheets into 3D hollow hierarchical microflower bud hybrids for fast and stable sodium storage, *Adv. Funct. Mater.* 30 (2019) 1907677.
- [12] S. Anwer, Y. Huang, B. Li, B. Govindan, K. Liao, J.C. W, F. Wu, R. Chen, L. Zheng, Zheng, Nature-inspired, graphene-wrapped 3D MoS₂ ultrathin microflower architecture as a high-performance anode material for sodium-ion batteries, *ACS Appl. Mater. Inter.* 11 (2019) 22323-22331.
- [13] H. Chen, T. Song, L. Tang, X. Pu, Z. Li, Q. Xu, H. Liu, Y. Wang, Y. Xia, In-situ growth of vertically aligned MoS₂ nanowalls on reduced graphene oxide enables a large

capacity and highly stable anode for sodium ion storage, *J. Power Sources* 445 (2020) 227271.

[14] Y. Fang, D. Luan, Y. Chen, S. Gao, X.W. Lou, Rationally designed three-layered $\text{Cu}_2\text{S}@ \text{carbon}@ \text{MoS}_2$ hierarchical nanoboxes for efficient sodium storage, *Angew. Chem. Int. Edit.* 59 (2020) 7178-7183.

[15] S. Kim, M. Hankel, W. Cha, G. Singh, J.M. Lee, I.Y. Kim, A. Vinu, Theoretical and experimental investigations of mesoporous $\text{C}_3\text{N}_5/\text{MoS}_2$ hybrid for lithium and sodium ion batteries, *Nano Energy* 72 (2020) 104702.

[16] K. Yao, Z. Xu, J. Huang, M. Ma, L. Fu, X. Shen, J. Li, M. Fu, Bundled defect-rich MoS_2 for a high-rate and long-life sodium-ion battery: achieving 3D diffusion of sodium ion by vacancies to improve kinetics, *Small* 15 (2019) 1805405.

[17] J.B. Cook, H.-S. Kim, Y. Yan, J.S. Ko, S. Robbennolt, B. Dunn, S.H. Tolbert, Mesoporous MoS_2 as a transition metal dichalcogenide exhibiting pseudocapacitive Li and Na-ion charge storage, *Adv. Energy Mater.* 6 (2016) 1501937.

[18] W. Sun, P. Li, X. Liu, J. Shi, H. Sun, Z. Tao, F. Li, J. Chen, Size-controlled MoS_2 nanodots supported on reduced graphene oxide for hydrogen evolution reaction and sodium-ion batteries, *Nano Res.* 10 (2017) 2210-2222.

[19] Y. Wang, Q. Qu, G. Li, T. Gao, F. Qian, J. Shao, W. Liu, Q. Shi, H. Zheng, 3D interconnected and multiwalled $\text{carbon}@ \text{MoS}_2 @ \text{carbon}$ hollow nanocables as outstanding anodes for Na-ion batteries, *Small* 12 (2016) 6033-6041.

[20] Z. Chen, D. Yin, M. Zhang, Sandwich-like $\text{MoS}_2 @ \text{SnO}_2 @ \text{C}$ with high capacity and stability for sodium/potassium ion batteries, *Small* 14 (2018) 1703818.

- [21] L. Jing, G. Lian, F. Niu, J. Yang, Q. Wang, D. Cui, C.-P. Wong, X. Liu, Few-atomic-layered hollow nanospheres constructed from alternate intercalation of carbon and MoS₂ monolayers for sodium and lithium storage, *Nano Energy* 51 (2018) 546-555.
- [22] Y. Liu, X. Hu, G. Zhong, J. Chen, H. Zhan, Z. Wen, Layer-by-layer stacked nanohybrids of N,S-co-doped carbon film modified atomic MoS₂ nanosheets for advanced sodium dual-ion batteries, *J. Mater. Chem. A* 7 (2019) 24271-24280.
- [23] B. Lu, J. Liu, R. Hu, H. Wang, J. Liu, M. Zhu, C@MoS₂@PPy sandwich-like nanotube arrays as an ultrastable and high-rate flexible anode for Li/Na-ion batteries, *Energy Storage Mater.* 14 (2018) 118-128.
- [24] W. Tang, X. Wang, Y. Zhong, D. Xie, X. Zhang, X. Xia, J. Wu, C. Gu, J. Tu, Hierarchical MoS₂/carbon composite microspheres as advanced anodes for lithium/sodium-ion batteries, *Chemistry* 24 (2018) 11220-11226.
- [25] X. Xu, R. Zhao, W. Ai, B. Chen, H. Du, L. Wu, H. Zhang, W. Huang, T. Yu, Controllable design of MoS₂ nanosheets anchored on nitrogen-doped graphene: toward fast sodium storage by tunable pseudocapacitance, *Adv. Mater.* 30 (2018) 1800658.
- [26] R. Sun, Q. Wei, J. Sheng, C. Shi, Q. An, S. Liu, L. Mai, Novel layer-by-layer stacked VS₂ nanosheets with intercalation pseudocapacitance for high-rate sodium ion charge storage, *Nano Energy* 35 (2017) 396-404.
- [27] J. Wang, N. Luo, J. Wu, S. Huang, L. Yu, M. Wei, Hierarchical spheres constructed by ultrathin VS₂ nanosheets for sodium-ion batteries, *J. Mater. Chem. A* 7 (2019) 3691-3696.

- [28] Y. Jing, Z. Zhou, C.R. Cabrera, Z. Chen, Metallic VS₂ monolayer: a promising 2D anode material for lithium ion batteries, *J. Phys. Chem. C* 117 (2013) 25409-25413.
- [29] S.J. Clark, M.D. Segall, C.J. Pickard, P.J. Hasnip, M.I. Probert, K. Refson, M.C. Payne, First principles methods using CASTEP, *Z. Krist.-Cryst. Mater.* 220 (2005) 567-570.
- [30] J. Harl, G. Kresse, Accurate bulk properties from approximate many-body techniques, *Phys. Rev. Lett.* 103 (2009) 056401.
- [31] J.P. Perdew, K. Burke, M. Ernzerhof, Generalized gradient approximation made simple, *Phys. Rev. Lett.* 77 (1996) 3865.
- [32] X. Li, T. Li, S. Huang, J. Zhang, M.E. Pam, H. Yang, Controllable synthesis of 2D molybdenum disulfide (MoS₂) for energy storage applications, *ChemSusChem* 13 (2020) 1379-1391.
- [33] H. Qiu, H. Zheng, Y. Jin, M. Jia, Q. Yuan, C. Zhao, M. Jia, Dopamine-derived N-doped carbon-encapsulated MoS₂ microspheres as a high-performance anode for sodium-ion batteries, *Ionics* 26 (2020) 5543-5551.
- [34] B. Chen, Y. Meng, F. He, E. Liu, C. Shi, C. He, L. Ma, Q. Li, J. Li, N. Zhao, Thermal decomposition-reduced layer-by-layer nitrogen-doped graphene/MoS₂/nitrogen-doped graphene heterostructure for promising lithium-ion batteries, *Nano Energy* 41 (2017) 154-163.
- [35] W. Ye, F. Wu, N. Shi, H. Zhou, Q. Chi, W. Chen, S. Du, P. Gao, H. Li, S. Xiong, Metal-Semiconductor Phase Twinned Hierarchical MoS₂ Nanowires with Expanded

- Interlayers for Sodium-Ion Batteries with Ultralong Cycle Life, *Small* 16 (2020) 1906607.
- [36] L. Cai, J. He, Q. Liu, T. Yao, L. Chen, W. Yan, F. Hu, Y. Jiang, Y. Zhao, T. Hu, Z. Sun, S. Wei, Vacancy-induced ferromagnetism of MoS₂ nanosheets, *J. Am. Chem. Soc.* 137 (2015) 2622-2627.
- [37] Y. Qu, M. Shao, Y. Shao, M. Yang, J. Xu, C.T. Kwok, X. Shi, Z. Lu, H. Pan, Ultra-high electrocatalytic activity of VS₂ nanoflowers for efficient hydrogen evolution reaction, *J. Mater. Chem. A* 5 (2017) 15080-15086.
- [38] J. Wu, J. Liu, J. Cui, S. Yao, M. Ihsan-Ul-Haq, N. Mubarak, E. Quattrocchi, F. Ciucci, J.-K. Kim, Dual-phase MoS₂ as a high-performance sodium-ion battery anode, *J. Mater. Chem. A* 8 (2020) 2114-2122.
- [39] X. Yue, J. Wang, Z. Xie, A.M. Patil, T. Yu, X. Du, Z. Wang, X. Hao, A. Abudula, G. Guan, Coral reef-like MoS₂ microspheres with 1T/2H phase as high-performance anode material for sodium ion batteries, *J. Mater. Sci.* 55 (2020) 14389-14400.
- [40] Z. Lei, J. Zhan, L. Tang, Y. Zhang, Y. Wang, Recent development of metallic (1T) phase of molybdenum disulfide for energy conversion and storage, *Adv. Energy Mater.* 8 (2018) 1703482.
- [41] C. Guo, J. Pan, H. Li, T. Lin, P. Liu, C. Song, D. Wang, G. Mu, X. Lai, H. Zhang, Observation of superconductivity in 1T'-MoS₂ nanosheets, *J. Mater. Chem. C* 5 (2017) 10855-10860.

- [42] P. Li, Y. Yang, S. Gong, F. Lv, W. Wang, Y. Li, M. Luo, Y. Xing, Q. Wang, S. Guo, Co-doped 1T-MoS₂ nanosheets embedded in N, S-doped carbon nanobowls for high-rate and ultra-stable sodium-ion batteries, *Nano Res.* 12 (2018) 2218-2223.
- [43] X. Chia, A. Ambrosi, P. Lazar, Z. Sofer, M. Pumera, Electrocatalysis of layered group 5 metallic transition metal dichalcogenides (MX₂, M = V, Nb, and Ta; X = S, Se, and Te), *J. Mater. Chem. A* 4 (2016) 14241-14253.
- [44] J. Zhang, C. Zhang, Z. Wang, J. Zhu, Z. Wen, X. Zhao, X. Zhang, J. Xu, Z. Lu, Synergistic interlayer and defect engineering in VS₂ Nanosheets toward efficient electrocatalytic hydrogen evolution reaction, *Small* 14 (2018) 1703098.
- [45] X. Xue, R. Chen, C. Yan, P. Zhao, Y. Hu, W. Kong, H. Lin, L. Wang, Z. Jin, One-step synthesis of 2-ethylhexylamine pillared vanadium disulfide nanoflowers with ultralarge interlayer spacing for high-performance magnesium storage, *Adv. Energy Mater.* 9 (2019) 1900145.
- [46] M. Naguib, J. Halim, J. Lu, K.M. Cook, L. Hultman, Y. Gogotsi, M.W. Barsoum, New two-dimensional niobium and vanadium carbides as promising materials for Li-ion batteries, *J. Am. Chem. Soc.* 135 (2013) 15966-15969.
- [47] Y. Dong, Z. Zhu, Y. Hu, G. He, Y. Sun, Q. Cheng, I.P. Parkin, H. Jiang, Supersaturated bridge-sulfur and vanadium co-doped MoS₂ nanosheet arrays with enhanced sodium storage capability, *Nano Res.* (2020) 1-7.
- [48] F. Luo, X. Feng, L. Zeng, L. Lin, X. Li, B. Kang, L. Xiao, Q. Chen, M. Wei, Q. Qian, In situ simultaneous encapsulation of defective MoS₂ nanolayers and sulfur

nanodots into SPAN fibers for high rate sodium-ion batteries, *Chem. Eng. J.* 404 (2021) 126430.

[49] L.G. Bulusheva, V.O. Koroteev, S.G. Stolyarova, A.L. Chuvilin, P.E. Plyusnin, Y.V. Shubin, O.Y. Vilkov, X. Chen, H. Song, A.V. Okotrub, Effect of in-plane size of MoS₂ nanoparticles grown over multilayer graphene on the electrochemical performance of anodes in Li-ion batteries, *Electrochim. Acta* 283 (2018) 45-53.

[50] Z. Hu, Q. Liu, S.L. Chou, S.X. Dou, Advances and challenges in metal sulfides/selenides for next-generation rechargeable sodium-ion batteries, *Adv. Mater.* 29 (2017) 1700606.

[51] Z. Hu, K. Zhang, Z. Zhu, Z. Tao, J. Chen, FeS₂ microspheres with an ether-based electrolyte for high-performance rechargeable lithium batteries, *J. Mater. Chem. A* 3 (2015) 12898-12904.

[52] K. Li, J. Zhang, D. Lin, D.W. Wang, B. Li, W. Lv, S. Sun, Y.B. He, F. Kang, Q.H. Yang, L. Zhou, T.Y. Zhang, Evolution of the electrochemical interface in sodium ion batteries with ether electrolytes, *Nat. Commun.* 10 (2019) 725.

[53] M. Chen, Z. Zhang, L. Si, R. Wang, J. Cai, Engineering of yolk-double shell cube-like SnS@N-S codoped carbon as a high-performance anode for Li- and Na-ion batteries, *ACS Appl. Mater. Inter.* 11 (2019) 35050-35059.

[54] J. Bai, B. Zhao, X. Wang, H. Ma, K. Li, Z. Fang, H. Li, J. Dai, X. Zhu, Y. Sun, Yarn ball-like MoS₂ nanospheres coated by nitrogen-doped carbon for enhanced lithium and sodium storage performance, *J. Power Sources* 465 (2020) 228282.

- [55] M. Feng, M. Zhang, H. Zhang, X. Liu, H. Feng, Room-temperature carbon coating on MoS₂/Graphene hybrids with carbon dioxide for enhanced sodium storage, *Carbon* 153 (2019) 217-224.
- [56] J. Guo, X. Sun, K. Shen, X. Li, N. Zhang, T. Hou, A. Fan, S. Jin, X. Hu, T. Li, R. Ling, S. Cai, C. Zheng, Controllable synthesis of tunable few-layered MoS₂ chemically bonding with in situ conversion nitrogen-doped carbon for ultrafast reversible sodium and potassium storage, *Chem. Eng. J.* 393 (2020) 124703.
- [57] L. Wang, G. Yang, J. Wang, S. Peng, W. Yan, S. Ramakrishna, Controllable design of MoS₂ nanosheets grown on nitrogen-doped branched TiO₂/C nanofibers: toward enhanced sodium storage performance induced by pseudocapacitance behavior, *Small* 16 (2020) 1904589.
- [58] Y. Wang, K. Wang, C. Zhang, J. Zhu, J. Xu, T. Liu, Solvent-exchange strategy toward aqueous dispersible MoS₂ nanosheets and their nitrogen-rich carbon sphere nanocomposites for efficient lithium/sodium ion storage, *Small* 15 (2019) 1903816.
- [59] W. Zhang, H. Zhou, Z. Huang, S. Li, C. Wang, H. Li, Z. Yan, T. Hou, Y. Kuang, 3D hierarchical microspheres constructed by ultrathin MoS₂-C nanosheets as high-performance anode material for sodium-ion batteries, *J. Energy Chem.* 49 (2020) 307-315.
- [60] X. Zhang, K. Liu, S. Zhang, F. Miao, W. Xiao, Y. Shen, P. Zhang, Z. Wang, G. Shao, Enabling remarkable cycling performance of high-loading MoS₂@graphene anode for sodium ion batteries with tunable cut-off voltage, *J. Power Sources* 458 (2020) 228040.

- [61] J. Wang, J. Polleux, J. Lim, B. Dunn, Pseudocapacitive contributions to electrochemical energy storage in TiO₂ (anatase) nanoparticles, *J. Phys. Chem. C* 111 (2007) 14925-14931.
- [62] T. Brezesinski, J. Wang, S.H. Tolbert, B. Dunn, Ordered mesoporous alpha-MoO₃ with iso-oriented nanocrystalline walls for thin-film pseudocapacitors, *Nat. Mater.* 9 (2010) 146-151.
- [63] D. Chao, C. Zhu, P. Yang, X. Xia, J. Liu, J. Wang, X. Fan, S.V. Savirov, J. Lin, H.J. Fan, Z.X. Shen, Array of nanosheets render ultrafast and high-capacity Na-ion storage by tunable pseudocapacitance, *Nat. Commun.* 7 (2016) 12122.
- [64] H. Lim, H. Kim, S.-O. Kim, W. Choi, Self-assembled N-doped MoS₂/carbon spheres by naturally occurring acid-catalyzed reaction for improved sodium-ion batteries, *Chem. Eng. J.* 387 (2020) 124144.
- [65] W. Wang, B. Jiang, C. Qian, F. Lv, J. Feng, J. Zhou, K. Wang, C. Yang, Y. Yang, S. Guo, Pistachio-shuck-like MoSe₂/C core/shell nanostructures for high-performance potassium-ion storage, *Adv. Mater.* 30 (2018) 1801812.
- [66] N. Feng, R. Meng, L. Zu, Y. Feng, C. Peng, J. Huang, G. Liu, B. Chen, J. Yang, A polymer-direct-intercalation strategy for MoS₂/carbon-derived hetero-aerogels with ultrahigh pseudocapacitance, *Nat. Commun.* 10 (2019) 1372.
- [67] W. Ren, H. Zhang, C. Guan, C. Cheng, Ultrathin MoS₂ nanosheets@metal organic framework-derived N-doped carbon nanowall arrays as sodium ion battery anode with superior cycling life and rate capability, *Adv. Funct. Mater.* 27 (2017) 1702116.

- [68] C. Zhao, C. Yu, M. Zhang, Q. Sun, S. Li, M. Norouzi Banis, X. Han, Q. Dong, J. Yang, G. Wang, X. Sun, J. Qiu, Enhanced sodium storage capability enabled by super wide-interlayer-spacing MoS₂ integrated on carbon fibers, *Nano Energy* 41 (2017) 66-74.
- [69] G. Wang, X. Bi, H. Yue, R. Jin, Q. Wang, S. Gao, J. Lu, Sacrificial template synthesis of hollow C@MoS₂@PPy nanocomposites as anodes for enhanced sodium storage performance, *Nano Energy* 60 (2019) 362-370.
- [70] W.Y. Zhou, S.S. Li, X.Y. Xiao, S.H. Chen, J.H. Liu, X.J. Huang, Defect-and phase-engineering of Mn-mediated MoS₂ nanosheets for ultrahigh electrochemical sensing of heavy metal ions: chemical interaction-driven in situ catalytic redox reactions, *Chem. Commun.* 54 (2018) 9329-9332.
- [71] S. Liu, Y. Yin, M. Wu, K.S. Hui, K.N. Hui, C.Y. Ouyang, S.C. Jun, Phosphorus-mediated MoS₂ nanowires as a high-performance electrode material for quasi-solid-state sodium-ion intercalation supercapacitors, *Small* 15 (2019) 1803984.
- [72] Y. Li, K. Chang, E. Shanguan, D. Guo, W. Zhou, Y. Hou, H. Tang, B. Li, Z. Chang, Powder exfoliated MoS₂ nanosheets with highly monolayer-rich structures as high-performance lithium-/sodium-ion-battery electrodes, *Nanoscale* 11 (2019) 1887-1900.

CHAPTER 5 Controllable synthesis of novel orderly layered VMoS₂ anode materials with super electrochemical performance for sodium ion batteries

5.1 Introduction

Recently, sodium ion batteries (SIBs) have been widely considered to be the possible alternatives of lithium ion batteries (LIBs) in field of energy storage owing to the rich sodium resource in the world[1-4]. However, compared with Li⁺, Na⁺ with a larger radius is not conducive to the intercalation between graphite layers of commercial graphite based anodes [5, 6]. To date, it is still full of challenges to develop suitable anode materials with excellent electrochemical performance for the SIBs. Carbon material[7], metal oxide[8], metal sulfide[9], and alloy[10] based anodes have been developed and applied in the SIBs. Typically, MoS₂, as a kind of layered metal sulfide, has drawn numerous attentions since it has larger interlayer spacing as well as higher theoretical capacity [11, 12]. Unfortunately, the pure MoS₂ has poor electrical conductivity, slow reaction kinetics and large volume change in the process of intercalation/deintercalation, resulting in short cycling life and low rate capacity [13, 14], which need to be conquered.

To solve the above issues, various strategies such as nanostructure designing, electrolyte selecting, voltage range cutting off, and electrode materials searching have been adopted[15-22]. By using these strategies, increased Na⁺ storage sites, shortened pathway for Na⁺ transmission, enhanced conductivity, and/or buffered volume

expansion could be realized. For instance, Ye *et al.* [23] synthesized MoS₂ anode material with mixed phases for SIBs, which showed specific capacities of 200 mA h g⁻¹ @ 0.1 A g⁻¹ and 154 mA h g⁻¹ @ 1 A g⁻¹ in a 0.4-3 V voltage range, respectively. Even though it displayed a good cycling stability, the reversible capacity was still low so that it could not meet the demand of application. Wang *et al.* [24] fabricated a C@MoS₂@polypyrrole (PPy) anode material, which showed a remarkable specific capacity of 713 mA h g⁻¹ @ 0.1 A g⁻¹ and excellent cyclability with a specific capacity of 295 mA h g⁻¹ @ 5 A g⁻¹ in 500 cycles. However, the fabrication process was too complex so that this anode was not suitable for the commercial SIBs. Therefore, fabrication of suitable anode materials with remarkable property for SIBs via facile methods is still necessary.

Herein, a novel orderly layered VMoS₂ (OL-VMS) material was synthesized through a simple self-assembly hydrothermal approach followed with a calcination treatment process. This material had an interesting nanostructure with stacked nanosheets, which could offer abundant storage sites for Na⁺, vertical paths to promote the Na⁺ diffusion, and a stable framework to buff the volume change during the intercalation/deintercalation of Na⁺. As it was used as the anode material, a remarkable specific capacity of 602.9 mAh g⁻¹ was obtained at 0.200 A g⁻¹. Furthermore, after 190 cycles at 2 A g⁻¹, the OL-VMS based anode still exhibited an outstanding specific capacity of 534.1 mAh g⁻¹. In addition, under the condition of large current density of 5 A g⁻¹, a specific capacity of 452.8 mAh g⁻¹ was achieved.

5.2 Experimental

5.2.1 Synthesis of OL-VMS

The OL-VMS material was simply synthesized as follows. Firstly, 0.234 g of NH_4VO_3 and 0.3629 g of $\text{Na}_2\text{MoO}_4 \cdot \text{H}_2\text{O}$ were dissolved in 30 ml of distilled water with 0.25 ml ammonia solution with ultrasonic treatment. Secondly, 2.4g of $\text{C}_2\text{H}_5\text{NS}$ (TAA) was added into the above solution and vigorously stirred for 30 min. Then, the obtained homogeneous suspension was transferred into a 50 ml Teflon-lined sealed autoclave, which was placed at an oven with a temperature of 220 °C for 24 h. After cooling down to room temperature, the black product was collected by centrifugation and successively washed with distilled water and ethanol for several times, and then dried at 60 °C in a vacuum oven for 12 h. Finally, the product was calcined at 300 °C for 1 h in argon atmosphere. For comparison, the OL-VMS materials synthesized with different amounts of ammonia solution and reaction periods were also obtained using the same process.

5.2.2 Characterizations

Scanning electron microscope (SEM, SU8010, Hitachi, Japan) with an energy dispersive spectrometer (EDS, Horiba, Japan) was used for characterizing the morphology and elemental distribution at an operation voltage of 15.0 kV. While, high-resolution transmission electron microscope (HRTEM) image was obtained on a JEM-2100F TEM with an accelerating voltage of 200 kV. X-ray diffraction (XRD) analysis was carried out by an X-ray diffractometer (XRD, Smartlab 9kW, Rigaku, Japan) with

a CuK α X-ray source ($\lambda=1.5418 \text{ \AA}$). The X-ray photoelectron spectrum (XPS) was determined on a VG ESCALAB 250 spectrometer (Thermo Electron, UK) using an Al K α X-ray source (1486 eV). Raman spectrum was recorded with a Renishaw inVia Raman spectrometer using an excitation wavelength of 532 nm.

5.2.3 Electrochemical measurements

To prepare working electrode, 75 wt % of the synthesized OL-VMS material, 15 wt% of super p and 10 wt% of polyvinylidene fluoride (PVDF) were mixed together in N-methyl pyrrolidone (NMP) to form a slurry at first. Then, the obtained slurry was pasted onto a copper foil and dried in a vacuum oven at 80 °C overnight. The amount of OL-VMS material coated on the copper foil was calculated to be $\sim 0.9 \text{ mg cm}^{-2}$ for each electrode. For comparison, the working electrode with a loading amount of $\sim 2 \text{ mg cm}^{-2}$ without super p was also prepared through the same process (OL-VMS material : PVDF = 95 wt% : 5 wt%). The electrolyte was 1 M sodium trifluoromethanesulfonate (NaCF $_3$ SO $_3$) in diglyme (DGM). 2032-type coin cell used in this study was assembled in an argon-filled glove box, in which sodium metal foil and Whatman GF/F were used as the counter electrode and separator, respectively. Galvanostatic charge/discharge measurements were recorded by a battery testing system (LAND CT2001A model, Wuhan LAND Electronic. Ltd) with different voltage ranges of 0.3-3 V, 0.2-3 V, 0.1-3 V, and 0.01-3 V. Cyclic voltammograph (CV) measurement was performed on an electrochemistry workstation at a scan rate of 0.1 mV s^{-1} . Electrochemical impedance spectrum (EIS) was recorded over a frequency range of 0.01 Hz-100 kHz.

5.3 Results and discussion

5.3.1 Characterizations

To explore the formation of OL-VMS with the special structure, the OL-VMS synthesis with different amounts of ammonia solutions were carried out. Figure 5.1 shows SEM images of different OL-VMS samples prepared with different amounts of ammonia solutions, i.e., 0, 0.5, 1 and 2 ml. In the absence of ammonia solution, a flower-like morphology was obtained (Figure 5.1 a and b). When 0.25 ml of ammonia solution was added, the layered orderly arrangement structure formed by stacked nanosheets with a diameter of 200 nm was clearly observed in 24 h (Figures 5.2a and b). With the increasing of ammonia solution amount, the morphology of the orderly layered structure became more and more ununiform (Figures 5.1 c-h). For example, as the added ammonia solution was increased to 1 and 2 ml, the nanosheets with a larger diameter of ~500 nm coexisted with those nanosheets with a diameter of 200 nm (Figures 5.1 e and g). Thus, controllably addition of appropriate ammonia solution amount should be conducive to the formation of more orderly layered structure.

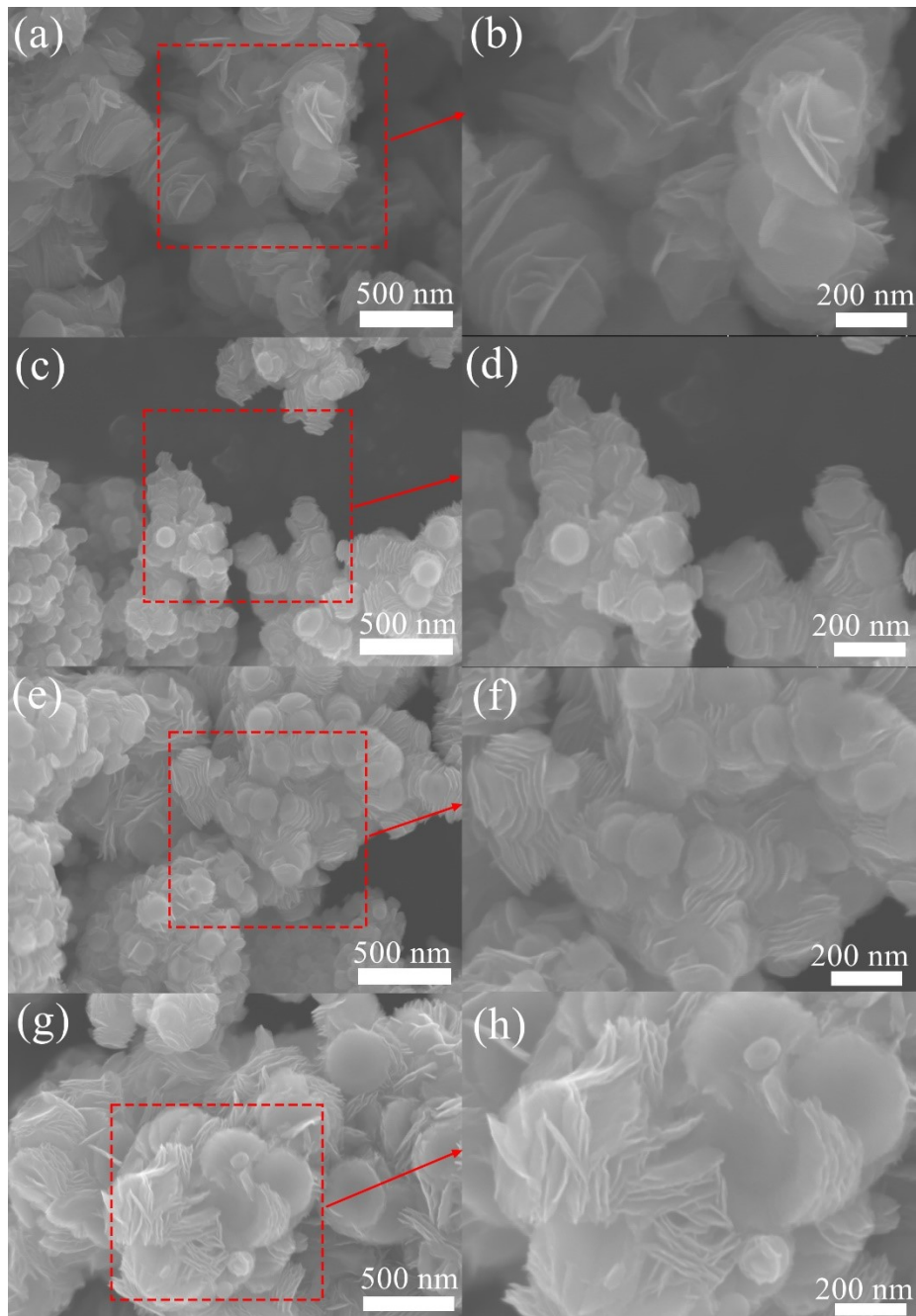


Figure 5.1 SEM images of OL-VMS synthesized with different amount of ammonia solution: (a and b) 0 ml, (c and d) 0.5 ml, (e and f) 0.1 ml, and (g and h) 2 ml.

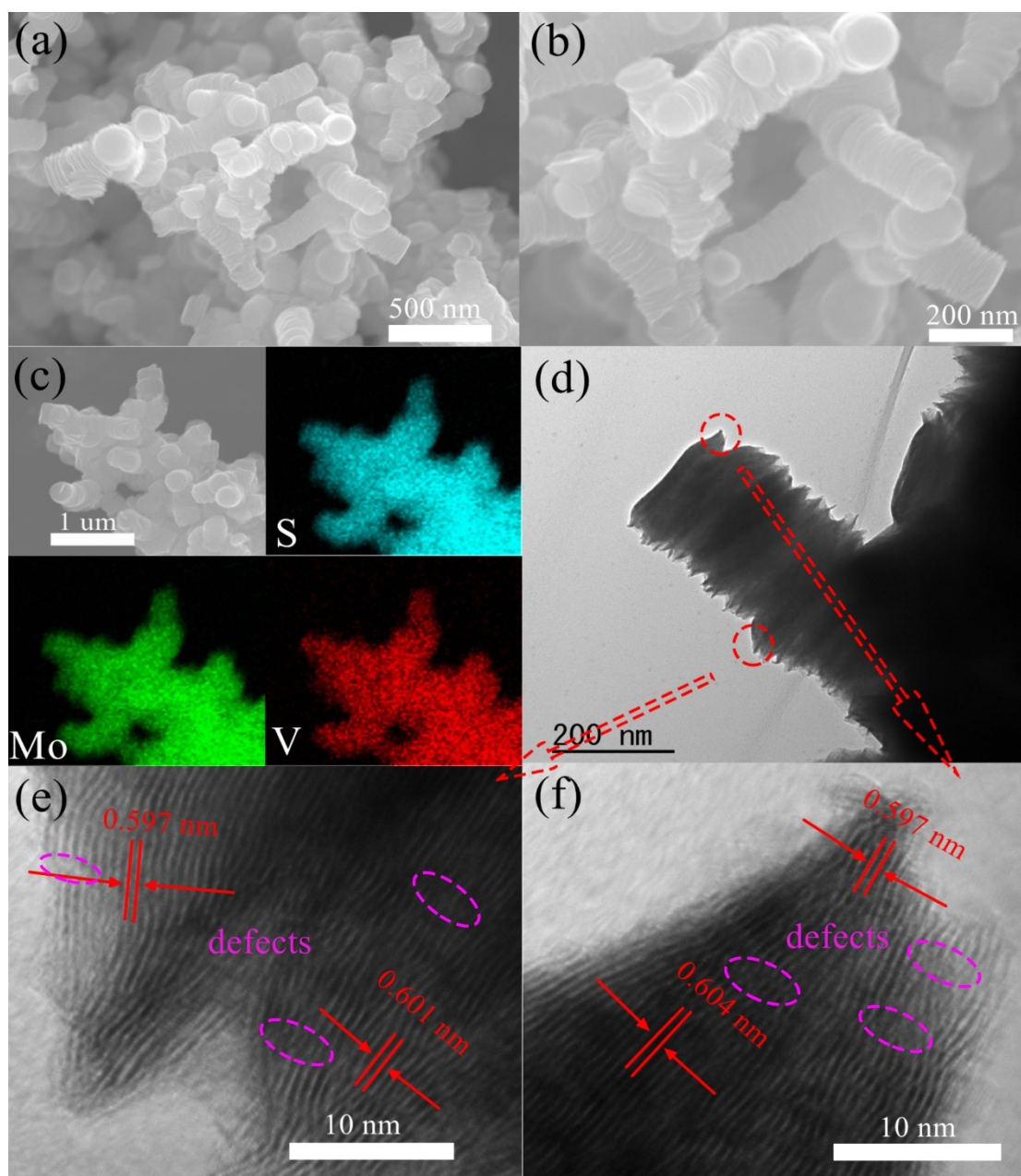


Figure 5.2 (a and b) SEM images of OL-VMS, (c) EDS elemental mappings of S, Mo, and V, (d) TEM and (e and f) HRTEM images of OL-VMS.

While, Figure 5.3 shows SEM images of OL-VMS samples synthesized with different hydrothermal synthesis time. One can see that the orderly layered structure with a short length was formed in the first 3 h (Figures 5.3 a and b). In addition, the single-layer nanosheet was also observed in this stage (Figure 5.3b), indicating that the

single-layer nanosheet should be firstly formed at the beginning stage of reaction. Then, with the increasing of hydrothermal synthesis time from 3 to 18 h, the length of the pillar with the orderly layered structure became longer and longer gradually (Figures 5.3 c-h). In the following sections, the OL-VMS prepared with 0.25 ml NH_4OH and 24 h reaction will be mainly characterized and discussed since it showed the best performance in the preliminary experiments. Based on these SEM observations, the formation mechanism of OL-VMS with layered orderly arrangement structure could be illustrated in Figure 5.4. Herein, due to the lowest energy of 002 plane of MoS_2 crystal, the MoS_2 nanosheet could be formed along the 002 plane during the hydrothermal process at first. Then, the NH_4^+ from NH_4OH in solution would absorb on the surface of the formed nanosheet so that the nanosheet was positively charged. As such, MoO_4^{2-} and VO_3^- anions in the solution were also adsorbed on the positively charged nanosheet surface through electrostatic interaction. Thereafter, the anions could be reduced by TAA to form the other VMS nanosheet, which would be stacked together with the first VMoS_2 nanosheet. This nanosheet stacking process should be proceeded continuously during the hydrothermal synthesis as the reaction time increases. Finally, the orderly layered structure was obtained as shown in Figures 5.2a and b. Figure 5.2c shows EDS elemental mappings of various elements on the surface of obtained OL-VMS sample. Obviously, the elements of Mo, S and V were uniformly distributed.

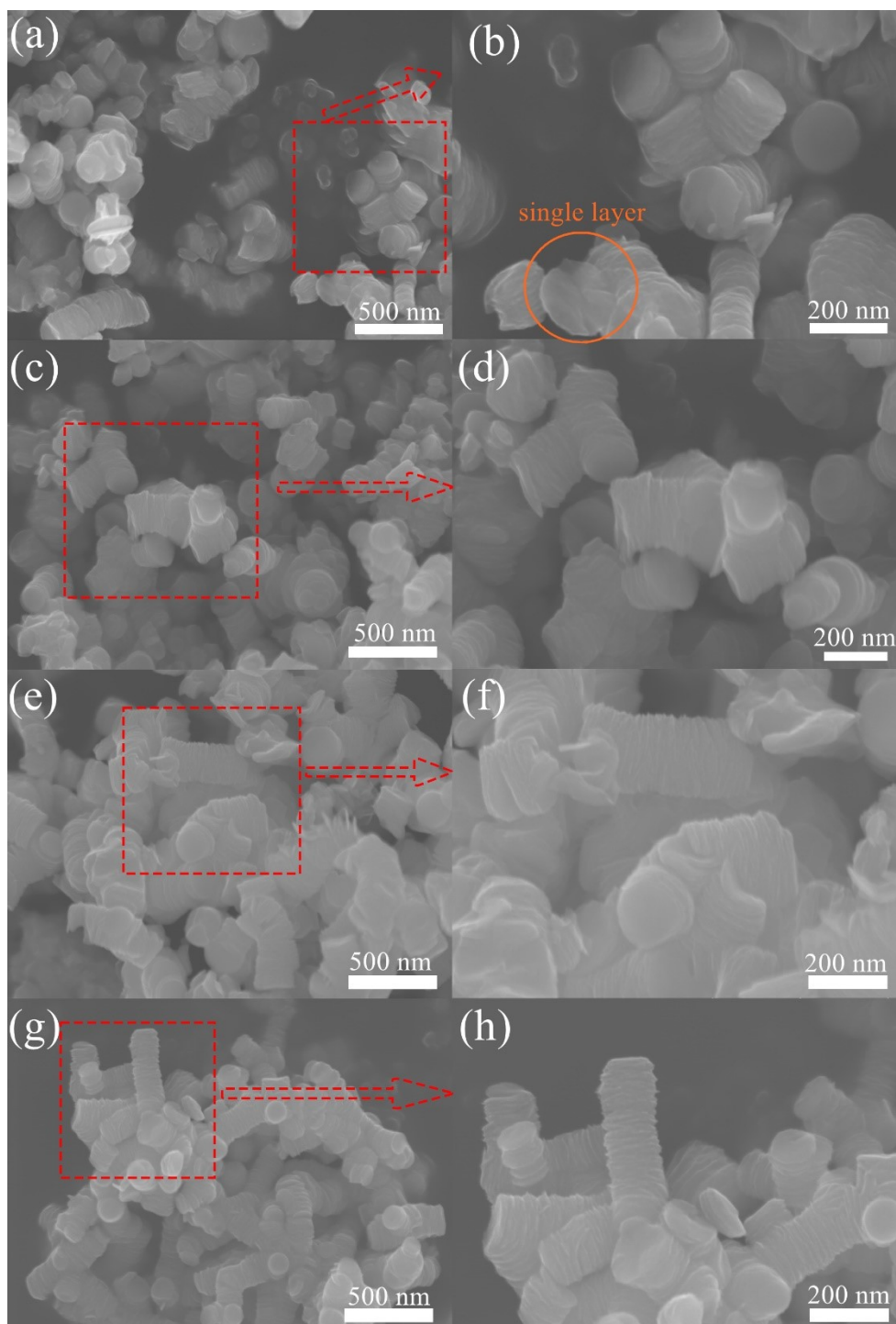


Figure 5.3 SEM images of OL-VMS samples prepared with different hydrothermal synthesis time: (a and b) 3 h, (c and d) 6 h, (e and f) 12 h, and (g and h) 18 h.

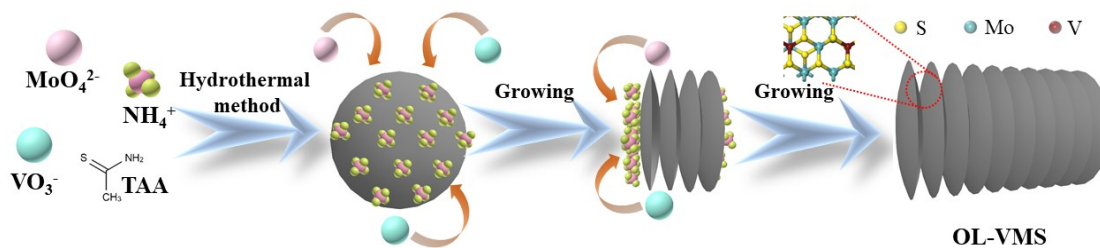


Figure 5.4 Schematic illustration of the OL-VMS fabrication procedure.

The nanostructure of OL-VMS was further observed by TEM measurement. From Figure 5.2d, it was obviously seen that the orderly layered structure with a diameter of 200 nm was consistent with the SEM observation (Figures 5.2a and b). Figures 5.2e and f present HRTEM images at different parts. It was clearly seen that a smaller interlayer spacing of ~ 0.6 nm was observed when compared with that of pure MoS_2 (0.615 nm). The smaller interlayer spacing in the OL-VMS could be resulted from the replacing of Mo atom in the framework of MoS_2 by the V atom. In addition, after the addition of V species, the (002) plane of MoS_2 became chaotic and discontinuous, resulting in more defects in the OL-VMS sample (Figures 5.2e and f), which could offer abundant Na^+ storage sites.

Figure 5.5a displays the typical XRD spectra of the obtained OL-VMS samples, in which four main peaks located at $2\theta=14.56^\circ$, 33.07° , 39.51° , and 58.29° are attributed to the (002), (100), (103) and (110) planes of 2H- MoS_2 (JCPDS No. 37-1492), separately [25]. It should be noted that no peaks relating to the impurities were found, indicating that the pure phase OL-VMS was obtained. Moreover, the position of peak corresponding to the (002) plane was just located in between (002) plane peak of MoS_2

and (001) plane peak of VS_2 , revealing that the interlayer spacing of OL-VMS should be larger than that of VS_2 but smaller than that of MoS_2 . In addition, based on Bragg's Law, the calculated distance between interlayers was 0.6 nm, which was consistent with the HRTEM observation (Figures 5.2e and f). Notably, the characteristic peaks of VS_2 were not detected from Figure 5.5a, indicating the formation of new phase due to the incorporating of vanadium into the nanostructure of MoS_2 . As indicated above, it caused smaller interlayer spacing.

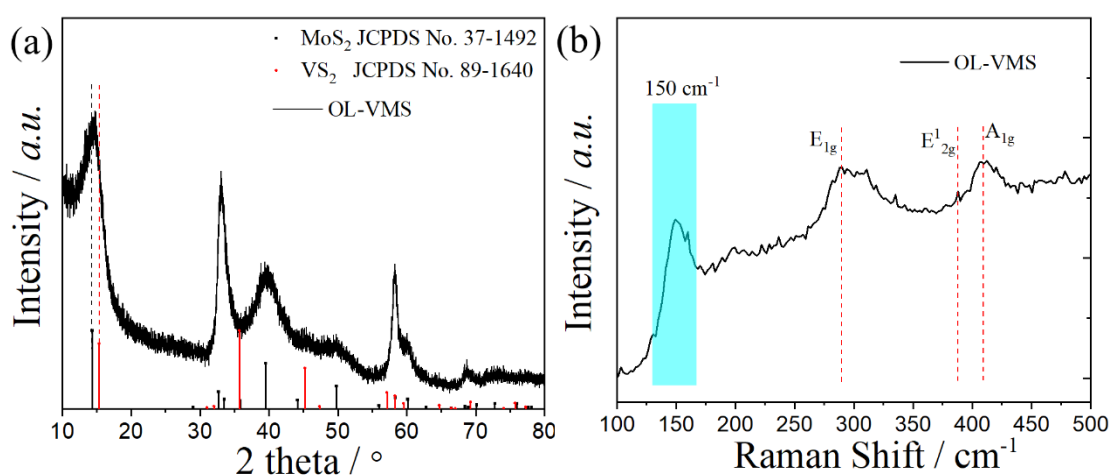


Figure 5.5 (a) XRD pattern and (b) Raman spectrum of OL-VMS sample.

Figure 5.6 shows XRD spectra of those OL-VMS samples prepared at different conditions. One can see that all XRD spectra were similar, revealing that they had the same crystalline structure. In order to further verify the nanostructure of OL-VMS sample, Raman spectrum analysis was also measured. Since the Raman spectrum of MoS_2 is almost the same as that of VS_2 [26-28], as shown in Figure 5.5b, three peaks appeared at ~ 290 , 388 , and 410 cm^{-1} corresponded to E_{1g} , E_{2g}^1 , and A_{1g} modes of MoS_2 as well as VS_2 , respectively. In particular, the peak observed at $\sim 150 \text{ cm}^{-1}$ indicated the presence of V-S bonds in the framework of MoS_2 [29, 30], which was consistent with

the above XRD result. Moreover, since the previous works have certificated that the positions of 1T phase of MoS₂ and VS₂ in Raman were similar [26,31], the 1T and 2H phase should coexist in the structure of OL-VMS.

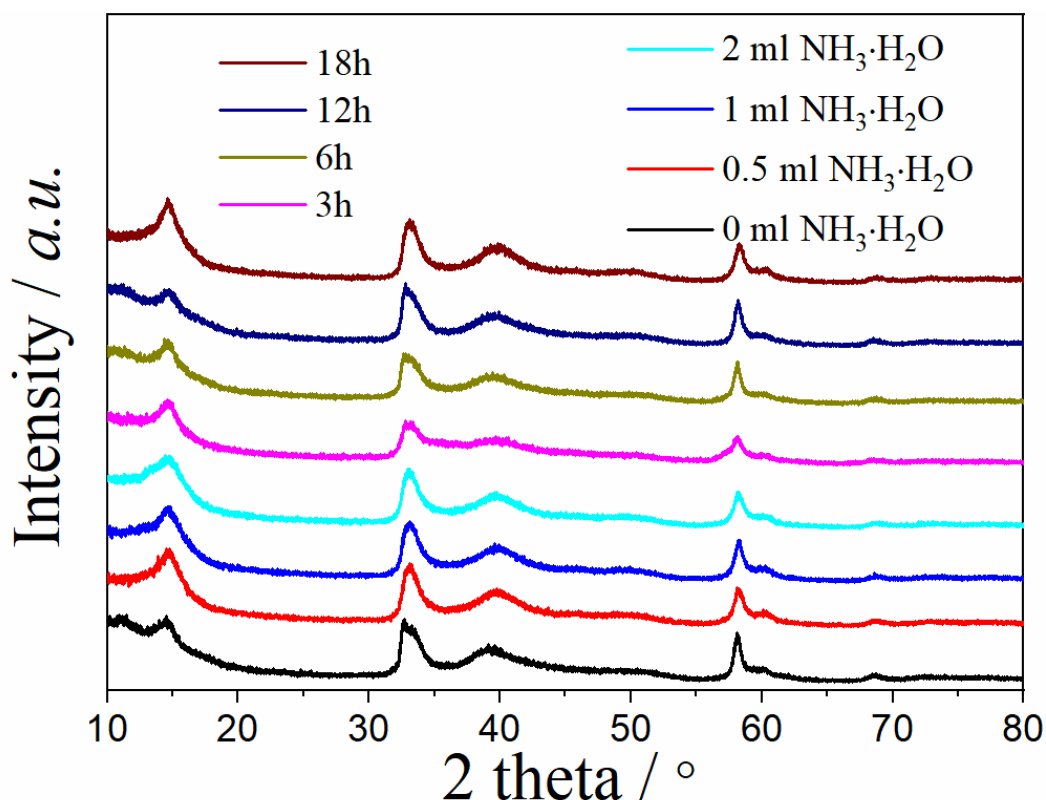


Figure 5.6 XRD patterns of OL-VMS samples prepared at different conditions.

Figure 5.7 displays the XPS survey spectrum and high-resolution XPS spectra of Mo 3d, V 2p, and S 2p for the OL-VMS. The peaks corresponding to V, Mo, and S were clearly observed (Figure 5.7a), indicating the co-existing of S, Mo and V species in the framework of obtained OL-VMS sample. In high-resolution XPS spectrum of Mo 3d (Figure 5.7b), four peaks were observed. Among them, two strong peaks located at 228.4 eV and 231.5 eV were ascribed to Mo⁴⁺ 3d_{5/2} and Mo⁴⁺ 3d_{3/2}, respectively [31]. While, the small peaks appeared at 235.8 eV and 225.9 assigned to Mo⁶⁺ and S 2s,

respectively. Herein, the presence of Mo^{6+} should be produced by the oxidation process on the surface of MoS_2 [32]. For V 2p, four peaks at 513.3, 521.0, 517.5 and 524.8 eV corresponding to $\text{V}^{2+} 2p_{3/2}$, $\text{V}^{2+} 2p_{1/2}$, $\text{V}^{4+} 2p_{3/2}$ and $\text{V}^{4+} 2p_{1/2}$, respectively, were observed (Figure 5.7c). Herein, the formation of V^{2+} should be resulted from the strong reducibility of S^{2-} [33], which was produced from the decomposition of TAA at high temperature. The high-resolution XPS spectrum of S 2p was consisted of four peaks located at 164.1, 162.8, 161.7 and 161.0 eV, respectively (Figure 5.7d), in which the two peaks in the low binding energy were attributed to $\text{S}^{2-} 2p_{1/2}$ and $\text{S}^{2-} 2p_{3/2}$, separately [34]. While, in the high binding energy, there were two peaks corresponding to S^0 , S^{2-}_2 , which should be produced by the decomposition of excessive TAA in the process of synthesis [35, 36]. Combining these XPS analysis results with the above HRTEM, XRD and Raman analyses, it revealed that some parts of molybdenum in nanostructure of MoS_2 should be replaced by vanadium, leading to the formation of VMoS_2 .

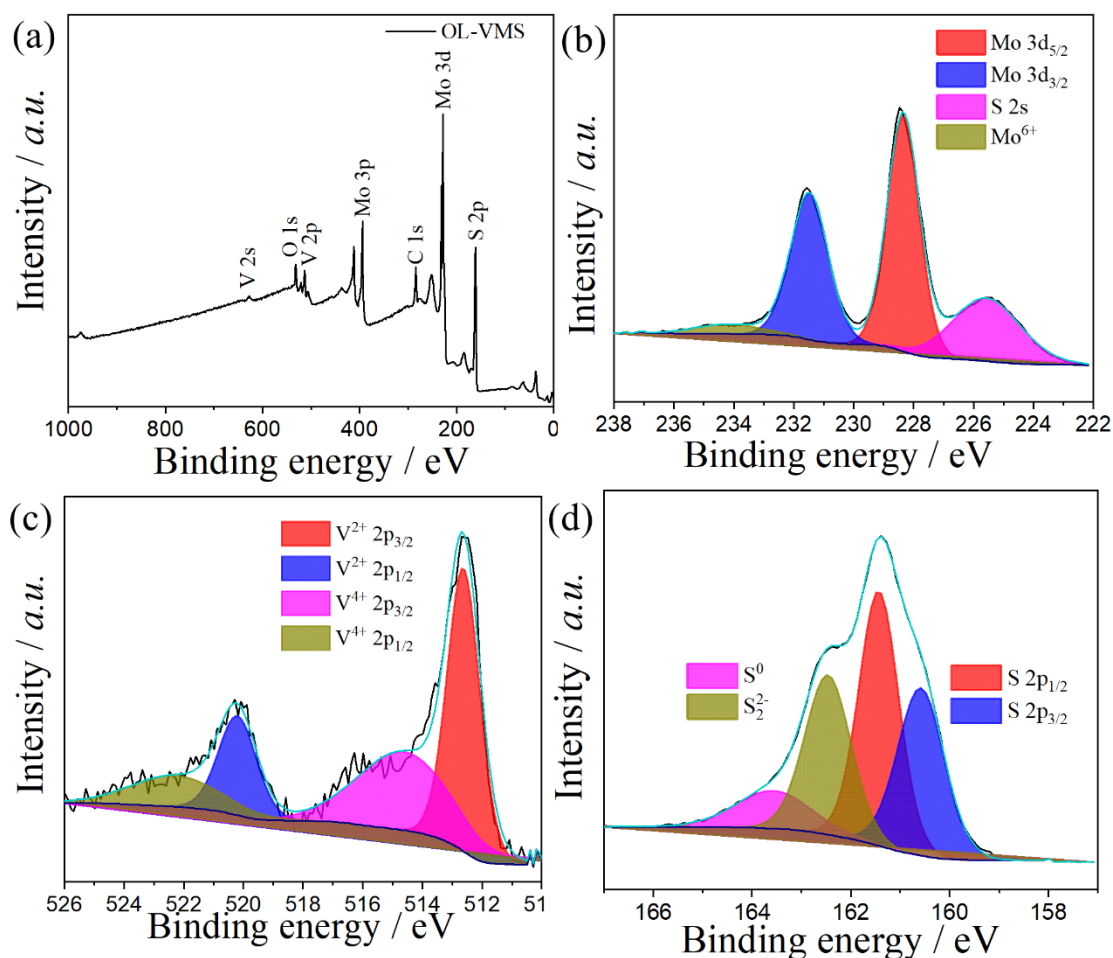


Figure 5.7 (a) XPS survey spectrum of OL-VMS; High-resolution (b) Mo 3d, (c) V 2p and (d) S 2p spectra of OL-VMS.

5.3.2 Electrochemical performance

The CVs of the OL-VMS based anodes were collected under the condition of 0.1 mV s^{-1} within a voltage range of 0.1-3 V. Figure 5.8a displays the first three cycles of CVs for the OL-VMS based anode, in which four cathodic peaks at 2.3, 1.9, 1.37, 0.3 V as well as two anodic peaks at 2.22 and 1.55 V appeared. Herein, the cathodic peaks at 2.3, 1.9 and 1.37 V could be assigned to the intercalation process between the interlayers while the last peak of 0.3 V corresponded to the formation of Na_2S with metal Mo and V during the conversion process. Herein, the intensity of cathodic peak

located at 0.3 V disappeared and the CV curve maintained almost unchanged after the first cycle (Figure 5.8a), which could be assigned to stable solid electrolyte interphase (SEI) layer produced by the ether-based electrolyte after the first cycle. Meanwhile, the peaks at 1.55 and 2.22 V in the first anodic scan should be assigned to either the formation of MoS₂ during conversion process or the deintercalation of Na⁺ from the interlayers.

Figure 5.8b shows the galvanostatic charging-discharging curves of 1st, 2nd and 5th cycle for OL-VMS based anode, which were tested at 0.2 A g⁻¹ within voltages ranged from 0.1 to 3 V. Herein, high specific capacities of 791.8 and 646.4 mAh g⁻¹ for the first cycle with a high initial Coulombic efficiency (CE) of 81.6% were obtained. Subsequently, after 5 cycles, the specific capacity was 602.9 mAh g⁻¹ with a CE of ~100%. Herein, the electrolyte with ether solvent could produce a stable SEI layer on the electrode surface, leading to a high initial CE [37]. The long cycling stability at 2 A g⁻¹ was measured. From Figure 5.8c, it was obviously seen that the anode delivered a stable specific capacity with 534.1 mAh g⁻¹ until 190th cycles. Furthermore, as another evaluation standard, the rate performance for OL-VMS based anode was also

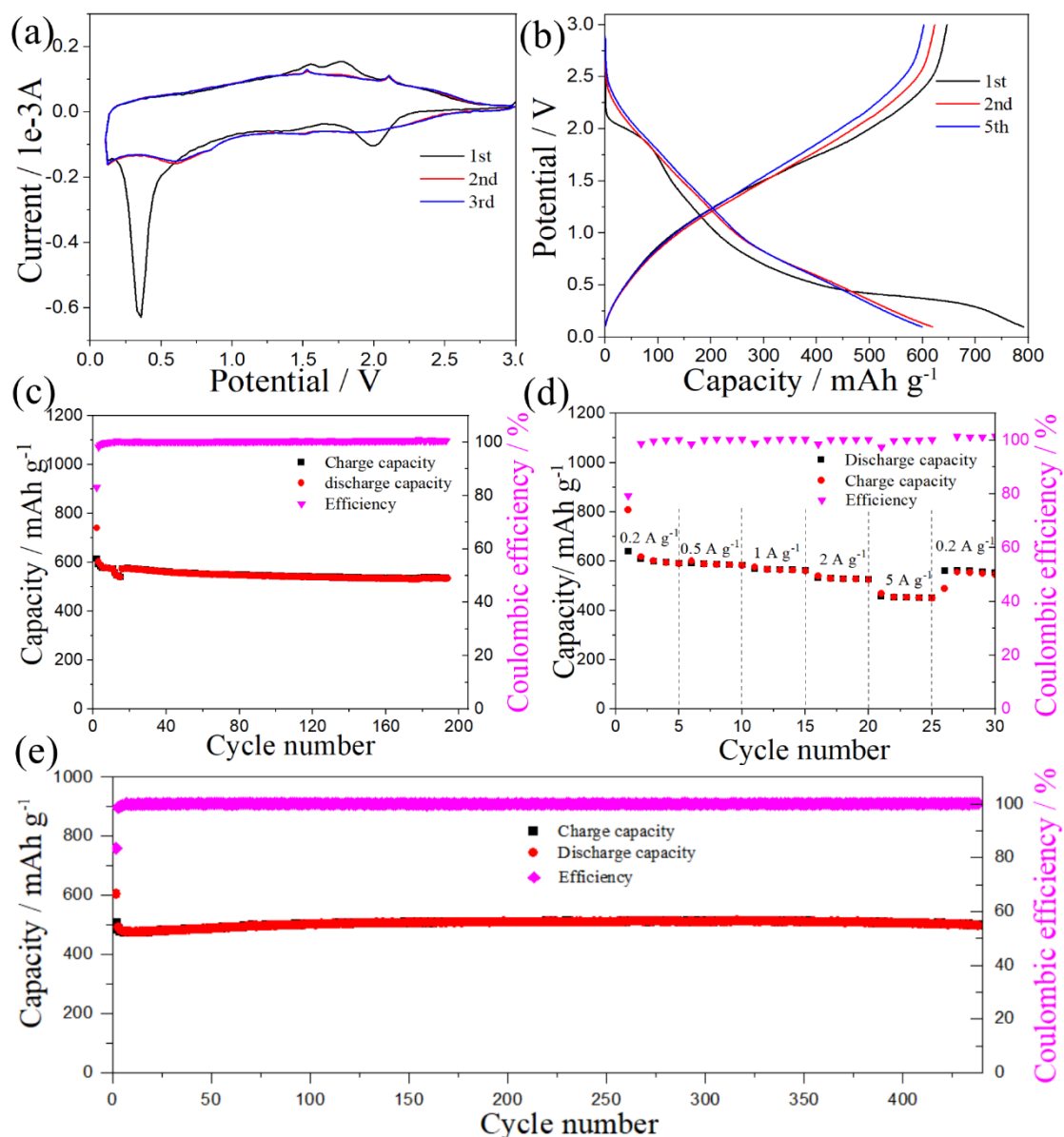


Figure 5.8 (a) Typical CV curves of the OL-VMS based anode in the first three cycles under condition of 0.1 mV s^{-1} within a voltage range from 0.1 to 3 V; (b) Typical galvanostatic charging/discharging curves in the 1st, 2nd, and 5th cycles for the OL-VMS based anode at 0.2 A g^{-1} ; (c) Stability measurement of the OL-VMS based anode at 2 A g^{-1} ; (d) Rate capability of the OL-VMS based anode; (e) Long cyclability of the OL-VMS based electrode at 5 A g^{-1} .

measured. As displayed in Figure 5.8d, the OL-VMS based anode exhibited reversible capacities of 601.4, 586.2, 564.2, 527.7, and 452.8 mAh g⁻¹ at 0.2, 0.5, 1, 2, and 5 A g⁻¹, separately. Furthermore, it was worth noting that the reversible capacity was rebounded to 550 mAh g⁻¹ after the current density was changed to 0.2 A g⁻¹ again. Most importantly, when the cycling stability was tested at 5 A g⁻¹, the OL-VMS-based anode also performed an excellent cycling capacity of 497.5 mAh g⁻¹ with a CE near 100%.

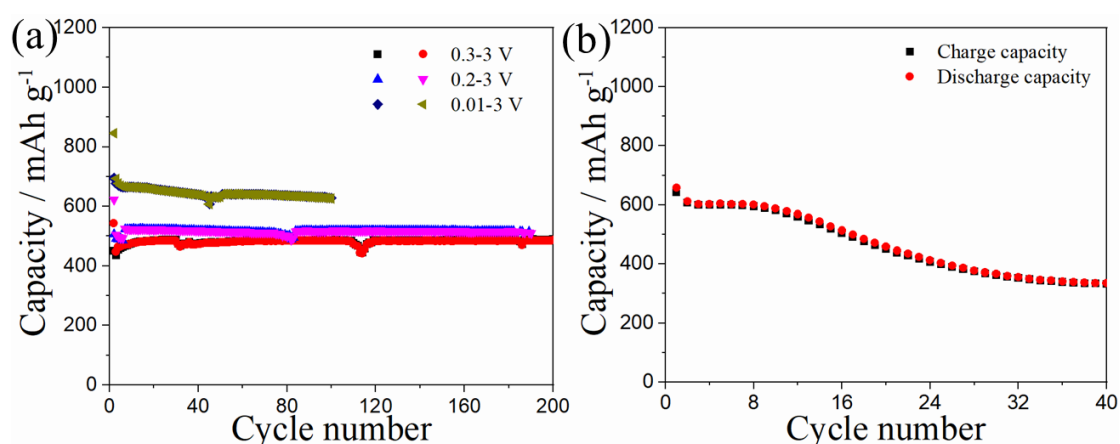


Figure 5.9 (a) Cycling performances of the OL-VMS based anode at a current density of 2 A g⁻¹ in different voltage ranges of 0.3-3, 0.2-3, and 0.01-3V; (b) Cycling performance of the anode with the flower-like sample (prepared without ammonia solution) at a current density of 2 A g⁻¹ in the voltage range of 0.01-3V;

As shown in Figure 5.9a, the cycling stabilities under different voltage ranges of 0.3-3, 0.2-3 and 0.01-3 V were also conducted at 2 A g⁻¹. After 200 cycles, the stable reversible capacities of 511 and 487 mA g⁻¹ were achieved under the voltage condition of 0.3-3V and 0.2-3 V, respectively. Interestingly, even the voltage range was extended to 0.01-3 V, until 100 cycles, the obtained OL-VMS based anode still delivered an outstanding specific capacity of 626.4 mA g⁻¹. In contrast, under a same voltage condition as that on OL-VMS based anode, the cycling life of the anode based on VMS

with the flower-like morphology prepared in the absence of NH_4OH was tested at 2 A g^{-1} . From Figure 5.9b, it was clearly seen that the reversible capacity decreased quickly from 642.4 to 331.7 mA g^{-1} with the increase of cycle, revealing that the anode with the orderly layered structure had better cycling stability when compared with that with the flower-like structure. Herein, the specific orderly layered structure could effectively buff the volume change during the process of discharging/charging.

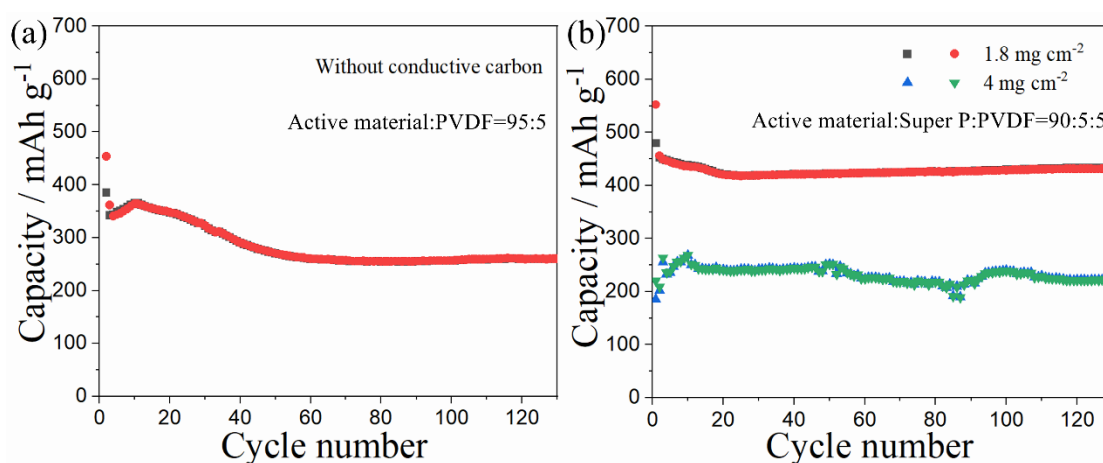


Figure 5.10 Cycling performance of the OL-VMS based anode with (a) in the case without conductive carbon addition and (b) high loading amount at a current density of 1 A g^{-1} in the voltage range of $0.3\text{-}3 \text{ V}$.

Most interestingly, even in the case without the conductive carbon additive (Figure 5.10 a), the OL-VMS based anode with 2 mg cm^{-1} loading amount also exhibited a remarkable specific capacity of 322.6 mA g^{-1} after 30-cycle testing at 1 A g^{-1} . Such a remarkable specific capacity in the absence of conductive carbon could be owing to the improved metal-like conductivity caused by vanadium mediating[38]. In contrast, the stability of electrodes with higher loading amounts of 1.8 and 4 mg cm^{-1} was also measured. As shown in Figure 5.10 b, after 130 cycles, the OL-VMS based anodes with 1.8 and 4 mg cm^{-1} loading amounts exhibited 430.6 and 223.6 mA g^{-1} at 1 A g^{-1} ,

respectively. Table 5.1 compares the electrochemical performance of the present OL-VMS based anode with other VS_2 and MoS_2 based ones. Obviously, compared with most VS_2 and MoS_2 based anodes, this OL-VMS based anode exhibited a higher specific capacity. Thus, such an OL-VMS material should be a potential anode material candidate for the SIBs.

Table 5.1 Comparison of electrochemical performance of the present OL-VMS based anode with the reported MoS₂ and VS₂ based ones.

Electrode	Voltage range	Electrolyte	Performance	Reference
MoS ₂ -C rhomboids	hollow 0.4-3 V	1M NaSO ₃ CF ₃ diglyme	in 506 mA h g ⁻¹ at 0.1 A g ⁻¹ 324 mA h g ⁻¹ at 5 A g ⁻¹	[22]
MoS ₂ -G	0.01-3 V	1M NaClO ₄ in EC, DEC, and FEC	606 mA h g ⁻¹ at 0.2 A g ⁻¹ 345 mA h g ⁻¹ at 1.6 A g ⁻¹	[39]
MoS ₂ @graphene	0.01-3 V	1M NaClO ₄ in EC, DEC, and FEC	513 mA h g ⁻¹ at 0.1 A g ⁻¹ 358.4 mA h g ⁻¹ at 5 A g ⁻¹	[40]
Mixed phase MoS ₂ nanowires	0.4-3 V	1M NaClO ₄ in EC, DEC, and FEC	200 mA h g ⁻¹ at 0.1 A g ⁻¹ 113 mA h g ⁻¹ at 5 A g ⁻¹	[23]
Bi ₂ S ₃ / MoS ₂	0.1-3 V	1M NaSO ₃ CF ₃ diglyme	in 558 mA h g ⁻¹ at 0.1 A g ⁻¹ 330.4 mA h g ⁻¹ at 5 A g ⁻¹	[41]
MoS ₂ /NCF-MP	0.005-3 V	1M NaSO ₃ CF ₃ diglyme	in 480 mA h g ⁻¹ at 0.1 A g ⁻¹ 374 mA h g ⁻¹ at 2 A g ⁻¹	[42]
MoS ₂ /SnS	0.1-3 V	1M NaClO ₄ in PC and FEC	750 mA h g ⁻¹ at 0.2 A g ⁻¹ 493 mA h g ⁻¹ at 5 A g ⁻¹	[20]
CNF@VS ₂	0.01-3 V	1M NaClO ₄ in EC, DMC, and EMC	540 mA h g ⁻¹ at 0.2 A g ⁻¹ 365 mA h g ⁻¹ at 5 A g ⁻¹	[43]
Flower-like VS ₂	0.3-3 V	1M NaSO ₃ CF ₃ diglyme	in 600 mA h g ⁻¹ at 0.1 A g ⁻¹ 400 mA h g ⁻¹ at 5 A g ⁻¹	[44]
VS ₂ -SNSs	0.4-3 V	1M NaSO ₃ CF ₃ diglyme	in 250 mA h g ⁻¹ at 0.2 A g ⁻¹ 203 mA h g ⁻¹ at 5 A g ⁻¹	[45]
VS ₂ nanosheet	0.01-3 V	1M NaClO ₄ in EC, DEC, and FEC	700 mA h g ⁻¹ at 0.1 A g ⁻¹ 400 mA h g ⁻¹ at 2 A g ⁻¹	[46]
VS ₂ HFS/RGO	0.1-2.5 V	1M NaClO ₄ in EC, PC, and FEC	430 mA h g ⁻¹ at 0.1 A g ⁻¹ 350 mA h g ⁻¹ at 2 A g ⁻¹	[47]
OL-VMS	0.1-3 V	1M NaSO ₃ CF ₃ diglyme	in 602.9 mA h g ⁻¹ at 0.1 A g ⁻¹ 452.8 mA h g ⁻¹ at 5 A g ⁻¹	This work
OL-VMS	0.01-3 V	1M NaSO ₃ CF ₃ diglyme	in 626.4 mA h g ⁻¹ at 2 A g ⁻¹	This work

DME : Dimethoxyethane; EC : Ethylene carbonate; DEC : Diethyl carbonate; PC : Propylene carbonate; EMC : Ethyl methyl carbonate; FEC : Fluoroethylene carbonate.

5.3.3 Electrochemical kinetics

It has been proven that the charge storage mechanisms include following two parts: one is the surface controlling process (pseudocapacitive), and the other is the diffusion-controlling process[48, 49]. Thus, the following equation could be adopted to evaluate the mechanism of this material [50, 51]:

$$i = av^b \quad (1)$$

where v and i are scan rate and current, respectively, and a and b are adjustable. In general, b -value should be in a scope of 0.5-1. The b -value of 1 stands for a surface-controlling process whereas the b -value approaching to 0.5 represents the other charge storage mechanism. To further evaluate the mechanism of charge storage for OL-VMS based anode, the CV curves measured at 0.1, 0.3, 0.5, 0.7, 0.9, 1.2, and 1.5 mV s^{-1} were

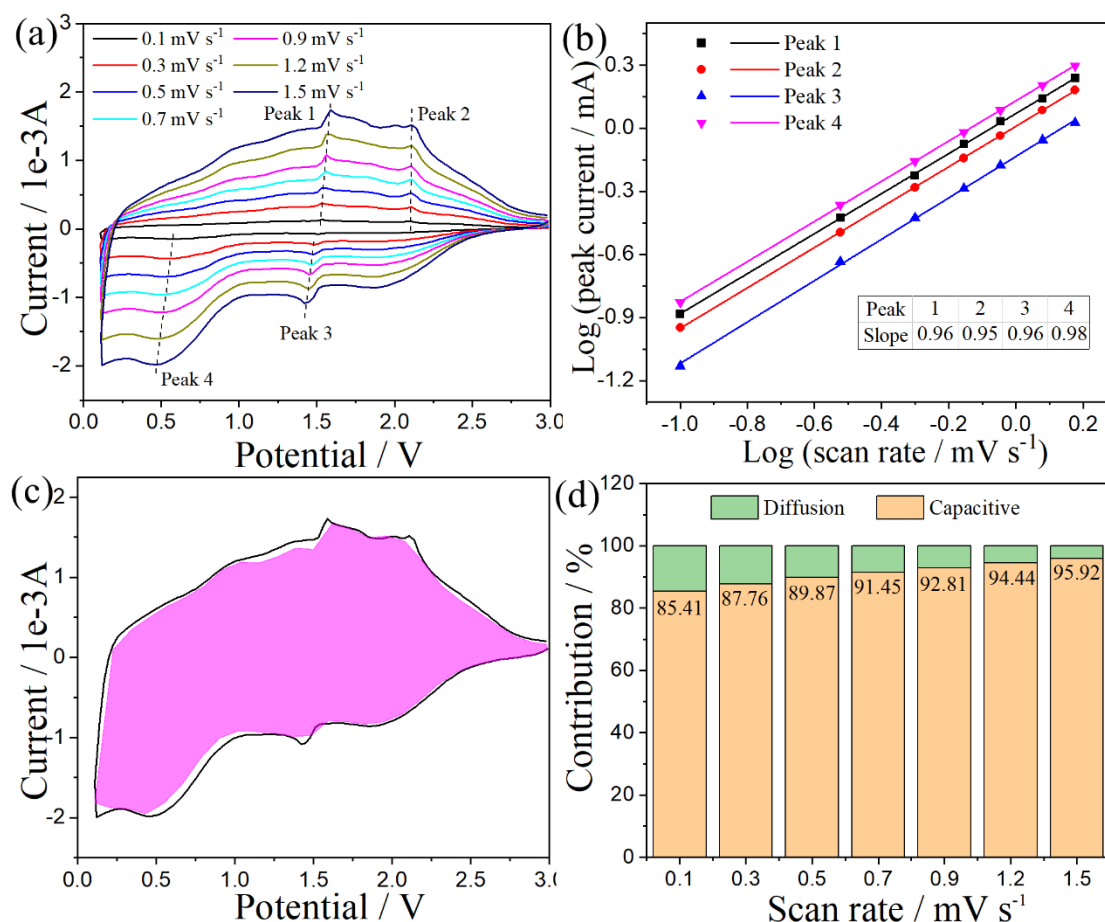


Figure 5.11 (a) CV curves of the OL-VMS based anode at different scan rates from 0.1 to 1.5 $mV s^{-1}$; (b) Fitting line of $\log i$ vs. $\log v$ plots for peaks 1, 2, 3 and 4; (c) The calculated contribution of capacitive at 1.5 $mV s^{-1}$; (d) The content of capacitive contribution for OL-VMS at various scan rates from 0.1 to 1.5 $mV s^{-1}$.

collected (Figure 5.11a) and based on them, a linear correlation between the $\log i$ and $\log v$ for each peak was obtained (Figure 5.11b). According to the linear fitting, the b-values of the peaks 1, 2, 3 and 4 were calculated to be 0.96, 0.95, 0.96 and 0.98, respectively. It should be noted that all of these b-values were close to 1, revealing a dominant surface-controlling process by using such an OL-VMS based anode, which was benefit for the fast charge transport as well as excellent rate performance.

Furthermore, the total current was composed of two parts: one corresponds to the current of capacitive (surface-controlling process), and the other is ascribed to the current of diffusion process, which could be calculated by the following equation [52]:

$$i = k_1\nu + k_2\nu^{1/2} \quad (2)$$

where k_1 and k_2 are adjustable parameters, ν corresponds to the scan rate, and i stands for value of current; $k_1\nu$ and $k_2\nu^{1/2}$ stand for the current values contributed by surface- and diffusion- controlling processes, separately. According to the k_1 and k_2 values based on the Eq. (2), the contributions of capacitive at various scan rates can be known. Figure 5.11 c shows the capacitive contribution of the OL-VMS-based anode at 1.5 mV s^{-1} , in which a high contribution of 95.92 % was achieved. Meanwhile, the contributions of capacitive process at various scan rates were also known and summarized in Figure 5.11d. The OL-VMS-based anode displayed a series of high capacitive contributions of 85.41, 87.76, 89.87, 91.45, 92.81, 94.44, and 95.92 corresponding to 0.1, 0.3, 0.5, 0.7, 0.9, 1.2, and 1.5 mV s^{-1} , respectively, revealing an outstanding charge transfer kinetics.

5.3.4 EIS analysis

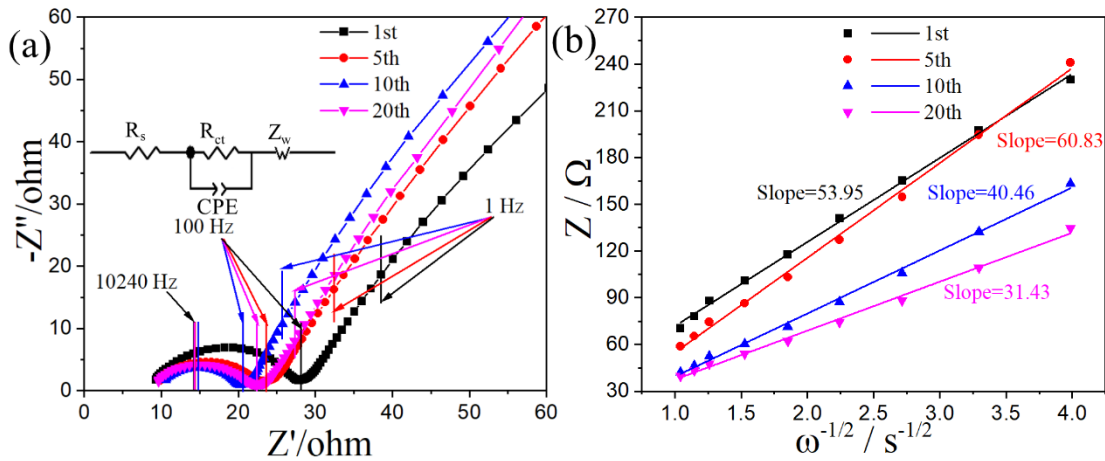


Figure 5.12 (a) EIS Nyquist plots of the OL-VMS-based electrode after 1st, 5th, 10th, and 20th cycles (inset: equivalent circuit); (b) the linear fitting between Z' and $\omega^{-1/2}$.

Table 5.2 Fitting results of Nyquist plots based on the equivalent circuits after 1st, 5th, 10th, and 20th cycles.

Cycle	R_s	R_{ct}
1 st	8.45	19.12
5 th	8.51	13.56
10 th	9.17	10.52
20 th	8.82	11.85

Figure 5.12a shows Nyquist plots measured after 1, 5, 10, and 20 cycles at 0.2 A g⁻¹ for OL-VMS based anode. Generally, the Nyquist plot consists of two sections: one is a semicircle in high frequency region, which is indexed to Warburg impedance (Z_w) relating to the Na⁺ diffusion; the other is a slope line in the low frequency region assigning to charge-transfer resistance (R_{ct}) [12, 53]. According to the equivalent circuit, the R_{ct} values were calculated to be 19.12, 13.56, 10.52, and 11.85 Ω after 1, 5, 10, and 20 cycles, respectively (Table 5.2). Obviously, the R_{ct} of the OL-VMS based anode

decreased gradually with the increasing of cycle, which could be attributed to the stable SEI layer formation and the enhanced electronic transfer kinetics [43, 54]. Furthermore, at the low frequency region, the slope line related with Warburg impedance was analyzed to evaluate diffusion of Na⁺ by using the following two equations [24, 55]:

$$Z' = R_S + R_{ct} + \sigma_w \omega^{-0.5} \quad (3)$$

$$D = \frac{R^2 T^2}{2A^2 n^4 F^4 C^2 \sigma_w^2} \quad (4)$$

where σ_w is the Warburg impedance coefficient. According to the linear fitting between Z' and $\omega^{-0.5}$ (Figure 5.12b), the value of Warburg impedance coefficient can be calculated based on the slope of fitting line. Herein, the low Warburg impedance coefficient means the high Na⁺ diffusion coefficient (D) according to Eq. (4), indicating the fast diffusion of Na⁺. With the increase of cycle numbers, the Warburg coefficient gradually decreased from 53.95 to 31.43, revealing a fast Na⁺ diffusion, which could be attributed to expansion of interlayer spacing during the charging/discharging process [56].

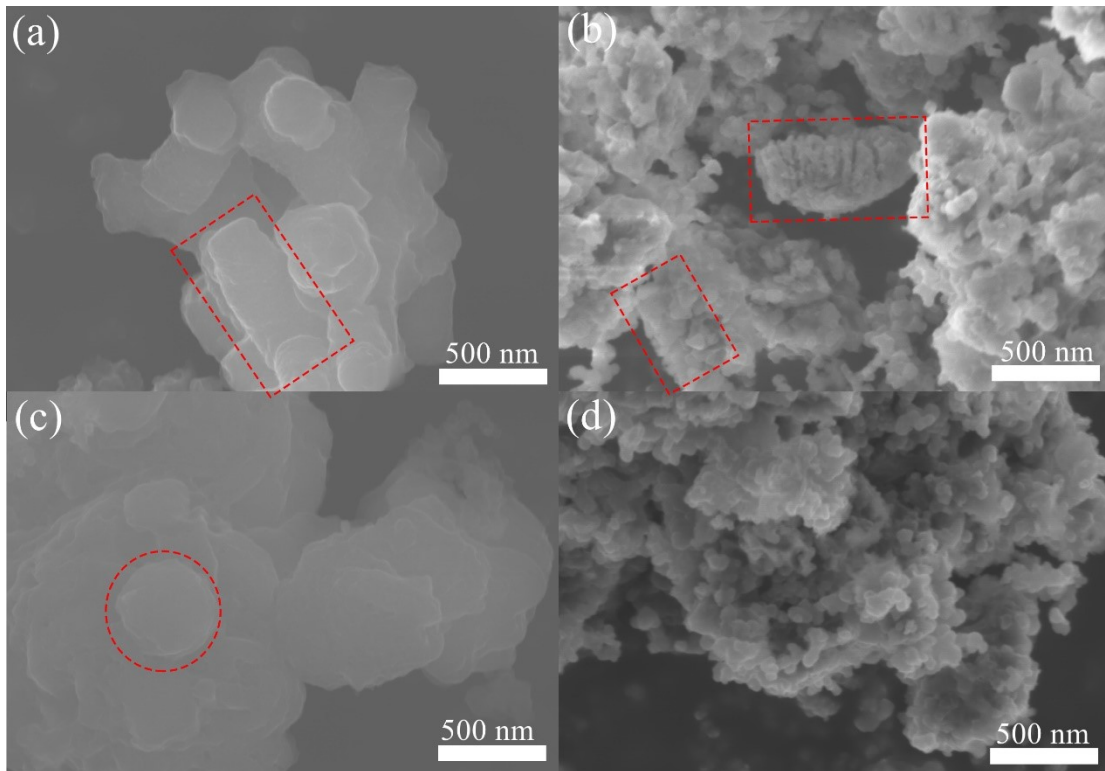


Figure 5.13 SEM images of (a, b) OL-VMS and (c, d) VMS with flower-like structure after 1 and 10 cycles.

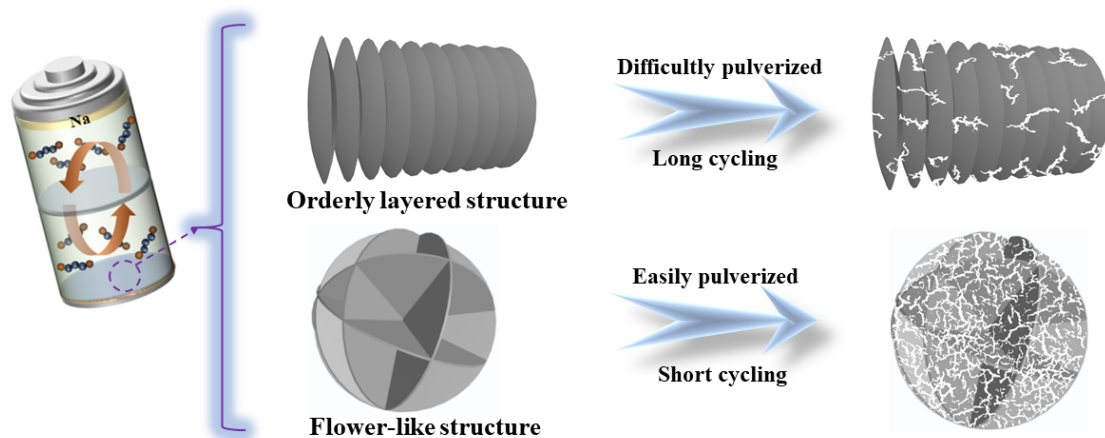


Figure 5.14 Illustration of pulverization of different structure during intercalation/deintercalation of Na^+ .

To prove the structural stability, the SEM images of OL-VMS with orderly layered structure and the VMS with flower-like structure after cycling test were observed. As

shown in Figure 5.13, after 1 cycle (Figure 5.13 a and c), the structures of both materials were still maintained. However, after 10 cycles, the orderly layered structure of OL-VMS was still kept (Figure 5.13 b) but the flower-like structure of the VMS was totally pulverized (Figure 5.13 d). Based on the above results, the OL-VMS with the orderly layered structure should be more difficult to pulverize during the ion intercalation/deintercalation process as illustrated in Figure 5.14, resulting in excellent cycling stability. In contrast, the VMS with the flower-like structure was more easily pulverized, leading to a short cycling life.

5.4 Conclusions

In conclusion, a novel orderly layered VMOs₂ anode material was successfully obtained using a facile self-assembly hydrothermal way followed with a heating treatment process, which displayed an excellent electrochemical performance due to the specific nanostructure. It is found that more defects could be exposed at the edges of stacked nanosheets to offer abundant storage sites for Na⁺, which effectively enhanced the specific capacity. Meanwhile, the orderly stacked nanosheets with vertical path and stable framework facilitated Na⁺ transportation, which effectively promoted the rate performance and buffered the volume expansion during the intercalation/deintercalation process, causing good cycling stability. In consequence, the OL-VMS anode material possessed a remarkable specific capacity (602.9 mAh g⁻¹ @200 mA g⁻¹), excellent cyclability (534 mAh g⁻¹ after 190 cycles at 2 A g⁻¹) and superior rate capacity (452.8 mAh g⁻¹@5 A g⁻¹) in the cut-off voltage range of 0.1-3 V.

Moreover, OL-VMS based anode also showed outstanding specific capacity of 626.4 mAh g⁻¹ even after 100 cycles at 2 A g⁻¹. In addition, in the case without the conductive carbon addition, it still delivered good electrochemical properties with a high specific capacity (260 mAh g⁻¹@1 A g⁻¹ after 130-cycle in 0.3-3 V voltage range). This work supplies an effective strategy to simply synthesize layered materials for achieving high electrochemical performance, which could significantly improve the energy density and reduce the cost toward commercialization.

References

- [1] B. Dunn, H. Kamath, J.-M. Tarascon, Electrical energy storage for the grid: a battery of choices, *Science* 334 (2011) 928-935.
- [2] M. Chen, Q. Liu, S.W. Wang, E. Wang, X. Guo, S.L. Chou, High-abundance and low-cost metal-based cathode materials for sodium-ion batteries: problems, progress, and key technologies, *Adv. Energy Mater.* 9 (2019) 1803609.
- [3] J.M. Lee, G. Singh, W. Cha, S. Kim, J. Yi, S.-J. Hwang, A. Vinu, Recent advances in developing hybrid materials for sodium-ion battery anodes, *ACS Energy Letters* 5 (2020) 1939-1966.
- [4] M. Chen, W. Hua, J. Xiao, D. Cortie, W. Chen, E. Wang, Z. Hu, Q. Gu, X. Wang, S. Indris, NASICON-type air-stable and all-climate cathode for sodium-ion batteries with low cost and high-power density, *Nat. Commun.* 10 (2019) 1-11.

- [5] Y. Wen, K. He, Y. Zhu, F. Han, Y. Xu, I. Matsuda, Y. Ishii, J. Cumings, C. Wang, Expanded graphite as superior anode for sodium-ion batteries, *Nat. Commun.* 5 (2014) 1-10.
- [6] H. Pan, Y.-S. Hu, L. Chen, Room-temperature stationary sodium-ion batteries for large-scale electric energy storage, *Energ. Environ. Sci.* 6 (2013) 2338-2360.
- [7] H. Zhang, Y. Huang, H. Ming, G. Cao, W. Zhang, J. Ming, R. Chen, Recent advances in nanostructured carbon for sodium-ion batteries, *J. Mater. Chem. A* 8 (2020) 1604-1630.
- [8] S. Fang, D. Bresser, S. Passerini, Transition metal oxide anodes for electrochemical energy storage in lithium-and sodium-ion batteries, *Adv. Energy Mater.* 10 (2020) 1902485.
- [9] T. Wang, D. Legut, Y. Fan, J. Qin, X. Li, Q. Zhang, Building Fast Diffusion Channel by Constructing Metal Sulfide/Metal Selenide Heterostructures for High-Performance Sodium Ion Batteries Anode, *Nano Lett.* 20 (2020) 6199-6205.
- [10] S. Liang, Y.J. Cheng, J. Zhu, Y. Xia, P. Müller-Buschbaum, A Chronicle Review of Nonsilicon (Sn, Sb, Ge)-Based Lithium/Sodium-Ion Battery Alloying Anodes, *Small Methods* 4 (2020) 2000218.
- [11] F. Luo, X. Feng, L. Zeng, L. Lin, X. Li, B. Kang, L. Xiao, Q. Chen, M. Wei, Q. Qian, In situ simultaneous encapsulation of defective MoS₂ nanolayers and sulfur nanodots into SPAN fibers for high rate sodium-ion batteries, *Chem. Eng. J.* 404 (2021) 126430.

- [12] W. Ren, H. Zhang, C. Guan, C. Cheng, Ultrathin MoS₂Nanosheets@Metal Organic Framework-Derived N-Doped Carbon Nanowall Arrays as Sodium Ion Battery Anode with Superior Cycling Life and Rate Capability, *Adv. Funct. Mater.* 27 (2017) 1702116.
- [13] Z. Hu, Q. Liu, S.L. Chou, S.X. Dou, Advances and Challenges in Metal Sulfides/Selenides for Next-Generation Rechargeable Sodium-Ion Batteries, *Adv. Mater.* 29 (2017).
- [14] W. Kang, Y. Wang, J. Xu, Recent progress in layered metal dichalcogenide nanostructures as electrodes for high-performance sodium-ion batteries, *J. Mater. Chem. A* 5 (2017) 7667-7690.
- [15] Y. Liu, X. Hu, G. Zhong, J. Chen, H. Zhan, Z. Wen, Layer-by-layer stacked nanohybrids of N,S-co-doped carbon film modified atomic MoS₂ nanosheets for advanced sodium dual-ion batteries, *J. Mater. Chem. A* 7 (2019) 24271-24280.
- [16] B. Lu, J. Liu, R. Hu, H. Wang, J. Liu, M. Zhu, C@MoS₂@PPy sandwich-like nanotube arrays as an ultrastable and high-rate flexible anode for Li/Na-ion batteries, *Energy Storage Mater.* 14 (2018) 118-128.
- [17] W. Tang, X. Wang, Y. Zhong, D. Xie, X. Zhang, X. Xia, J. Wu, C. Gu, J. Tu, Hierarchical MoS₂/Carbon Composite Microspheres as Advanced Anodes for Lithium/Sodium-Ion Batteries, *Chemistry* 24 (2018) 11220-11226.
- [18] X. Xu, R. Zhao, W. Ai, B. Chen, H. Du, L. Wu, H. Zhang, W. Huang, T. Yu, Controllable Design of MoS₂ Nanosheets Anchored on Nitrogen-Doped Graphene:

Toward Fast Sodium Storage by Tunable Pseudocapacitance, *Adv. Mater.* 30 (2018) e1800658.

[19] K. Ma, Y. Dong, H. Jiang, Y. Hu, P. Saha, C. Li, Densified MoS₂/Ti₃C₂ films with balanced porosity for ultrahigh volumetric capacity sodium-ion battery, *Chem. Eng. J.* (2020) 127479.

[20] J. Ru, T. He, B. Chen, Y. Feng, L. Zu, Z. Wang, Q. Zhang, T. Hao, R. Meng, R. Che, Covalent Assembly of MoS₂ Nanosheets with SnS Nanodots as Linkages for Lithium/Sodium-Ion Batteries, *Angewandte Chemie International Edition* 59 (2020) 14621-14627.

[21] H. Chen, T. Song, L. Tang, X. Pu, Z. Li, Q. Xu, H. Liu, Y. Wang, Y. Xia, In-situ growth of vertically aligned MoS₂ nanowalls on reduced graphene oxide enables a large capacity and highly stable anode for sodium ion storage, *J. Power Sources* 445 (2020) 227271.

[22] L. Han, S. Wu, Z. Hu, M. Chen, J. Ding, S. Wang, Y. Zhang, D. Guo, L. Zhang, S. Cao, Hierarchically porous MoS₂-carbon hollow rhomboids for superior performance of the anode of sodium-ion batteries, *ACS Appl. Mater. Inter.* 12 (2020) 10402-10409.

[23] W. Ye, F. Wu, N. Shi, H. Zhou, Q. Chi, W. Chen, S. Du, P. Gao, H. Li, S. Xiong, Metal-Semiconductor Phase Twinned Hierarchical MoS₂ Nanowires with Expanded Interlayers for Sodium-Ion Batteries with Ultralong Cycle Life, *Small* 16 (2020) 1906607.

- [24] G. Wang, X. Bi, H. Yue, R. Jin, Q. Wang, S. Gao, J. Lu, Sacrificial template synthesis of hollow C@MoS₂@PPy nanocomposites as anodes for enhanced sodium storage performance, *Nano Energy* 60 (2019) 362-370.
- [25] Y. Qiao, J. Wu, X. Cheng, Y. Pang, Z. Lu, X. Lou, Q. Li, J. Zhao, S. Yang, Y. Liu, Construction of robust coupling interface between MoS₂ and nitrogen doped graphene for high performance sodium ion batteries, *J. Energy Chem.* 48 (2020) 435-442.
- [26] Z. Lei, J. Zhan, L. Tang, Y. Zhang, Y. Wang, Recent Development of Metallic (1T) Phase of Molybdenum Disulfide for Energy Conversion and Storage, *Adv. Energy Mater.* 8 (2018) 1703482.
- [27] P. He, M. Yan, G. Zhang, R. Sun, L. Chen, Q. An, L. Mai, Layered VS₂ nanosheet-based aqueous Zn ion battery cathode, *Adv. Energy Mater.* 7 (2017) 1601920.
- [28] J. Su, M. Wang, Y. Li, F. Wang, Q. Chen, P. Luo, J. Han, S. Wang, H. Li, T. Zhai, Sub-Millimeter-Scale Monolayer p-Type H-Phase VS₂, *Adv. Funct. Mater.* 30 (2020) 2000240.
- [29] Y. Zhou, Q. Xu, T. Ge, X. Zheng, L. Zhang, P. Yan, Accurate control of VS₂ nanosheets for coexisting high photoluminescence and photothermal conversion efficiency, *Angewandte Chemie* 132 (2020) 3348-3354.
- [30] W. Li, J. Huang, L. Feng, L. Cao, Y. Liu, L. Pan, Nano-grain dependent 3D hierarchical VS₂ microrods with enhanced intercalation kinetic for sodium storage properties, *J. Power Sources* 398 (2018) 91-98.

- [31] J. Bai, B. Zhao, X. Wang, H. Ma, K. Li, Z. Fang, H. Li, J. Dai, X. Zhu, Y. Sun, Yarn ball-like MoS₂ nanospheres coated by nitrogen-doped carbon for enhanced lithium and sodium storage performance, *J. Power Sources* 465 (2020) 228282.
- [32] P. Li, Y. Yang, S. Gong, F. Lv, W. Wang, Y. Li, M. Luo, Y. Xing, Q. Wang, S. Guo, Co-doped 1T-MoS₂ nanosheets embedded in N, S-doped carbon nanobowls for high-rate and ultra-stable sodium-ion batteries, *Nano Res.* 12 (2018) 2218-2223.
- [33] M. Naguib, J. Halim, J. Lu, K.M. Cook, L. Hultman, Y. Gogotsi, M.W. Barsoum, New two-dimensional niobium and vanadium carbides as promising materials for Li-ion batteries, *J. Am. Chem. Soc.* 135 (2013) 15966-15969.
- [34] T. Guo, Y. Song, Z. Sun, Y. Wu, Y. Xia, Y. Li, J. Sun, K. Jiang, S. Dou, J. Sun, Bio-templated formation of defect-abundant VS₂ as a bifunctional material toward high-performance hydrogen evolution reactions and lithium–sulfur batteries, *J. Energy Chem.* 42 (2020) 34-42.
- [35] Y. Dong, Z. Zhu, Y. Hu, G. He, Y. Sun, Q. Cheng, I.P. Parkin, H. Jiang, Supersaturated bridge-sulfur and vanadium co-doped MoS₂ nanosheet arrays with enhanced sodium storage capability, *Nano Res.* (2020).
- [36] X. Xue, R. Chen, C. Yan, P. Zhao, Y. Hu, W. Kong, H. Lin, L. Wang, Z. Jin, One-Step Synthesis of 2-Ethylhexylamine Pillared Vanadium Disulfide Nanoflowers with Ultralarge Interlayer Spacing for High-Performance Magnesium Storage, *Adv. Energy Mater.* 9 (2019) 1900145.

- [37] K. Li, J. Zhang, D. Lin, D.W. Wang, B. Li, W. Lv, S. Sun, Y.B. He, F. Kang, Q.H. Yang, L. Zhou, T.Y. Zhang, Evolution of the electrochemical interface in sodium ion batteries with ether electrolytes, *Nat. Commun.* 10 (2019) 725.
- [38] X. Yue, J. Wang, A.M. Patil, X. An, Z. Xie, X. Hao, Z. Jiang, A. Abudula, G. Guan, A novel vanadium-mediated MoS₂ with metallic behavior for sodium ion batteries: achieving fast Na⁺ diffusion to enhance electrochemical kinetics, *Chem. Eng. J.* (2020) 128107.
- [39] S. Anwer, Y. Huang, B. Li, B. Govindan, K. Liao, J.C. W, F. Wu, R. Chen, L. Zheng, Nature-Inspired, Graphene-Wrapped 3D MoS₂ Ultrathin Microflower Architecture as a High-Performance Anode Material for Sodium-Ion Batteries, *ACS Appl Mater Interfaces* 11 (2019) 22323-22331.
- [40] X. Zhang, K. Liu, S. Zhang, F. Miao, W. Xiao, Y. Shen, P. Zhang, Z. Wang, G. Shao, Enabling remarkable cycling performance of high-loading MoS₂@Graphene anode for sodium ion batteries with tunable cut-off voltage, *J. Power Sources* 458 (2020) 228040.
- [41] L. Cao, X. Liang, X. Ou, X. Yang, Y. Li, C. Yang, Z. Lin, M. Liu, Heterointerface Engineering of Hierarchical Bi₂S₃/MoS₂ with Self-Generated Rich Phase Boundaries for Superior Sodium Storage Performance, *Adv. Funct. Mater.* 30 (2020) 1910732.
- [42] A. Cheng, H. Zhang, W. Zhong, Z. Li, D. Cheng, Y. Lin, Y. Tang, H. Shao, Z. Li, Few-layer MoS₂ embedded in N-doped carbon fibers with interconnected macropores for ultrafast sodium storage, *Carbon* 168 (2020) 691-700.

- [43] D. Xu, H. Wang, R. Qiu, Q. Wang, Z. Mao, Y. Jiang, R. Wang, B. He, Y. Gong, D. Li, Coupling of bowl-like VS₂ nanosheet arrays and carbon nanofiber enables ultrafast Na⁺-Storage and robust flexibility for sodium-ion hybrid capacitors, *Energy Storage Mater.* 28 (2020) 91-100.
- [44] D. Yu, Q. Pang, Y. Gao, Y. Wei, C. Wang, G. Chen, F. Du, Hierarchical flower-like VS₂ nanosheets – A high rate-capacity and stable anode material for sodium-ion battery, *Energy Storage Mater.* 11 (2018) 1-7.
- [45] R. Sun, Q. Wei, J. Sheng, C. Shi, Q. An, S. Liu, L. Mai, Novel layer-by-layer stacked VS₂ nanosheets with intercalation pseudocapacitance for high-rate sodium ion charge storage, *Nano Energy* 35 (2017) 396-404.
- [46] J. Zhou, L. Wang, M. Yang, J. Wu, F. Chen, W. Huang, N. Han, H. Ye, F. Zhao, Y. Li, Y. Li, Hierarchical VS₂ Nanosheet Assemblies: A Universal Host Material for the Reversible Storage of Alkali Metal Ions, *Adv. Mater.* 29 (2017).
- [47] H. Qi, L. Wang, T. Zuo, S. Deng, Q. Li, Z.H. Liu, P. Hu, X. He, Hollow Structure VS₂@Reduced Graphene Oxide (RGO) Architecture for Enhanced Sodium-Ion Battery Performance, *ChemElectroChem* 7 (2020) 78-85.
- [48] J. Wang, J. Polleux, J. Lim, B. Dunn, Pseudocapacitive contributions to electrochemical energy storage in TiO₂ (anatase) nanoparticles, *J. Phys. Chem. C* 111 (2007) 14925-14931.
- [49] T. Brezesinski, J. Wang, S.H. Tolbert, B. Dunn, Ordered mesoporous alpha-MoO₃ with iso-oriented nanocrystalline walls for thin-film pseudocapacitors, *Nature materials* 9 (2010) 146-151.

- [50] D. Chao, C. Zhu, P. Yang, X. Xia, J. Liu, J. Wang, X. Fan, S.V. Saviolov, J. Lin, H.J. Fan, Z.X. Shen, Array of nanosheets render ultrafast and high-capacity Na-ion storage by tunable pseudocapacitance, *Nat. Commun.* 7 (2016) 12122.
- [51] H. Lim, H. Kim, S.-O. Kim, W. Choi, Self-assembled N-doped MoS₂/carbon spheres by naturally occurring acid-catalyzed reaction for improved sodium-ion batteries, *Chem. Eng. J.* 387 (2020) 124144.
- [52] W. Wang, B. Jiang, C. Qian, F. Lv, J. Feng, J. Zhou, K. Wang, C. Yang, Y. Yang, S. Guo, Pistachio-Shuck-Like MoSe₂/C Core/Shell Nanostructures for High-Performance Potassium-Ion Storage, *Adv. Mater.* 30 (2018) e1801812.
- [53] N. Feng, R. Meng, L. Zu, Y. Feng, C. Peng, J. Huang, G. Liu, B. Chen, J. Yang, A polymer-direct-intercalation strategy for MoS₂/carbon-derived heteroaggregates with ultrahigh pseudocapacitance, *Nat. Commun.* 10 (2019) 1372.
- [54] Y. Zhang, H. Tao, T. Li, S. Du, J. Li, Y. Zhang, X. Yang, Vertically oxygen-incorporated MoS₂ nanosheets coated on carbon fibers for sodium-ion batteries, *ACS Appl. Mater. Inter.* 10 (2018) 35206-35215.
- [55] C. Zhao, C. Yu, M. Zhang, Q. Sun, S. Li, M. Norouzi Banis, X. Han, Q. Dong, J. Yang, G. Wang, X. Sun, J. Qiu, Enhanced sodium storage capability enabled by super wide-interlayer-spacing MoS₂ integrated on carbon fibers, *Nano Energy* 41 (2017) 66-74.
- [56] K. Yao, Z. Xu, J. Huang, M. Ma, L. Fu, X. Shen, J. Li, M. Fu, Bundled Defect-Rich MoS₂ for a High-Rate and Long-Life Sodium-Ion Battery: Achieving 3D Diffusion of Sodium Ion by Vacancies to Improve Kinetics, *Small* 15 (2019) e1805405.

CHAPTER 6 Conclusions and Prospects

6.1 Conclusions

Sodium ion battery (SIBs) are considered as an attractive candidate of Lithium ion battery (LIBs) due to the low cost of sufficient sodium resource and their comparable suitability in field of energy storage. Thus, numerous researchers have developed effective strategies to fabricate anode materials with excellent electrochemical performance. In this work, three different strategies, i.e., 1T and 2H phase mixing, V mediating and morphology designing with voltage cutting off, are applied to enhance the performance of MoS₂-based anode. It is found that the above strategies can effectively increase the electrochemical performance due to high conductivity, stable structure, and suitable voltage range. The following conclusions are achieved:

- (1) The effective strategies such as morphology design, structural engineering, electrolyte selecting, doping or combination with non-carbon material, and combination with carbon material, for enhancing electrochemical performance of layered metal sulfide are comprehensively summarized and analyzed (**Chapter 1**).
- (2) The MoS₂-MS anode material with 1T/2H phase is successfully synthesized by a one-step hydrothermal method. The obtained MoS₂-MS is confirmed to have disordered structure, rich defects and large interlayer spacing. As it is used as the anode material for SIBs, the MoS₂-MS-based anode displays a highly stable specific capacity of 467 mAh g⁻¹ over 100 cycles at 100 mA g⁻¹, good cycling stability with a specific capacity of 412 mAh g⁻¹ over 500 cycles at 1 A g⁻¹, and superb rate

performance with a maintaining specific capacity of 100 mAh g^{-1} at 20 A g^{-1} . Such an excellent electrochemical performance is considered to be ascribed to its specific structure. Especially, the 1-T phase presented in the disordered structure enhances the electrical conductivity, the rich defects provides more active sites for Na^+ ion storage and the large interlayer spacing facilitates the diffusion of the Na^+ ions. This work might provide a strategy to increase the electrochemical performance and decrease the cost for developing electrode materials in energy storage field **(Chapter 3)**.

(3) A series of high-performance VMoS_2 based anode materials for SIBs are successfully synthesized with different V:Mo molar ratios in the precursors through a facile one-step hydrothermal method. The experimental and DFT calculation results reveals that the V mediating in the structure of MoS_2 not only significantly enhances the conductivity, but also greatly increases the electrochemical kinetics with dominated the pseudocapacitive contribution for the sodium ion storage. As a result, the VMoS_2 material named VM-43 prepared with a V:Mo molar ratio of 4:3 is found to have the disordered structure with rich defects, and exhibits high reversible capacity (i.e., maintaining at 548.1 mAh g^{-1} over 80 cycles with 100 mA g^{-1}), excellent cycling stability (i.e., maintaining at 451.6 mAh g^{-1} over 800 cycles with 2 A g^{-1}) and superb rate performance (maintaining 207.4 mAh g^{-1} with 20 A g^{-1}). It is expected that this the novel electrode material preparation strategy could significantly decrease the cost, increase the electrochemical performance, and promote the commercialization of SIBs **(Chapter 4)**.

(4) A novel orderly layered VMoS₂ anode material is successfully obtained using a facile self-assembly hydrothermal way followed with a heating treatment process, which displays an excellent electrochemical performance due to the specific nanostructure. It is found that more defects could be exposed at the edges of stacked nanosheets to offer abundant storage sites for Na⁺, which effectively enhances the specific capacity. Meanwhile, the orderly stacked nanosheets with vertical path and stable framework facilitates Na⁺ transportation, which effectively promotes the rate performance and buffers the volume expansion during the intercalation/deintercalation process, causing good cycling stability. In consequence, the OL-VMS anode material possesses a remarkable specific capacity (602.9 mAh g⁻¹ @200 mA g⁻¹), excellent cyclability (534 mAh g⁻¹ after 190 cycles at 2 A g⁻¹) and superior rate capacity (452.8 mAh g⁻¹@5 A g⁻¹) in the cut-off voltage range of 0.1-3 V. Moreover, OL-VMS based anode also shows outstanding specific capacity of 626.4 mAh g⁻¹ even after 100 cycles at 2 A g⁻¹. In addition, in the case without the conductive carbon addition, it still delivers good electrochemical properties with a high specific capacity (322.6 mAh g⁻¹@1 A g⁻¹ in 0.3-3 V voltage range). This work supplies an effective strategy to simply synthesize layered materials for achieving high electrochemical performance, which could significantly improve the energy density and reduce the cost toward commercialization.

6.2 Prospects

Even though several effective strategies for the preparation of MoS₂-based anodes have been designed and applied to improve the electrochemical performance, it is still full of challenges for the commercialization of SIBs. In the future work, the following issues should be resolved:

- (1) Most of researchers have focused on how to improve the electrochemical performance. However, few people pay attention to the low initial coulombic efficiency of anode (below 90%) caused by decomposition of electrolyte and side reactions. Therefore, the strategies for enhancing ICE such as developing new electrolyte, adding additive and designing suitable structure should be considered to promote commercialization of SIBs in the future.
- (2) Even though the strategies for synthesizing the MoS₂-based anode with remarkable performance are so effective, the most current methods are very complicated and consume a lot of energy. Thus, it is practical and significant to fabricate novel anode materials with well-designed nanostructure for SIBs via some simple methods, which can largely decrease the cost and save energy.
- (3) Recently, researchers have made great progress in improving the electrochemical performance of MoS₂-based anode materials. However, few works explore the reaction mechanism and kinetics during charging/discharging process. To further understand the reaction mechanism and electrochemical reaction kinetics, the DFT

calculations should be combined with in-situ characterizations to investigate the mechanism during charging/discharging process.

List of publications and presentations

Publications

- 1) **Xiyan Yue**, Jiajia Wang, Amar M. Patil, Xiaowei An, Zhengkun Xie, Xiaogang Hao, Zhongqing Jiang, Abuliti Abudula, and Guoqing Guan, “A novel vanadium-mediated MoS₂ with metallic behavior for sodium ion batteries: achieving fast Na⁺ diffusion to enhance electrochemical kinetics,” *Chemical Engineering Journal*, (2021) 128107.
- 2) **Xiyan Yue**, Jiajia Wang, Zhengkun Xie, Amar M. Patil, Tao Yu, Xiao Du, Zhongde Wang, Xiaogang Hao, Abuliti Abudula, and Guoqing Guan, “Coral reef-like MoS₂ microspheres with 1T/2H phase as high performance anode material for sodium ion batteries,” *Journal of Materials Science*, 55 (2020) 14389–14400.
- 3) **Xiyan Yue**, Jiajia Wang, Zhengkun Xie, Yang. He, Tao Yu, Zhao Liu, Changlin Liu, Xiaogang Hao, Abuliti Abudula, and Guoqing Guan, “Controllable synthesis of novel orderly layered VMoS₂ anode materials with super electrochemical pperformance for sodium ion batteries,” *ACS CS Applied Materials & Interfaces*. (In submission)
- 4) Zhengkun Xie, Zhijun Wu, Xiaowei An, **Xiyan Yue**, Pairuzha Xiaokaiti, Akihiro Yoshida, Abuliti Abudula, and Guoqing Guan, “A sandwich-type composite polymer electrolyte for all-solid-state lithium metal batteries with high areal capacity and cycling stability,” *Journal of Membrane Science*, 596 (2020) 117739.
- 5) Amar M. Patil, **Xiyan Yue**, Akihiro Yoshida, Shasha Li, Xiaogang Hao, Abuliti Abudula, and Guoqing Guan, “Redox-AmbitiousRoute to Boost Energy and Capacity Retention of Pouch Type AsymmetricSolid-State Supercapacitor Fabricated with Graphene Oxide-Based HybridElectrodes,” *Applied Materials Today*, 19 (2020) 100563.
- 6) Jiajia Wang, **Xiyan Yue**, Yanyan Yang, Suchada Sirisomboonchai, Peifen

- Wang, Xuli Ma, Abuliti Abudula, Guoqing Guan, “Earth-abundant transition-metal-based bifunctional catalysts for overall electrochemical water splitting: A review,” *Journal of Alloys and Compounds*, 819 (2020) 153346.
- 7) Jiajia Wang, **Xiyan Yue**, Yanyan Yang, Zhongkai Zhao, Zhongliang Yu, Ping An, Abuliti Abudula, and Guoqing Guan, “Hydrogen Production from Chemical Looping Reforming: Current Status and Future Perspective,” Chapter 4 in Book “New Dimensions in Production and Utilization of Hydrogen” edited by Sonil Nanda, Dai-Viet N. Vo, and Phuong Nguyen-Tri, *Elsevier*, Radarweg 29, PO Box 211, 1000 AE Amsterdam, Netherlands, ISBN: 978-0-12-819553-6; eBook ISBN: 9780128231579; Published Date: 17th August 2020.
 - 8) Zhengkun Xie, Zhijun Wu, Xiaowei An, **Xiyan Yue**, Jiajia Wang, Abudula and Guoqing Guan, “Anode-Free Rechargeable Lithium Metal Batteries: Progress and Prospects,” *Energy Storage Materials*, 32 (2020) 386-401.
 - 9) Amar M. Patil, Xiaowei An, Shasha Li, **Xiyan Yue**, Xiao Du, Akihiro Yoshida, Xiaogang Hao, Abuliti Abudula, and Guoqing Guan, “Fabrication of three-dimensionally heterostructured rGO/WO₃.0.5H₂O@Cu₂S electrodes for high-energy solid-state pouch-type asymmetric supercapacitor,” *Chemical Engineering Journal*, 403 (2021) 126411.
 - 10) Zhengkun Xie, Xiaowei An, Zhijun Wu, **Xiyan Yue**, Jiajia Wang, Xiaogang Hao, Abuliti Abudula and Guoqing Guan, “Fluoropyridine family: Bifunction as electrolyte solvent and additive to achieve dendrites-free lithium metal batteries,” *Journal of Materials Science & Technology*, 74 (2021) 119-127.
 - 11) Zhengkun Xie, Zhijun Wu, Xiaowei An, **Xiyan Yue**, Akihiro Yoshida, Xiao Du, Xiaogang Hao, Abuliti Abudula, and Guoqing Guan, “2-Fluoropyridine: a novel electrolyte additive for lithium metal batteries with high areal capacity as well as high cycling stability,” *Chemical Engineering Journal*, 393 (2020) 124789.

Domestic presentations

- (1) XIYAN YUE, Zhengkun Xie, Zhijun Wu, Amar M. Patil, Tao Yu, Akihiro Yoshida, Abuliti Abudula, Guoqing Guan " One step hydrothermal synthesis MoS₂ as high performance anode material for sodium ion batteries", 2019 年電気化学大会秋季大会, Yamanashi, Japan, September 5-6, 2019.
- (2) XIYAN YUE, Jiajia Wang, Zhengkun Xie, Zhijun Wu, Amar M. Patil, Tao Yu, Akihiro Yoshida, Abuliti Abudula, Guoqing Guan, "Vanadium doped MoS₂ to form V_xMo_yS_z: a promising anode with excellent performance for sodium ion batterie" 2020 年電気化学大会春季大会, Nagoya, Japan, March 17-19, 2020.
- (3) XIYAN YUE, Jiajia Wang, Zhengkun Xie, Zhijun Wu, Amar M. Patil, Tao Yu, Akihiro Yoshida, Abuliti Abudula, Guoqing Guan, "Facile synthesis of VS₂/MoS₂ heterostructure with expanded (002) interlayer spacing as anode material for sodium ion batteries" 令和 2 年度化学系学協会東北大会 (2020). Hachinohe, Japan, September 26-27, 2020.
- (4) XIYAN YUE, Jiajia Wang, Zhengkun Xie, Zhijun Wu, Amar M. Patil, Tao Yu, Akihiro Yoshida, Abuliti Abudula, Guoqing Guan, "VMoS₂ with expanded interlayer spacing for enhancing sodium storage capacity," 化学工学会第 51 回秋季大会, Iwate, Japan, September 24-26, 2020.

List of patents

- (1) 岳喜岩、官国清、吉田曉弘、関和治、阿布里提、"二次電池用負極活物質、"
特願 2019-155563、出願日：2019 年 8 月 28 日。(專利)
- (2) 岳喜岩、官国清、王佳佳、関和治、阿布里提、"正極活物質、正極材料及び該正極材料を備える二次電池、並びに、正極活物質の製造方法、" 出願番号：特願 2021-014643、出願日：2021 年 2 月 1 日。(專利)
- (3) 王佳佳、官国清、岳喜岩、関和治、阿布里提、"負極活物質、負極材料及び該負極材料を備えるアルカリイオン電池、並びに負極活物質の製造方法"、日本特許、出願番号：特願 2021-020949、出願日：2021 年 2 月 12 日。

- (4) 王佳佳、官国清、**岳喜岩**、謝正坤、武志俊、関和治、阿布里提、“アルカリ金属—硫黄電池用正極材料及びこれを備えたアルカリ金属—硫黄電池”、日本特許、出願番号：特願 2020-150417、出願日：2020 年 9 月 8 日。
- (5) 謝正坤、官国清、武志俊、**岳喜岩**、関和治、阿布里提、“電池用電解液及びリチウム電池”、日本特許、出願番号：特願 2020-102684、出願日：2020 年 6 月 12 日。
- (6) 謝正坤、官国清、武志俊、**岳喜岩**、関和治、阿布里提、“二次電池用正極活物質前駆体、二次電池用正極活物質、二次電池用陰極液、二次電池用正極及び二次電池”、日本特許、出願番号：特願 2020-019666、出願日：2020 年 2 月 7 日。
- (7) 謝正坤、官国清、**岳喜岩**、武志俊、吉田曉弘、阿布里提、関和治、“生物材料由来のハードカーボン、負極材料、負極、及びアルカリイオン電池、”
出願番号：特願 2019-192989、出願日：2019 年 10 月 23 日。

Award

1. **Excellent Student Recognition**, Hirosaki University, Japan, March, 2021

Curriculum vitae

2011.9-2015.7 Xuchang University Chemical Engineering and Technology

2015.9-2018.7 Taiyuan University of Technology Chemical Engineering

2018.10-2021.9 Hirosaki University Safety System Engineering